

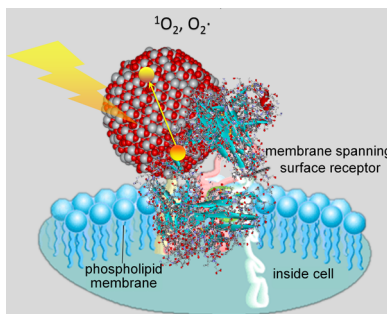
Titanium Dioxide in the Service of the Biomedical Revolution

Tijana Rajh,*[†] Nada M. Dimitrijevic,[†] Marc Bissonnette,[‡] Tamara Koritarov,^{†,§} and Vani Konda[‡]

[†]Center for Nanoscale Materials, Argonne National Laboratory, 9700 South Cass Avenue, Argonne, Illinois 60540, United States

[‡]Department of Medicine, The University of Chicago Medicine, 5841 South Maryland Avenue, MC 4076, Chicago, Illinois 60637, United States

[§]School of Medicine, Boston University, 72 East Concord Street, Boston, Massachusetts 02118, United States



CONTENTS

1. Introduction
 2. Energy Band Structure of TiO_2 Nanoparticles
 3. Importance of Surface Sites in TiO_2 Nanoparticles
 4. Nanoparticles as Redox Active Centers
 5. Charge Separation in TiO_2 Redox Active Centers: EPR Spectroscopy
 6. Effect of Size and Shape on Bulk and Surface Properties of Anatase Nanoparticles
 7. Toxicity of Pristine TiO_2 Nanoparticles
 8. Phototoxicity of TiO_2 Nanoparticles: Generation of Reactive Oxygen Species
 9. Biomedical Applications of Pristine TiO_2 Nanoparticles
 10. Sensitization of TiO_2 Nanoparticles for Absorption of Visible Light
 - 10.1. Enediol and Catechol Sensitization of TiO_2 Nanoparticles
 - 10.2. Dye Sensitization of TiO_2 Nanoparticles
 - 10.3. Sensitization by Anionic and Cationic Doping
 - 10.4. Surface Modification with Inorganic Complexes
 11. Binding Specificity of DNA Hybrid Nanocomposites
 - 11.1. TiO_2/DNA Conjugates in the Cell Machinery
 - 11.2. TiO_2/DNA Conjugates and Biosensing
 12. Binding Specificity of Protein Hybrid Nanocomposites
 - 12.1. $\text{TiO}_2/\text{Antibody}$ Interaction with Cell Machinery
 - 12.2. $\text{TiO}_2/\text{Protein}$ Conjugates and Biosensing
 13. Drug Delivery
 14. Imaging Guided Therapy
 15. Concluding Remarks and Future Directions
- Author Information
Corresponding Author

| | |
|-----------------|----|
| Notes | AJ |
| Biographies | AJ |
| Acknowledgments | AK |
| References | AK |

1. INTRODUCTION

Over time, nature has developed elegant molecular structures and complex machinery at the nanoscale to regulate sophisticated and synchronized cell functioning. Control and manipulation of biomolecules, which are basic elements of cell functioning, and their assemblies within the living cells are still major challenges in understanding and replicating the complex functioning of cells. Biomolecules such as proteins, RNA, and DNA exhibit dimensions that are comparable to those of nanoparticles. As they have similar length scale nanoparticles and biomolecules can be integrated into a hybrid entity to provide an interesting tool for tracking chemical processes and probing mechanisms of cell functioning within living cells.

Fifty-five years ago, in his famous talk “Plenty of Room at the Bottom”, Richard Feynman not only anticipated the field of nanotechnology alone but also envisioned the new field of bionanomedicine.¹ In his talk, he quoted his friend Albert R. Hibbs,² who suggested a very interesting possibility: “... although it is a very wild idea, it would be interesting in surgery if you could swallow the surgeon.”¹ This concept was abandoned for a few decades until nanotechnology offered a potential to shape matter on the molecular level and coax atoms into new combinations to result in hybrid structures of manmade materials and biomolecules with properties that extend beyond individual constituents.

With advances in the nanoscience and nanotechnology fields, a new class of composite materials was developed that physically integrates inorganic nanoparticles and biologically active molecules.³ These hybrid conjugates can display unique recognition and catalytic properties and potentially be reintroduced into the living organism and successfully incorporated into the cell machinery. These bioinorganic composites exhibit multifunctional properties that are responsible for their ability to integrate with both inorganic materials, via covalent bonding to inorganic supports, and biological entities, via site-selective multivalent interactions with cell constituents. This development opened new opportunities for impacting diverse applications affecting biosensing, site-selective

Special Issue: 2014 Titanium Dioxide Nanomaterials

Received: January 16, 2014



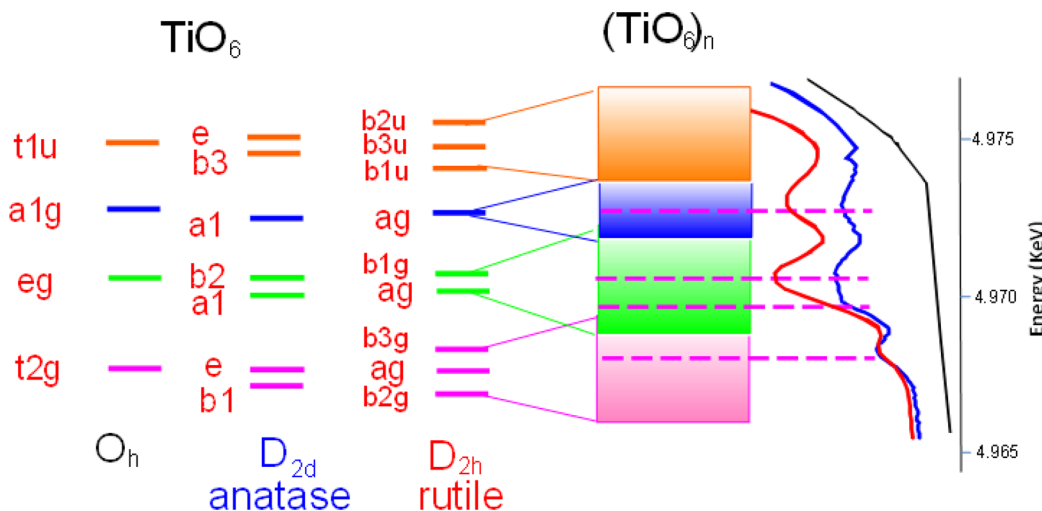


Figure 1. Schematic presentation of energy levels of TiO_6 octahedra in ideal octahedral (black), anatase (blue), and rutile (red) environment.¹¹ As atoms approach each other to form a periodic crystal, the levels form energy bands that constitute a conduction band of TiO_2 appear in XANES as a pre-edge structure (shown as black, blue, and red spectra on the far right).

catalysis, energy transduction, as well as advanced medical therapies.

Development of hybrid materials with collective properties that combine delocalized electronic states of semiconductors and localized orbitals of biomolecules is particularly interesting for creation of nanoscale energy converters, because these composites have the ability of carrying out site-selective redox chemistry. Many important biological processes involve redox chemistry, including cellular respiration or cell signaling. Introduction of hybrid nanoscale energy converters into the cell matrix in a site-selective manner enables participation of the composites in desired cell metabolic functions, forming a basis for new tools for biomedicine and biotechnology operated by redox chemistry. For that purpose a special class of functional nanoparticles capable of site-specific interactions with cell components that are also capable of participating in electron transfer or other energy transducing processes have to be developed.⁴ In this review we discuss new approaches for creating and utilizing bioinorganic composites of one of the most investigated nanoscale materials, titanium dioxide (TiO_2), for biomedical applications.

TiO_2 has been extensively used in many industrially relevant processes ranging from environmental applications to clean energy and from cosmetics to paint. Wide use of TiO_2 is based on its exceptionally efficient photoactivity, high chemical stability, and low cost. More significantly, since ancient times TiO_2 has been used as a white pigment,⁵ and thus, its low toxicity for both humans and the environment has been established over the course of history. Despite the intensive studies of TiO_2 in various fields, use of TiO_2 in biomedical applications is relatively new. The first papers appeared in the 1990s with increasing use of titanium in implants and the need to understand the interaction of cell components and biomolecules with implant surfaces covered with oxidized titanium.^{6,7} During that time a report appeared demonstrating the first use of TiO_2 for photoinduced cell death by Fujishima et al.⁸ Soon after, the field gained momentum, and beginning in the mid-2000s, the number of publications and citations began to exponentially increase. In this review we summarize the progress of various biological and biomedical applications of TiO_2 that hold promise for future medical innovations in molecular medicine.

2. ENERGY BAND STRUCTURE OF TiO_2 NANOPARTICLES

Titanium dioxide exists in three crystal modifications: anatase, brookite, and rutile. All crystalline modifications have different adsorption properties and photoresponses due to different band structures, making their use in biomedical applications dependent on their crystalline form. In bulk state, rutile is the most thermodynamically stable form. Due to its lower thermodynamic stability, few laboratories have accomplished the synthesis of anatase single crystals.⁹ However, in the nanocrystalline regime the anatase crystal structure becomes dominant and plays the most important role in photocatalysis, environmental, and energy applications, therefore holding promise for light-initiated biomedical applications.^{10,11} Anatase crystalline modification is a distorted octahedral coordination (O_h) in which every titanium atom is surrounded by six oxygen atoms in an elongated octahedral geometry (D_{2d}), adopting axial symmetry. In rutile (D_{2h}), due to the Jahn–Teller distortions, additional in-plane (equatorial) and out-of-plane (axial) bond length and bond angle distortions exist, while in brookite stronger distortions lead to a local symmetry loss and formation of C_1 -symmetric TiO_6 units. These different atomic arrangements determine surface and electronic band structures of each polymorph, thus affecting their electron-transfer capability and the redox potentials of photo-induced charge carriers. The 3d levels of Ti^{4+} in octahedral symmetry O_h are split into $3t_{2g}$ and $3e_g$ sublevels due to the existence of the crystal field.¹² In D_{2d} symmetry (anatase), however, the six ligand bonds to titanium are different in length, which produces a splitting of the t_{2g} and e_g orbitals of each TiO_6 octahedra into two additional subsets (Figure 1). However, according to Pauli's exclusion principle, the orbital levels in a bulk crystal acquire energies that are slightly different from each other, forming a subband of states. These energy subbands constitute the conduction band of TiO_2 and appear in the X-ray absorption near edge structure (XANES) spectrum of TiO_2 as the pre-edge structure. Figure 1 (far right) shows predicted pre-edge structures of ideal octahedral O_h symmetry (black), anatase D_{2d} (blue), and rutile D_{2h} (red). As the deviation from centrosymmetry increases, the intensity of the 1s to 3d transition of Ti^{4+} becomes more allowed. In anatase the lowest band in the conduction band of TiO_2 is composed from the $b1$ and e

subbands that have mainly π character and can overlap with valence band oxygen p_{\perp} orbitals in the p-type fashion.

The maximum of the valence band and minimum of the conduction band in the reciprocal space are located in the center, Γ point, of the Brillouine zone (BZ). While in rutile this transition constitutes the lowest energy transition (band gap), in anatase this transition ($\Gamma_3 \rightarrow \Gamma_1$) is dipole forbidden. In anatase the indirect transitions from the M point at the edge of the BZ to the Γ point in the center of BZ is the first allowed transition, making anatase an indirect semiconductor.¹³ The two lowest allowed transitions are both $M \rightarrow \Gamma$ transitions, with energies of 3.026 and 3.06 eV, but the transition of $M2 \rightarrow \Gamma$ with an energy of 3.19 eV is allowed with both parallel and perpendicular direction, increasing the transition probability and therefore constituting the band gap energy of anatase TiO_2 . The curvature of the bands at the maximum of the valence and minimum of conduction bands were found to be small, indicating large effective masses ranging from $5m_0$ to $13m_0$ and from $\sim 2m_0$ to $3m_0$ for valence band holes and conduction band electrons, respectively.^{14–18} However, although large, the effective masses in anatase are still smaller than those of donor electrons in rutile, which is consistent with the high mobility of charges and the band-like conduction observed in anatase crystals. They also account for the very shallow donor energies in anatase.¹⁹ Due to the difficulties in preparation of anatase single crystals the precise value of the electron effective mass in anatase remains elusive. Nevertheless, the relatively large effective masses make the occurrence of the quantization effect in titania particles negligible for particle sizes $> 30 \text{ \AA}$. Moreover, Serpone et al.²⁰ associated the blue shifts observed in small anatase nanoparticles with the changes in the interband transition probabilities. They found that although TiO_2 is an indirect band-gap semiconductor, upon decreasing the particle size to nanosize range, direct (Franck–Condon type) transitions become allowed resulting in blue shifts of absorption spectra experimentally observed in small nanoparticles of TiO_2 . This could have significant implications on the reactivity of small TiO_2 nanoparticles as the excitonic interaction between photogenerated electrons and holes would be less significant than in nanoparticles in which quantization effects prevail, enabling easier charge separation and therefore enhanced chemical reactivity. Another significant feature of TiO_2 particles is that the top of the valence band curvature is larger (sharper) than the one on the bottom of the conduction band.^{16–18} This suggests that the effective mass of the hole is smaller than the effective mass of the electrons (larger Bohr radius for holes than that of the photogenerated electrons). This differs from most semiconductors and can have important consequences for formation of the exciton pairs, a dominant process in small semiconductor particles such as the reverse excitonic interactions between charge carriers in which photogenerated holes orbit around the heavier electrons. This, in turn, would suggest that photogenerated holes are more likely localized to the surface of the small titania particles while electrons would first localize in the particle interior. This was experimentally demonstrated using electron paramagnetic resonance (EPR).²¹

3. IMPORTANCE OF SURFACE SITES IN TiO_2 NANOPARTICLES

The surface of metal oxide materials experiences rearrangement of atom positions with respect to those in the bulk material, due to the abrupt termination of the periodic structure at the surface. This is particularly important for nanoparticles that are smaller than 20 nm. When nanoparticles reach this size range, the

fraction of the surface atoms becomes comparable to the fraction in the bulk and surface atoms begin controlling overall electronic structure. As the coordination sphere of the surface metal atoms is incomplete, surface sites start participating in the charge trapping, thereby reducing the potential of nanoparticles for redox chemistry. The contribution of the surface reconstruction to chemical reactivity of different metal oxide particles (TiO_2 , Fe_2O_3 , ZrO_2 , and ZnO) having particle sizes ranging from 3 to 40 nm was investigated using X-ray absorption spectroscopies (XANES, extended X-ray absorption fine structure, EXAFS).^{22–25} It was found that atoms located at the surface have significantly altered electrochemical properties. Surface atoms, due to truncation of the crystal units, are coordinated with solvent molecules. This coordination with solvent results in a weaker covalent bonding compared to those within the crystalline lattice. This, in turn, moves the energy levels of the surface atoms to the midgap region, thereby decreasing their reducing/oxidizing abilities and affecting the photoreactivity needed for their effective participation in biomedical applications.^{26,27} In addition, it has been found that the surface Ti atoms adjust their coordination environment as the size of nanocrystalline TiO_2 reaches nanocrystalline range.^{23,25} This change in coordination environment is accompanied by a compression of the Ti–O bond and slight extension of the Ti–Ti bond (Figure 2). Importantly, due to the distortions of the crystalline

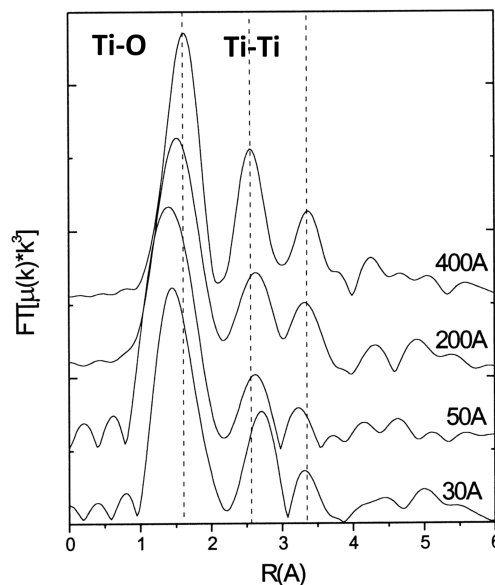


Figure 2. EXAFS spectra of TiO_2 nanoparticles with different diameters. Adapted from ref 25. Copyright 1997 American Chemical Society.

environment, the surface atoms of the metal oxide nanoparticles have a high tendency to bind molecules from their surroundings, suggesting that TiO_2 nanoparticles have a high affinity for binding proteins and other cellular components when introduced to the cellular environment. Additionally, due to the change of the crystalline structure, the electronic structure of the conduction band of nanocrystalline TiO_2 also changes. Modifications in the relative intensities and peak positions in the pre-edge features of the Ti K-edge can be observed as the particle size of nanoparticles is reduced (Figure 3).²⁴ Buildup of the intensity with decreasing particle size was associated with enhanced transition from 1s to 3d levels in Ti that becomes more allowed with the deviation from the centrosymmetry of

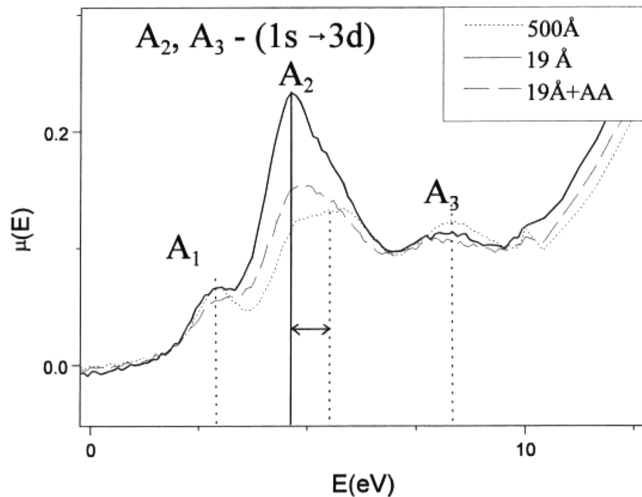


Figure 3. Pre-edge features of Ti K-edge ($E = 4.966$ keV) structure in XANES studies of Ti atoms for different size TiO_2 particles before and after surface modification with ascorbic acid. Reprinted with permission from ref 24. Copyright 1999 American Chemical Society.

TiO_6 octahedra in small particle size nanoparticles. The changes in the bond length (Figure 2) as well as the energy and probability of $1s \rightarrow 1d$ transition (Figure 3) suggest that the coordination of surface Ti atoms changes from centrosymmetric six coordinate (octahedral) in 50 nm particles to five coordinate (square-pyramidal) in small 2 nm particles. This also suggests that the overlap between the p-like valence and the d-like conduction band orbitals in distorted square-pyramidal environment is enhanced, improving the probability of promoting an electron from the nanoparticle surface to the conduction band of nanoparticulate TiO_2 . This behavior is supported by EPR

investigation of small TiO_2 nanoparticles that shows that at helium temperatures (4–10 K) photogenerated holes are always formed at the surface while photogenerated electrons experience a bulk TiO_2 environment. Similar lattice distortions are also found on the tips of anatase anisotropic structures such as nanorods propagating ~5 outmost atomic layers to the particle interior (Figure 4).²⁸ The surface reconstruction in anisotropic structures also changes the environment of surface Ti atoms to an undercoordinated square-pyramidal structure (C_{4v}). Due to the changed coordination environment these atoms become defect sites that display enhanced affinity toward bidentate ligand binding which restores their coordination environment. The undercoordinated surface sites were found to exhibit a high affinity for a variety of bidentate oxygen-rich ligands and provide the opportunity for seamless attachments to the nanoparticle surface. It has been found that biologically relevant molecules such as ascorbic acid, dopamine, and a variety of amino acids bind selectively to these undercoordinated surface sites,^{26,27} offering opportunities for integration of TiO_2 nanoparticles with biomolecules and their use in biomedical applications. Moreover, these undercoordinated sites can also bind molecular oxygens. A recent combined theoretical and experimental study by Setvin et al.²⁹ confirms that molecular O_2 is adsorbed at 5-fold-coordinated undercoordinated Ti sites as a superoxo (O_2^-) species that is transformed to peroxy (O_2^{2-}) site. Such adsorbed oxygen may play a key role in oxidation reactions in photocatalysis and can be envisioned as a key component in ROS formation, critical for light-induced biomedical therapies.

4. NANOPARTICLES AS REDOX ACTIVE CENTERS

Under illumination, TiO_2 particles behave as miniature electrochemical cells capable of light-induced redox chemistry. This opens an opportunity for employing light-induced redox

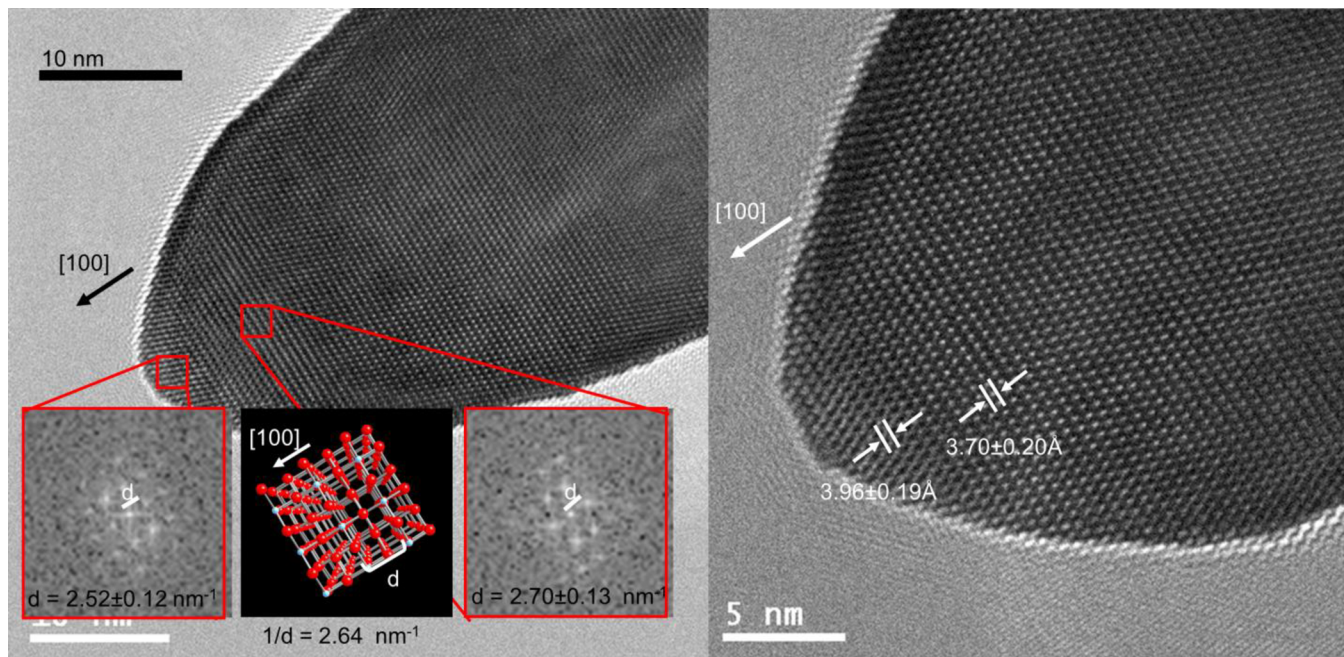


Figure 4. Distortion of the crystalline environment of TiO_2 nanorods at the locations of high curvature. (Left) FFT of the TEM image of the tip area (left inset) and an interior region centered approximately 9 nm from the end of the nanorods (right inset). Middle inset is a representation of anatase crystal structure, showing the (100) $\text{Ti}-\text{Ti}$ distance (d). (Right) Extension of the (001) plane spacing can be seen at the nanorods tip using HRTEM, compared to the normal, relaxed $\text{Ti}-\text{Ti}$ distances seen within the interior area. Adapted from ref 28. Copyright 2006 Wiley-VCH Verlag GmbH & Co. KGaA, Weinheim.

chemistry of TiO_2 nanoparticles to manipulate biomolecules and deliver controlled redox equivalents to participate in the cell metabolic processes. Since the first report of photocatalytic water splitting on TiO_2 electrode under illumination with UV light,³⁰ TiO_2 has been extensively studied in photoelectrochemical applications. Absorption of light with an energy greater than the band gap (3.2 eV for anatase and brookite and 3.0 eV for rutile TiO_2) promotes electrons from the valence band (VB) to the conduction band (CB), leaving electronic vacancies in the valence band, which attract electrons and behave as positively charged holes (Figure 5). These photogenerated electrons and

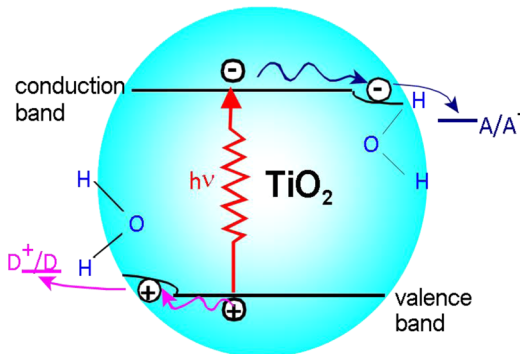
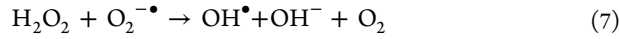


Figure 5. Salient features of the photoinduced redox reactions at the surface of TiO_2 nanoparticles.

holes can undergo recombination or can be transported to the surface of a nanoparticle to react with redox couples in the solution. Therefore, particulate metal oxides have both anodic and cathodic compartments, allowing for both oxidation and reduction of molecules adsorbed at their surface. The efficiency of redox reactions depends on the efficiency of charge separation and reaction selectivity of the photogenerated charge pairs.

The ability of semiconductors to carry out redox reactions upon formation of charge pairs is determined by thermodynamic and kinetic factors. The thermodynamic requirements are given by the position of the conduction and valence band edges. For example, for a reduction of a particular species (A), the conduction band of the semiconductor must be more negative than the potential of a relevant redox couple, while oxidation of a particular species (D) by valence band holes requires that the valence band be more positive than the relevant redox potential. Therefore, the reaction requirement for TiO_2 photocatalysis is that reactive species match the energies of the conduction and valence bands ($E_{\text{cb}} \approx -0.5$ V, $E_{\text{vb}} \approx +2.7$ V vs NHE at pH 7, respectively for anatase TiO_2).³¹ Kinetic requirements are dominated by the carrier diffusion and adsorption of reactants. Anatase TiO_2 nanoparticles fulfill these requirements and offer distinct advantages in the heterogeneous photocatalysis process: (1) high absorption cross section of the incident photons; (2) fast carrier diffusion; (3) high adsorption of redox species due to the undercoordination of surface Ti sites; (4) ease of the change of the crystalline environment with the valence state change; and (5) suitable redox levels of the valence and conduction band edges that can yield high efficiencies in converting light energy to useful redox events. However, due to the surface reconstruction in the nanosize regime, a large fraction of the atoms that constitute the nanoparticle is located at the surface with altered electrochemical properties.^{26,27} Because of the truncation of the periodic crystalline structure at the surface and weaker covalent bonding of surface atoms compared to the lattice atoms, the

energy level of the surface species is found in the midgap region.³² These surface states behave as donor or acceptor sites, and thus, photogenerated charge carriers tend to localize at the surface of the semiconductor, thereby decreasing their reducing/oxidizing abilities and the efficiency of their redox reactions. In the presence of oxygen, illumination of TiO_2 in aqueous solutions results in formation of oxidative radical species with different redox properties and different reactivities. While photogenerated holes react with free and surface-adsorbed H_2O to produce hydroxyl radicals, the strongest existing oxidative species with $E_{\text{ox}} = 2.7$ V vs NHE, photogenerated electrons are scavenged by molecular O_2 to yield superoxide radical anions. These reactions are exceptionally efficient in TiO_2 solutions and form a basis for widespread use of TiO_2 in environmental applications



These radical species have different redox properties, diffusion coefficients, and diffusion distances. For example, OH^\bullet radical has the strongest oxidation potential and a large diffusion coefficient, however, due to the high reactivity, the diffusion distances of OH^\bullet radicals as well as the one for singlet oxygen (${}^1\text{O}_2$) in water are fairly small (<20 and 20–220 nm, respectively).^{33,34} On the other hand, superoxide radical ($\text{O}_2^{\cdot-}$) and H_2O_2 have moderate oxidation potentials, but their diffusion distances can reach up to hundreds of micrometers.³⁵ Due to the variety in reactivity and redox properties, all of these radicals can participate in decomposition of many different organic species with which they make close contact or with which they encounter at large distances from the locations of their formation. These considerations are very important for biomedical applications of TiO_2 redox chemistry, suggesting that only those radicals that can reach active cell components will affect cell functioning. Highly reactive OH^\bullet radicals will disappear very fast either in the recombination reaction or in a reaction with arbitrary electron-donating molecules in the TiO_2 vicinity resulting in loss of its activity. However, moderately reactive superoxide radicals $\text{O}_2^{\cdot-}$ would be able to diffuse and reach cell organelles, ultimately influencing cell functioning.

5. CHARGE SEPARATION IN TiO_2 REDOX ACTIVE CENTERS: EPR SPECTROSCOPY

Electron paramagnetic resonance (EPR) is a powerful, versatile, and nondestructive method that yields structural, electronic, and dynamical information. It utilizes physical interactions of the electron spin (S) with a nucleus spin (I) in the external magnetic field (B). EPR has been utilized for understanding the mechanisms of a variety of biological processes such as photosynthesis,^{36,37} lipid oxidation,³⁷ or enzymatic formation

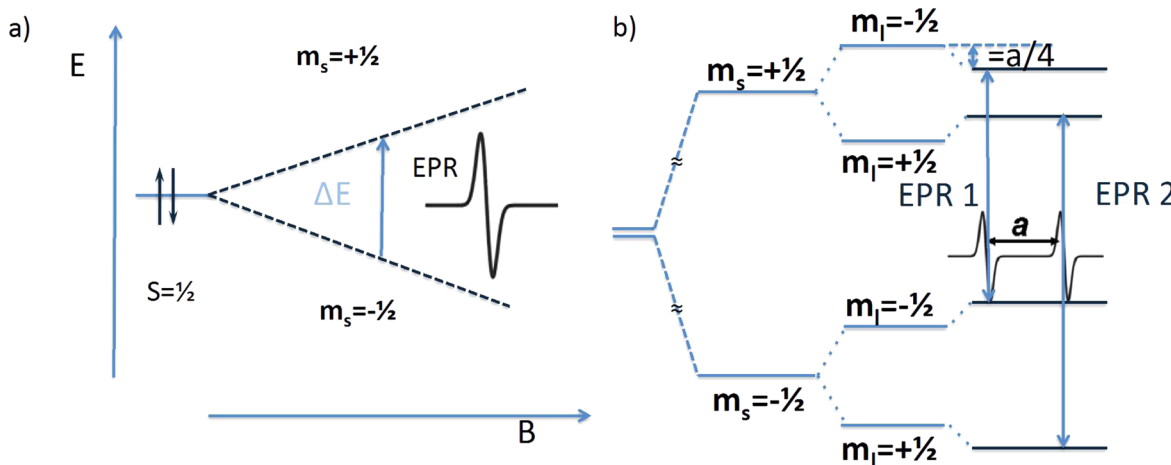


Figure 6. Energy-level scheme of (a) an electron with spin $S = 1/2$ as a function of the applied magnetic field B and (b) an electron interacting with a nucleus with a nuclear spin $I = 1/2$.

of superoxide by xanthine oxidase.³⁸ It also permits *in vivo* studies of free radicals, which are intrinsically paramagnetic species as they have unpaired electrons in one of their orbitals. Unpaired spins interact with external magnetic fields, and because the electron has a magnetic moment, it orients in an external magnetic field. It will have a state of lowest energy when the magnetic moment of the electron, μ , is aligned with the magnetic field, $m_s = -1/2$, and a state of highest energy when μ is aligned against the magnetic field, $m_s = +1/2$. The difference between these levels, the *Zeeman splitting*, is the most fundamental interaction in EPR (Figure 6a) and increases with the magnetic field intensity. The energy between the two Zeeman levels is

$$\Delta E = h\nu = g\mu_B B \quad (9)$$

where μ_B is a Bohr magneton and the g factor is a constant of proportionality (that can be different for different crystal orientations g_x , g_y , and g_z). If the resonance condition is fulfilled, namely, if the energy of the microwave irradiation used for examining the system, $h\nu$, matches the energy between the two levels ΔE , absorption of photons induces transitions between the two spin states, resulting in a spin flip from the orientation parallel to the magnetic field ($-1/2$) to the one antiparallel to the field ($1/2$) and consequently producing an absorption peak in the EPR spectrum. Since the EPR spectrum in the solid state will depend on the relative orientation of the applied field with respect to the paramagnetic species, the local magnetic field experienced by the electron spin is further influenced by the magnetic moments of the nearby nuclei. This coupling between electron spin and nuclear spin, a so-called hyperfine (HF) interaction, splits the electron Zeeman levels into the hyperfine levels (Figure 6b). Additional interactions may further affect the absorption spectra, and the overall spin Hamiltonian can be written as

$$H = H_{EZI} - H_{NZI} - H_{HFI} = g\mu_B BS_Z - g_N\mu_N BI_Z + h \cdot aS \cdot I \quad (10)$$

where the first term describes the electron Zeeman interactions (EZI), the second term describes the nuclear Zeeman (NZI), and the third term represents the hyperfine interaction (HFI). S is the spin quantum number, I is the nucleus spin, h is Planck's constant, and the term $aS \cdot I$ is introduced by the Fermi contact interaction. Depending on the electron and nuclear spin

quantum numbers additional terms for zero-field splitting accounting for dipole–dipole interaction of electrons in the systems with $S > 1/2$ and nuclear quadrupole interactions that accounts for nuclei with a nuclear spin quantum number $I > 1/2$ have to be incorporated into the spin Hamiltonian. The number of EPR lines is $2I + 1$ when one unpaired electron interacts with one nucleus. When one unpaired electron interacts with N equivalent nuclei, the number of EPR lines is $2NI + 1$. When one electron interacts with nonequivalent nuclei, the number of EPR lines is given by the expression

$$\text{number of EPR lines} = \prod_{i=0}^k (2N_i + 1) \quad (11)$$

where k is the number of nonequivalent nuclei.

Although the overall spectrum may have a number of components, it is a “fingerprint” of the paramagnetic species that reports on the environment where radical species are located.³⁹ EPR spectroscopy is well suited for studying processes *in situ* yielding to structural, electronic, and dynamical information, without influencing the process itself. The EPR technique is uniquely suited for studying TiO₂ redox centers formed upon illumination because it provides unambiguous identification of the nature of both reducing and oxidizing active sites, their coordination, and the oxidation states, and it enables differentiation between surface and bulk sites. This is especially important for studying the photocatalytic activity of TiO₂ in complex environments as EPR is the only technique that simultaneously reports the coordination environment of both electrons and holes, enabling an estimate of their separation distances. This, in turn, enables assessments of their recombination rate and provides pathways for enhancing charge separation distances. As a consequence, EPR has been widely used in monitoring the presence, stability, and reactivity of charge carriers in TiO₂ formed under illumination starting from the early studies of Howe and Gratzel.^{40,41} Paramagnetic centers created by photoexcitation of TiO₂ have spin and orbital magnetic moments that report on both the character of the orbitals in which they reside and their environment through hyperfine splitting, spin–lattice interactions, and g anisotropy.⁴² The technique provides direct identification of the local structure along the pathway of the photogenerated charges and is very sensitive to even small structural changes, for example, between

anatase and rutile samples or electrons in the interior or on the surface of nanoparticles (Figure 7).

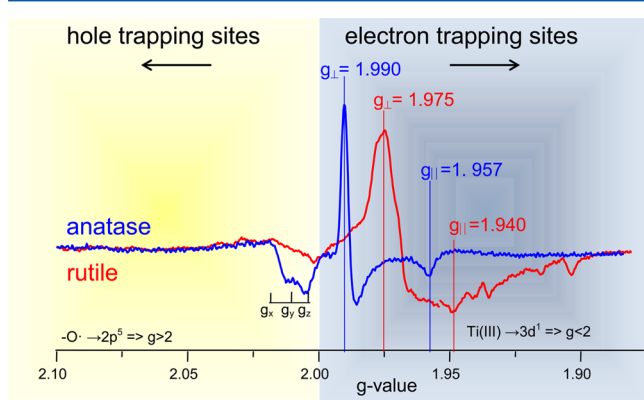


Figure 7. EPR spectra of anatase and rutile nanoparticles recorded under illumination at 4.5 K. Electrons are trapped at lattice sites as Ti^{3+} (showing axially symmetric signal), while holes are trapped at the surface of nanoparticles as oxygen-centered radicals (showing the asymmetric signal). Due to the different symmetry of titanium cation in anatase (D_{2d}) and rutile (D_{2h}), the EPR spectra of these nanoparticles can be clearly distinguished.

In this sense, the EPR technique brings coordination chemistry concepts of exchange interactions and transition metal ligand coordination to consideration of the processes taking place on metal oxide surfaces.^{43,44} Moreover, EPR enables *in situ* identification of the reaction intermediates as well as charge transport studies in hierarchical heterostructures.^{21,45,46} Great efforts were made to improve understanding of the state and localization of surface-stabilized carriers on TiO_2 , including identification of highly reactive Ti^{3+} tetrahedral sites in mixed-phase TiO_2 ,^{21,47,48} and five-coordinate sites on the surface of anatase nanoparticles using continuous wave EPR spectroscopy.^{24,49} While these studies dealt with the nature and structure of the redox active centers, an understanding of the spin dynamics requires the use of advanced pulsed EPR techniques. It has been shown in many studies of the optimized photoactive systems such as natural photosynthesis that spin multiplicity plays an important role in charge separation and therefore in efficiency of photochemical reactions. Using an electron spin echo envelope modulation (ESEEM) pulsed EPR technique, we demonstrated that hole dynamics are associated with oxygen atoms at the nanoparticle surface and influenced by the interaction with nuclear spins from water molecules.⁵⁰ Being on the surface, they interact through weak dipolar coupling with surrounding hydrogen nuclei from adsorbed water molecules, observed as the Larmor frequency of ${}^1\text{H}$ nuclei, shown in Figure 8. At the same time, the absence of this proton frequency in ESEEM of trapped electrons further verifies that electrons formed at 4.2 K localize in the bulk, at least >0.5 nm from the nanoparticle surface, and their dynamics are influenced solely by the lattice vibrations. This initial electron–hole pair configuration in which electrons are localized within the interior of the anatase crystals and the holes are located on their surface suggests that in order for a photocatalytic reaction to be efficient an oxidation reaction should occur first (e.g., biological molecules at the surface that are usually easily oxidized) followed by the reduction reaction (e.g., oxygen molecules). This electron–hole interplay in addition to spin dynamics that foster longevity of electron–hole pairs are key factors contributing to the high efficiency of photocatalytic

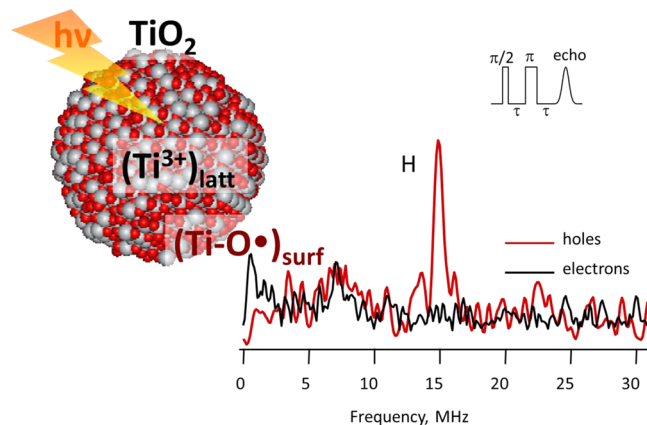


Figure 8. ESEEM spectra of TiO_2 nanoparticles obtained after 355 nm excitation recorded at a resonant field of photogenerated holes (brown) and electrons (black). The peak at 14.9 MHz (H frequency) demonstrates that hole centers (O^\bullet) are subjected to weak dipolar coupling with surrounding ${}^1\text{H}$ nuclei from adsorbed water. Adapted from ref 50. Copyright 2007 American Chemical Society.

reactions on titania nanoparticles. Many semiconducting nanoparticle systems have been studied with the prospect of finding an alternative system capable of exceeding photocatalytic activity obtained by TiO_2 . However, so far none of the investigated systems had such an efficient light-induced charge separation integrated with advanced catalytic properties. It has been demonstrated repeatedly that TiO_2 nanoparticles are the most photocatalytically efficient (in terms of quantum yield defined as the number of events per absorbed photon) and therefore *best suited for successful application of a photocatalytic approach in light-stimulated timed release of therapeutic agents for biomedical applications*.

6. EFFECT OF SIZE AND SHAPE ON BULK AND SURFACE PROPERTIES OF ANATASE NANOPARTICLES

The ability to systematically manipulate the shape and size of metal oxide nanoparticles allows for control of their electronic and chemical properties, resulting in new venues for more efficient site-selective chemistry. The size and shape strongly influence particle crystallinity that, in turn, controls electron/hole transport and charge separation, a prerequisite for efficient use of absorbed photons in redox reactions. The size and shape of nanoparticles also determine the nature of localized charge carriers that, in turn, regulate the redox properties of nanoparticles. Finally, the size and shape of crystalline particles determine exposed crystalline planes that govern adsorption and interaction of molecular species controlling nanoparticle selectivity and efficiency of photocatalytic processes.

Anisotropic TiO_2 nanostructures such as rods, bricks, and tubes as well as spherical and faceted nanoparticles have been developed in our laboratory and elsewhere.^{51–54} Recently, highly uniform anatase TiO_2 nanocrystals were obtained using a nonaqueous surfactant-assisted synthesis. A seeded growth technique was used to obtain nanoparticles with tailored morphologies in the 10–100 nm size range.⁵⁵ It was found that introduction of titanium(IV) fluoride (TiF_4) to the synthesis resulted in preferential exposure of the 001 facets of anatase, while control of a surface modifier binding group (amino vs OH group) controlled exposure of 101 facets. *In situ* release of hydrofluoric acid (HF) during synthesis allowed formation of

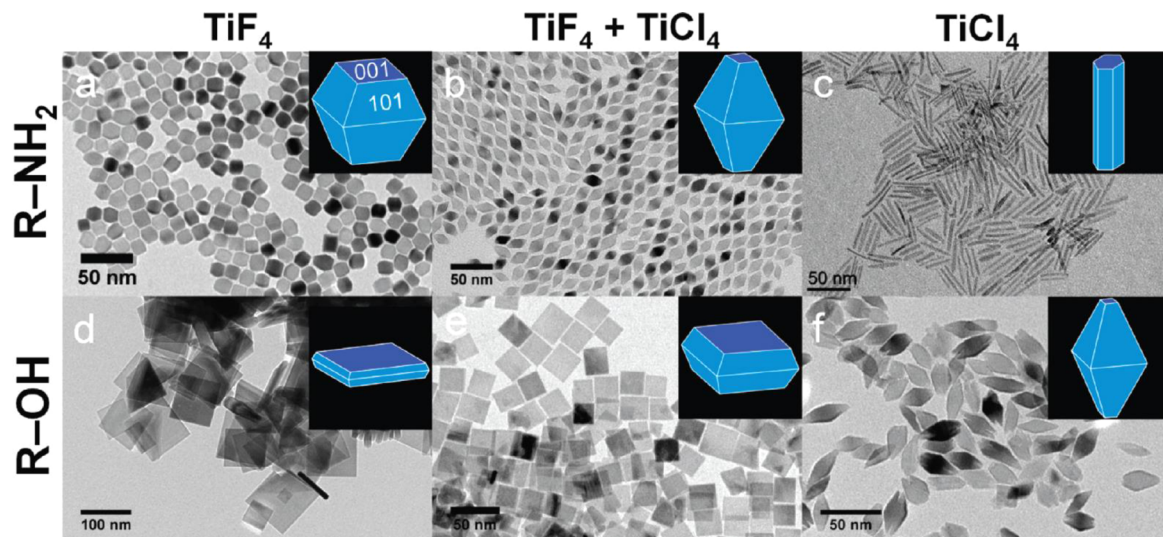


Figure 9. TEM images of anatase nanocrystallites. Adapted from ref 55. Copyright 2012 American Chemical Society.

uniform anatase nanocrystals based on the truncated tetragonal bipyramidal geometry (Figure 9). These nanoparticles also exhibit a blue color characteristic of the presence of excess electrons. Oxygen vacancies or titanium interstitials, which are formed during the synthetic process, were suggested to be the source of additional electrons.

TiO₂ nanostructures exhibit different surface areas and surface-to-bulk aspect ratios depending on their size and shape. Moreover, the coordination and structure of Ti surface atoms and thus the nature of surface defects is expected to depend on the size and shape of the nanocrystallites. We applied our initial discovery of the difference between the structure of Ti atoms at the surface and the bulk of anatase spherical nanoparticles using X-ray absorption techniques^{24,25} to the study of the local structure of anisotropic TiO₂ nano-objects. We investigated low-temperature charge separation in differently shaped nano-TiO₂ using EPR spectroscopy. The spectra shown in Figure 10 indicate a different distribution of electron density in TiO₂ nano-objects under illumination. While the signals from surface-trapped holes change only slightly within different shapes of anatase particles (localized on surface oxygen atoms), there is a distinct change in g-tensor values of lattice-trapped electrons, $(\text{Ti}^{3+})_{\text{latt}}$, demonstrating the influence of the surface states in collective conduction band states.

Brick-like and faceted structures have a perpendicular component of lattice electrons $g_{\perp} = 1.992$ that is characteristic of bulk anatase crystals, and it changes to $g_{\perp} = 1.989$ for spherical particles and 300 nm elongated rods containing five-coordinated Ti³⁺ sites at the regions of high curvature.²⁸ This suggests that the small changes of surface structure, like the presence of undercoordinated Ti sites, “spill over” from the surface and affect g values of bulk $(\text{Ti}^{3+})_{\text{latt}}$ showing the delocalized nature of electron orbitals in which spins reside. Additionally, we found that the parallel component $g_{\parallel}^2 = 1.958$ assigned to localized Ti³⁺ sites disappears in the faceted and brick-like nanocrystallites. Only the motionally narrowed signal associated with electron hopping from one center to another,²⁴ $g_{\parallel}^1 = 1.961$, prevails (Figure 10, inset). These changes are not affected by the size (different nanoparticles with sizes below 20 nm show the same g-tensor values) but rather by the shape of the nano-objects.

The observed difference in g-tensor values is the consequence of the deviations in the lattice structure and the lattice spacing

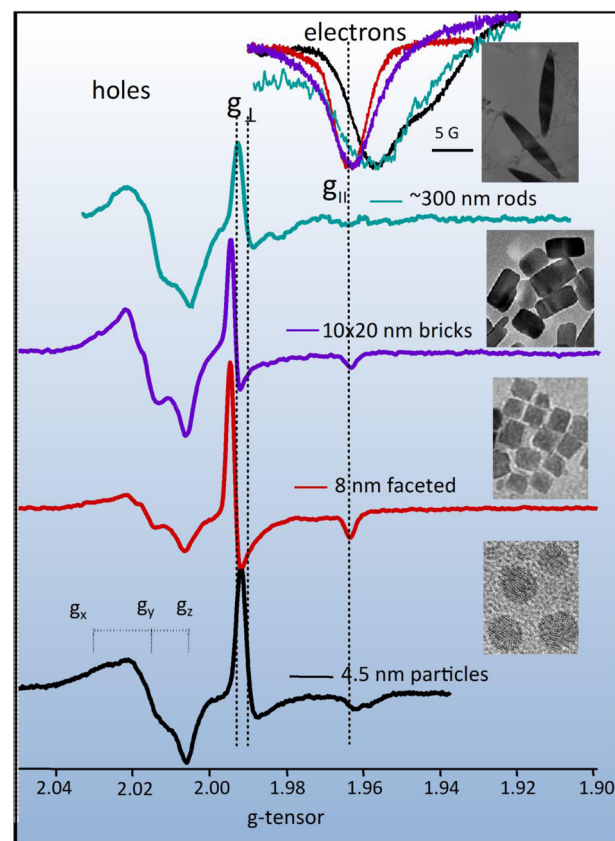


Figure 10. EPR spectra of TiO₂ nano-objects under monochromatic excitation (355 nm, Nd:YAG laser). Temperature 4.5 K. (Inset) Spectra of a parallel component of signal corresponding to trapped electrons in anatase nano-objects.

that is affecting the local environment of surface and interior trapping sites. Meriaudeau et al.⁵⁶ applied the angular overlap model to the electrons in Ti 3d orbitals of the anatase lattice and showed that a strong π -antibonding effect of one or two oxide ligands of a Ti³⁺O₆ paramagnetic center is responsible for the deviations in g-tensor values. We found that distortions of a Ti–O bond, resulting from reconstruction of the surface of spherical nanoparticles and at the points of high curvature (tips) of

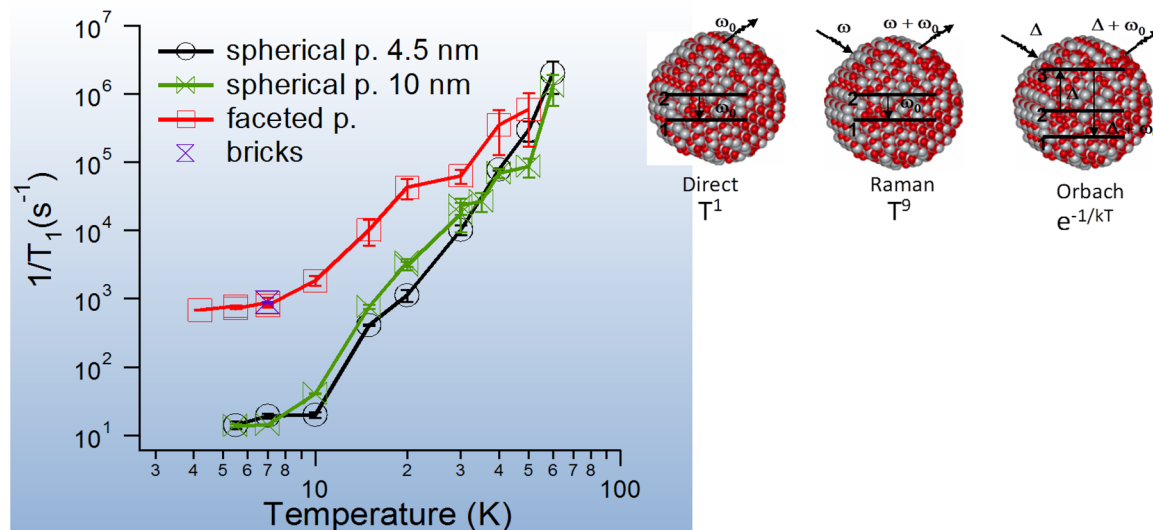


Figure 11. Temperature dependence of spin–lattice relaxation time T_1 for trapped electrons. Reprinted with permission from ref 50. Copyright 2007 American Chemical Society.

elongated rods, cause the changes in g -tensor values of $(\text{Ti}^{3+})_{\text{latt}}$ from the values in the bulk TiO_2 .^{28,49} In particular, the lattice distortion shown in Figure 4 encompassing elongation along the [100] direction at the tips of long nanorods (from $3.78 \pm 0.20 \text{ \AA}$), and contraction along (104) (from $2.0 \pm 0.09 \text{ \AA}$) and (102) planes (from $2.94 \pm 0.14 \text{ \AA}$) causes deviation of the g values in nanorods.²⁸ These alterations of bond lengths results in the distortion of the symmetry of the Ti atom to square pyramidal, as opposed to the symmetry of bulk TiO_2 , which is known to be octahedral. The same changes in symmetry have been observed for the 4.5 nm spherical particles.²⁴ Accordingly, the high curvature of both spherical and rod-like nano-objects that promotes distortion of the Ti–O bond also yields the similar EPR spectra of trapped electrons for both nanoparticle shapes. For faceted and brick-like crystallites, we observed a shift of the g -tensor values of the $(\text{Ti}^{3+})_{\text{latt}}$ signal toward “bulk” electrons, suggesting a negligible concentration of five-coordinated Ti sites, i.e., negligible changes in Ti–O bond lengths. Thus, these faceted nano-objects exhibit more ordered crystalline structure, and the increase in size from ~ 8 to 20 nm does not affect their g -tensor values. On the other hand, as holes are localized oxygen-centered radicals ($\text{Ti}^{4+}\text{O}^{\bullet}_{\text{surf}}$)^{49,57,58} they are not affected by the size and shape of nano-objects. Strong localization on the surface oxygen atoms also indicates that holes are confined to energetically deep sites within the midgap state independent of the size or shape of nanoparticles. These results suggest that the nanoparticles with high curvature have superior properties for selective binding of ligands, which complete coordination of five-coordinated states, but have a reduced crystalline quality that results in a fair electron transport. On the other hand, faceted nanoparticles have defect-free crystalline properties that result in a superior electron/hole transport, but their binding properties are not as good as those of spherical nanoparticles. For biomedical applications integration/binding of nanoparticles with biological molecules is of the greatest importance, as a nanoparticle–biomolecule construct has to survive interactions with diverse body–fluid components as it transits its intended target site. The strength of the interaction between components within a nanoparticle conjugate therefore has to be stronger than any of the interactions with the proteins and lipids that conjugate encounters along its pathway. Undercoordinated sites that are present in high-curvature

nano-particles (spherical, nanorods) are the most reactive sites that can be used for binding nanoparticles to biomolecules. Although their crystallinity is not as high quality as those of faceted nanoparticles, they are the particles of choice for biomedical applications.

The structural deformations associated with the presence of five-coordinated Ti sites at the surface of nanoparticles affect the interaction of photogenerated electrons with lattice phonons, influencing spin–lattice relaxation times, T_1 . Spin–lattice relaxation is responsible for the lifetime of spin multiplicity that determines the longevity of the electron–hole separation, thereby directly influencing photocatalytic efficiency. Relaxation is facilitated by modulations of the crystal field by phonons (lattice vibrations) transmitted to the electron magnetic moment through spin–orbit coupling.⁵⁹ Equation 12 summarizes different relaxation processes and their temperature dependence

$$\frac{1}{T_1} = A_{\text{dir}} T + A_{\text{Ran}} \left(\frac{kT}{h} \right)^{7+d} \int_0^{\Theta_D/T} \frac{x^{6+d} e^x}{(e^x - 1)^2} dx + A_{\text{orb}} e^{-\Delta/kT} \quad (12)$$

where T is the temperature in Kelvin, Θ_D is the Debye temperature, and A_{dir} , A_{Ran} , and A_{orb} are the coefficients for the contribution from the direct (one-phonon resonant), Raman (two-phonon nonresonant), and Orbach (two-phonon resonant) processes, respectively. In Raman-type relaxation, $d = 0$ (non-Kramers ions) or 2 (Kramers ions) and the transport integral is taken over by the Debye phonon spectrum.

The results of the biexponential fit of the signal recovery in three-pulse echo experiments measured from 4.2 to 70 K are presented in Figure 11 as dependence of $1/T_1$ on the temperature T .⁵⁰ At temperatures below 10 K, there is a linear dependence of $1/T_1$ with temperature ($1/T_1 \approx T$) which is characteristic of the direct one-phonon resonant process and as such is expected to depend on the size of crystallites. This was observed for metal oxides in $100 \mu\text{m}$ size range.⁶⁰ However, we did not observe changes in spin–lattice relaxation times with size in the nanoscale range; rather, again the dependence was on the shape of nano-objects. The measured spin–lattice relaxation times are the same for 4.5 and 10 nm spherical particles and 2 orders of magnitude slower than the one measured for faceted

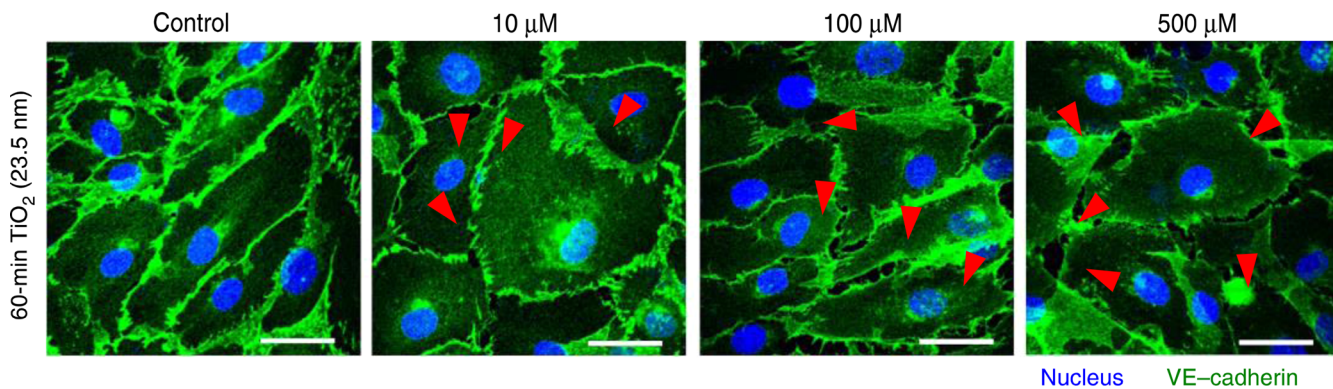


Figure 12. TiO_2 nanoparticles induced epithelial cell leakage (red arrowhead) after cell treatment with various concentrations of TiO_2 recorded 60 min after exposure. Nuclei were visualized by 40,6-diamidino-2-phenylindole (blue), while VE-cadherin in adherens junctions was visualized with immunofluorescence (green). Adapted from ref 63. Copyright 2013 Rights Managed by Nature Publishing Group.

particles of similar size. As spherical nanoparticles exhibit relatively high concentration of five-coordinated Ti atoms at the surface, even the small changes in Ti–O distances affect the lattice vibration energies. At low temperatures, spin–lattice relaxation is dominated by resonant interactions with low-energy phonons. Thus, the effect of different shape is the most pronounced. In distorted anatase structures the number of low-energy phonons is limited compared to faceted particles, accounting for slow spin–lattice relaxation times.

At higher temperatures, the relaxation follows the power law which is characteristic of the nonresonant two-phonon Raman process. As a nonresonant process, it depends on the number of phonons (according to the Debye spectrum at a given temperature). With the increase in temperature the number of available phonons for interaction with photogenerated electrons increases, and eventually the difference that arises from the various shapes of nanocrystallites diminishes at ~ 50 K. $1/T_1$ varies with temperature as $\leq T^6$ over a broad temperature range, which is much slower than the T^9 variation expected for Kramers ion, such as Ti^{3+} , suggesting a relaxation mechanism through a phonon-modulated hyperfine coupling.⁶¹ Data at higher temperatures shows that the dynamical coupling of $(\text{Ti}^{3+})_{\text{latt}}$ to the crystal field is weak. The weak coupling confirms the relatively high mobility of photogenerated electrons. This is supported by findings that electrons are initially trapped in energetically shallow lattice traps, some 20 meV below the conduction band, and can migrate through hopping even at relatively low temperatures.⁶²

The distortion of the Ti–O bond caused by reconstruction of the surface to accommodate the shape of TiO_2 nano-objects greatly affects the spin properties of photogenerated lattice-trapped electrons. Although these findings have been obtained at cryogenic temperatures, they have implications on room-temperature photocatalysis, since lowering the temperature mainly changes the kinetics but not the pathway and properties of photogenerated charges in TiO_2 . The different spin dynamics observed for differently shaped anatase nano-objects imply a difference in the efficiency of charge separation, charge mobility, and electron–hole recombination. The spin relaxation processes discussed above indicate higher mobility and suppressed charge recombination in faceted particles compared to spherical particles of the same size, in analogy to natural photosynthesis, where electron spin correlation slows down spontaneous decay of the charge-separated state.⁴² The presence of five-coordinated sites thus promotes recombination of photogenerated charges in

bare particles, lowering the efficiency of the desired photocatalytic reactions. However, the high affinity of under-coordinated Ti atoms toward oxygen-containing ligands enhances adsorption/binding of such molecules, introducing changes in the mechanism and efficiency of photocatalytic reactions, in particular those relevant for biomedical applications.

7. TOXICITY OF PRISTINE TiO_2 NANOPARTICLES

A recent study of Setyawati et al.⁶³ showed that titanium dioxide nanoparticles (~ 25 nm) cause endothelial cell leakiness (ECL) even when they are not excited by light, while microcrystalline TiO_2 particles (~ 650 nm) do not disrupt the endothelial cell layer. Endothelial cell leakiness was found to be a consequence of the disruption of the adherens junctions upon interaction of endothelial cells with TiO_2 nanoparticles (Figure 12). Endothelial cells line the interior of blood vessels and function as gatekeepers for nutrients, waste, and cell movement. Endothelial cell dysfunction is implicated in tumor cell metastasis and chronic vascular disease.^{64,65} The integrity of the endothelium is dependent on adherens junctions between endothelial cells and facilitated by homophilic transcellular interactions between vascular endothelial (VE) and cadherin, the major adherens junction adhesion molecule that controls cell adhesion. It was found that the physical interaction between bare TiO_2 nanoparticles and endothelial cells alters the adherence junction. Nanoparticles could migrate into and disrupt the barrier between endothelial cells in cell cultures and *in vivo*. Leakiness of the endothelial cells was explained by the disruption of the homophilic interaction of VE–cadherin by TiO_2 nanoparticles. Actin rearrangement upon binding of TiO_2 might induce changes in cell shape, causing leakiness between neighboring endothelial cells. The authors postulated that nanoparticles might alter phosphorylation of VE–cadherin at intracellular tyrosine residues (Y658 and Y731), which modulates interaction with p120 and β -catenin needed for cell adhesion. This would, in turn, promote actin remodeling and degradation of VE–cadherin.

The effect of TiO_2 nanoparticles on cell leakiness was also tested in an *in vivo* setting. Injected nanoparticles induced leakiness in subcutaneous blood vessels in mice (Figure 13) and increased the number of pulmonary metastases in a melanoma-lung metastasis mouse model. These findings demonstrated a new receptor-independent mechanism by which nanomaterials can cause endothelial cell leakiness by triggering an intracellular signaling cascade.



Figure 13. TiO_2 nanoparticles induce leakiness of a subcutaneous blood vessel *in vivo* promoting increased Evan's blue dye extravasation at the subcutaneous vasculature on the back of mice. Adapted from ref 63. Copyright 2013 Rights Managed by Nature Publishing Group.

Other studies also indicate that very small bare anatase nanoparticles (10 and 20 nm) can induce increased hydrogen peroxide/nitric oxide production, oxidative lipid peroxidation, DNA damage, and micronuclei formation in a human bronchial epithelial cell line in the absence of photoactivation.⁶⁶ Trouiller et al.⁶⁷ using a mouse model also investigated the effects of bare TiO_2 nanoparticles on oxidative DNA damage and genotoxicity. Bare dispersed Degussa P25 TiO_2 nanoparticles (~ 20 nm) were administered in drinking water to wild-type mice. After treatment the authors assessed DNA damage by a variety of methods in different cell types. TiO_2 nanoparticles, in a concentration-dependent manner, increased double-strand breaks in bone marrow cells, as measured by an increase in histone H2AX phosphorylation. Administration of $50 \mu\text{g}/\text{mL}$ TiO_2 nanoparticle solution, the lowest concentration tested, produced a significant increase in the percentage of γ -H2AX-positive cells. Peripheral white blood cells also showed increased single- and double-strand breaks, and erythrocytes from peripheral blood showed a higher frequency of micronuclei but only at the highest dose of TiO_2 nanoparticles ($0.5 \text{ mg}/\text{mL}$). The transgenic mice used in this study also facilitated monitoring the effect of *in vivo* exposure to TiO_2 nanoparticles via a retinal pigment epithelium eye-spot

test. The eye-spot test permits monitoring of DNA deletions, which cause a reversion of the pink-eyed locus to the melanin-producing form. Livers of TiO_2 nanoparticle-treated mice had a 1.5-fold increase in DNA oxidative damage relative to untreated mice as indicated by increased levels of 8-hydroxy-2'-deoxyguanosine. Because the nanoparticles induced proinflammatory cytokines and oxidative DNA damage, the authors speculated that genotoxicity may occur through an indirect mechanism.

While the above-discussed study suggested the existence of the toxicity of TiO_2 particles, the study also stated that human studies have not been able to detect any relation between TiO_2 occupational exposure and the cancer risk.⁶⁷ Several other studies failed to detect toxicity of TiO_2 particles at concentrations below $1 \text{ mg}/\text{mL}$,^{8,68} making the current status of our knowledge inconclusive. The above-discussed toxicity studies involve bare TiO_2 with sizes that are in the nanoscale range, suggesting that bare TiO_2 nanoparticles can have significant binding to cell receptors and induce inflammatory responses. The same effects were not observed when microcrystalline TiO_2 was used. These findings can be understood by taking into account the unique surface chemistry of TiO_2 nanoparticles that are largely determined by the reactive undercoordinated Ti atoms that were discussed in the previous sections. Undercoordinated sites were shown to be highly reactive toward oxygen-rich ligands as they fill their octahedral coordination sites with OH groups.⁶⁹ If undercoordinated sites are reacted with bidentate surface active molecules or proteins *in vitro* before they are introduced into the tissue, however, their reactivity with cellular proteins will be minimized, reducing potential particle toxicity. The surface-active molecules can also be used to bring site selectivity and functionality to the redox active TiO_2 nanoparticles. Future research involving surface modification of nanoparticles needs to establish the applicability of these findings more broadly. We

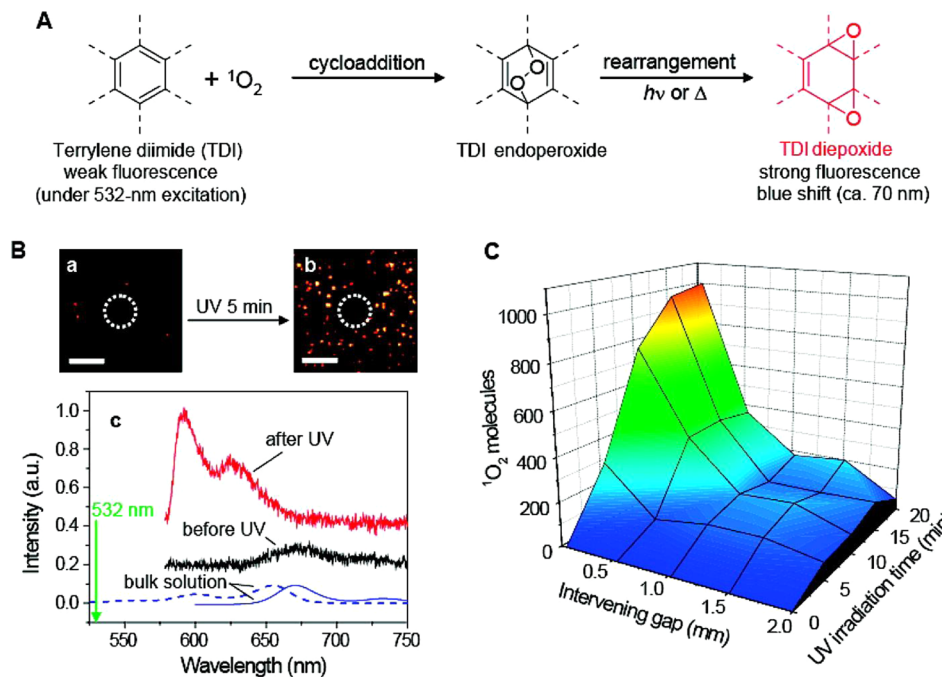


Figure 14. (A) Single-molecule detection of ${}^1\text{O}_2$ with TDI. (B) Fluorescence imaging of TDI before (a) and after (b) UV irradiation (scale bars are $10 \mu\text{m}$). Blue-shifted fluorescence TDI diepoxy is shown with the bright spots. The absence of fluorescence at the center of the image after UV irradiation is due to the bleaching of TDI caused by the direct UV irradiation. (C) Temporal and spatial distributions of ${}^1\text{O}_2$ that diffused from the surface of the TiO_2 film. The observation region is $70 \times 70 \mu\text{m}^2$. Reprinted with permission from ref 35. Copyright 2009 American Chemical Society.

need to determine if nanoparticle surface modification can reduce the adverse interactions of modified TiO_2 nanoparticles with surface receptors that could compromise cell function.

8. PHOTOTOXICITY OF TiO_2 NANOPARTICLES: GENERATION OF REACTIVE OXYGEN SPECIES

All TiO_2 nanoparticles, independent of their size and shape, exhibit phototoxicity. Recently, it has been determined that TiO_2 -induced cell death was inversely proportional to the TiO_2 particle size and that particles in the nanosize range induce the highest level of cell death.⁶⁸ It has also been shown that cell damage was dependent on the crystalline form of TiO_2 with rutile causing less phototoxicity than anatase TiO_2 particles. Furthermore, cell membrane damage and subsequent photocytotoxicity was dependent on the level of reactive oxygen species (ROS). By employing EPR oximetry with immuno-spin-trapping as a unique probing technique, the authors demonstrated that UVA irradiation of TiO_2 nanoparticles can induce significant bimacromolecular damage, in particular to the polyunsaturated lipids in plasma membranes and human serum albumin. The damage was mediated by lipid and protein peroxidation during UVA irradiation.

As mentioned earlier, photoexcitation of TiO_2 in aqueous solution results in formation of various ROS such as hydroxyl (OH^\bullet), superoxide anions ($\text{O}_2^{\cdot-}$), hydroperoxyl (HO_2^\bullet) radicals, and hydrogen peroxide (H_2O_2).^{70–73} Excitation of TiO_2 nanoparticles larger than 10 nm also resulted in formation of singlet oxygen (${}^1\text{O}_2$) as confirmed by measuring the phosphorescence of ${}^1\text{O}_2$ at 1260 nm.⁷⁴ Upon TiO_2 excitation, photogenerated holes localize on the surface, oxidize surrounding water, and produce OH^\bullet radicals due to the large positive potential of the valence band. The alternative pathway for formation of OH^\bullet radicals is a photoreaction of hydrogen peroxide with superoxide radical,⁷⁵ whereas superoxide radical $\text{O}_2^{\cdot-}$ is formed when photogenerated electrons react with oxygen molecules. Majima et al.³⁵ used oxidation of terrylenediimide (TDI) derivative by singlet oxygen ${}^1\text{O}_2$ to determine production of ${}^1\text{O}_2$ in nanocrystalline TiO_2 films (Figure 14A). They showed that oxidation of TDI with singlet oxygen results in formation of endoperoxide, a molecule with reduced fluorescence, that further transforms into diepoxide, a strongly fluorescent molecule whose fluorescence is blue shifted compared to TDI and can easily be detected upon 532 nm laser excitation.⁷⁶ Figure 14B shows images of the single-molecule fluorescence observed 5 min after UV irradiation of the TiO_2 films. It can be seen that only a few fluorescent spots were visible before UV irradiation, as TDI has only a weak luminescence when excited at 532 nm. After UV irradiation, however, bright fluorescent spots emerged around the UV-irradiated region. The change in the fluorescence pattern was attributed to formation of TDI diepoxide, formed by the cycloaddition reaction between ${}^1\text{O}_2$ generated during the TiO_2 photocatalytic reactions and the TDI deposited on PMMA-coated glass slides. To further identify the origin of the fluorescence, the fluorescence spectra of single molecules were measured before and after UV irradiation at each fluorescent spot (Figure 14B, panel c). The spectrum after UV irradiation was found to be very intense and blue shifted by ~70 nm compared to the one before UV irradiation, strongly suggesting that TDI diepoxide was the source of fluorescence. Formation of singlet oxygen ${}^1\text{O}_2$ during the TiO_2 photocatalytic reactions was also very efficient, as 40% of the TDI molecules underwent complete digital switching.

Efficient production of singlet oxygen upon photoexcitation of TiO_2 particles was somewhat surprising, and three different reactions were proposed to mediate its formation: (i) recombination of superoxide anion $\text{O}_2^{\cdot-}$ with photogenerated holes,⁷⁴ (ii) dismutation of two superoxide anions in water solution producing partially excited oxygen molecules,⁷⁷ and (iii) electron–hole recombination resulting in energy transfer to molecular O_2 .⁷⁸ Illumination of nanoscale anatase particles (<10 nm), however, does not lead to formation of ${}^1\text{O}_2$, due to the insufficient charge separation in small-sized particles.⁷⁴

As noted above, the redox properties and difference in ROS reactivity are critical for biomedical applications of photocatalysis as they determine their longevity and range of their biological effects. Short-lived ROS species like OH^\bullet and ${}^1\text{O}_2$ participate readily in the reaction with neighboring molecules on a “first come, first served” basis.⁷⁹ Singlet oxygen ${}^1\text{O}_2$ is especially important in the reaction with unsaturated lipids in plasma membranes, resulting in compromised membrane functions often associated with cell necrosis. On the other hand, relatively long-lived species such as $\text{O}_2^{\cdot-}/\text{HO}_2^\bullet$ and H_2O_2 diffuse over long distances and can affect neighboring cells.⁸⁰ The effectiveness of oxidation of organic species by ROS and their complete decomposition to CO_2 and H_2O is visually shown in the AFM images obtained by illumination of stearic acid monolayer on TiO_2 surface (Figure 15). Stearic acid is a polyunsaturated lipid

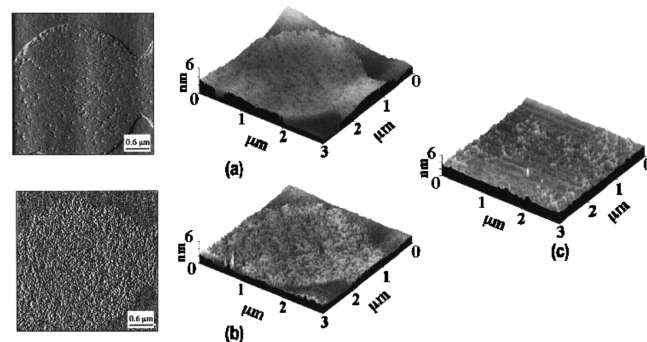


Figure 15. $\text{TiO}_2(110)$ -mediated photodegradation of stearic acid shown in the sequential AFM images ($3 \mu\text{m} \times 3 \mu\text{m}$). Images were obtained after (a) 5, (b) 10, and (c) 20 min of UV irradiation. (a and b) Images are also displayed in two dimensions (left) to highlight morphological changes (incident UV light intensity = 2.5 mW cm^{-2}). Reprinted with permission from ref 81. Copyright 1999 American Chemical Society.

and a component in the plasma membrane that can be used as a model system for studying the effects of the photogenerated radicals on cell membrane integrity. When a 2 nm layer of stearic acid adsorbed on TiO_2 nanocrystalline film was illuminated with UV light (2.5 mW/cm^2) changes in the surface morphology were readily observed. Initially, illumination caused inhomogeneous pitting of the film, while continued irradiation enlarged the affected areas and caused merging of the pits resulting in production of isolated islands that eventually completely disappeared.⁸¹ In the same manner as the radical species decompose stearic acid, one can imagine that reactive oxygen species will induce cytotoxicity to the neighboring tissue. Therefore, there is growing interest in developing modified TiO_2 nanoparticles for photodynamic therapy as an alternative and promising noninvasive treatment for cancer.⁸² The greatest problem for photodynamic use of TiO_2 , however, remains absorption of light in the UV part of the spectrum that constitutes only 5% of the white light spectrum.

9. BIOMEDICAL APPLICATIONS OF PRISTINE TiO_2 NANOPARTICLES

As we have shown in previous sections photoirradiated TiO_2 particles drive various chemical reactions due to their strong oxidation and reduction ability. This effect was first applied by Cai et al.⁸ in the immortal HeLa cell lines. For that purpose HeLa cells were illuminated with UV light for 10 min in the presence of TiO_2 (100 $\mu\text{g}/\text{mL}$), and after illumination distinct cell death was detected. The authors concluded that the cells were killed by hydroxyl (OH^\bullet) and hydroperoxyl (HO_2^\bullet) radicals produced from water upon illumination of TiO_2 particles and also that the cells were directly oxidized by the photogenerated holes in TiO_2 . It should be noted that these authors found that TiO_2 particles in the absence of light showed little cytotoxicity for concentration as high as 360 $\mu\text{g}/\text{mL}$. The distribution of TiO_2 particles in the HeLa cells was studied using a transmission electron microscope (Figure 16). It was found that TiO_2 particles were localized on the cell membrane and in the cytoplasm but not in the nuclear region.

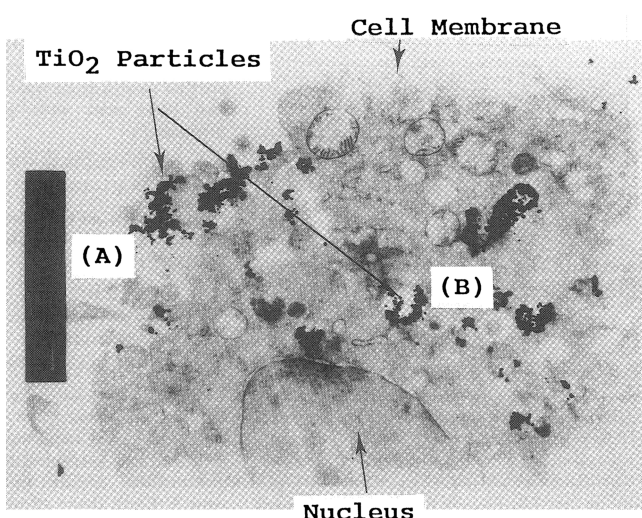


Figure 16. TEM picture of HeLa cells incubated with TiO_2 (0.1 mg/mL) for 24 h. TiO_2 aggregates were found on the membrane (A) and cytoplasm (B), while none of the particles were found in the nucleus. Reprinted with permission from ref 8. Copyright 1991 The Chemical Society of Japan.

Subsequent studies investigating the effect of TiO_2 in sunscreens on DNA confirmed the ability of TiO_2 to catalyze oxidative DNA damage in cultured human fibroblasts *in vitro*.⁸³ It has been also shown that incubation of the human skin fibroblasts with 10 $\mu\text{g}/\text{mL}$ of TiO_2 for 18 h with subsequent illumination with UVA light (0.58 KJ/m^2) showed photosensitivity that was light intensity dependent.⁸⁴ Illuminated fibroblasts contained significant levels of photooxidation, as measured by hydroxylation of guanine bases in RNA after irradiation. However, cellular DNA did not show significant levels of oxidative damage. These results support the view that TiO_2 photocatalyzes free radical formation within localized regions of a cell, namely, the membrane and cytoplasm and not the nucleus.

Later work showed that photoactivated TiO_2 , in particular anatase, caused DNA cleavage at the guanine residues in the presence of Cu(II) and at thymine residues after piperidine treatment, demonstrating reactivity of photoproduced radical

species with both guanine and thymine.⁸⁵ DNA damage was inhibited in the presence of superoxide dismutase (SOD), catalase, and bathocuproine, the molecule that acts as a chelating agent for Cu(I). These results revealed that DNA damage was mediated by superoxide, hydrogen peroxide, and Cu(I). Cu(I) was formed in the process of photocatalytic reduction of Cu(II) by superoxide radical, and addition of SOD removed superoxide radicals necessary for formation of Cu(I). SOD was found to inhibit DNA damage due to inhibition of the reduction of Cu(II) by superoxide. It should be noted that Cu(I) forms an equilibrium with the $\text{O}_2^\bullet/\text{O}_2$ redox species,⁸⁶ suggesting that the phototoxicity of Cu(I) may actually proceed via O_2^\bullet radical and that the role of Cu(I) is to extend the longevity of superoxide radical anion. Accordingly, the study showed that DNA damage occurs in the presence of a high concentration of anatase particles in the absence of Cu(II). DNA photodamage was also inhibited in the presence of typical free hydroxyl radical scavengers such as mannitol, ethanol, DMSO, and sodium formate, suggesting that OH^\bullet radicals were also involved in DNA damage under these conditions. It was concluded that the mechanism that involves superoxide-mediated DNA damage may be responsible for the phototoxicity of TiO_2 .

Although phototoxicity of nanosized TiO_2 was observed in concentrations as low as 10 $\mu\text{g}/\text{mL}$, a major challenge for the use of pristine TiO_2 in phototherapeutic applications remains in the ability of TiO_2 to absorb only the UV part of the light spectrum. Figure 17 shows the tissue cross section of absorption of light for the different ranges of the light spectrum.⁸⁷ The figure shows that in the UV region, where pristine TiO_2 absorbs, a significant part of the incoming light is also absorbed by proteins, melanin, and hemoglobin. On the other hand, water and fat tissue start absorbing at 1000 nm, leaving the optical window in the range of 600–1000 nm as the only feasible region where photoactive species can be efficiently activated for photodynamic therapy. In order to make TiO_2 nanoparticles amenable for practical applications, the nanoparticles must be modified to respond to the visible light in this optical window.

10. SENSITIZATION OF TiO_2 NANOPARTICLES FOR ABSORPTION OF VISIBLE LIGHT

10.1. Enediol and Catechol Sensitization of TiO_2 Nanoparticles

Different methods have been developed to extend the optical absorption of TiO_2 in the visible region. Interaction of TiO_2 nanoparticles with enediol molecules (including catechols and squaric or ascorbic acid containing compounds) was the first approach that held promise for extending the optical absorption to the visible region for biological/medical applications.^{24,69,88} Adsorption of these oxygen-rich ligands on the surface of TiO_2 nanoparticles was found to repair undercoordinated Ti surface atoms. Due to the ortho position of hydroxyl groups and sp^2 hybridization of carbon atoms in enediol ligands, surface Ti atoms become chelated in the optimal geometry of a five-membered ring, restoring the six-coordinated octahedral geometry of surface Ti atoms. This strong binding enabled seamless integration of enediol ligands with TiO_2 nanoparticles that results in formation of hybrid orbitals generated by mixing of the orbitals of chelating ligands and the continuum states of TiO_2 . Due to this hybrid character of modified nanoparticles absorption of light in these systems enabled excitation of electrons from the chelating enediol ligands directly into the

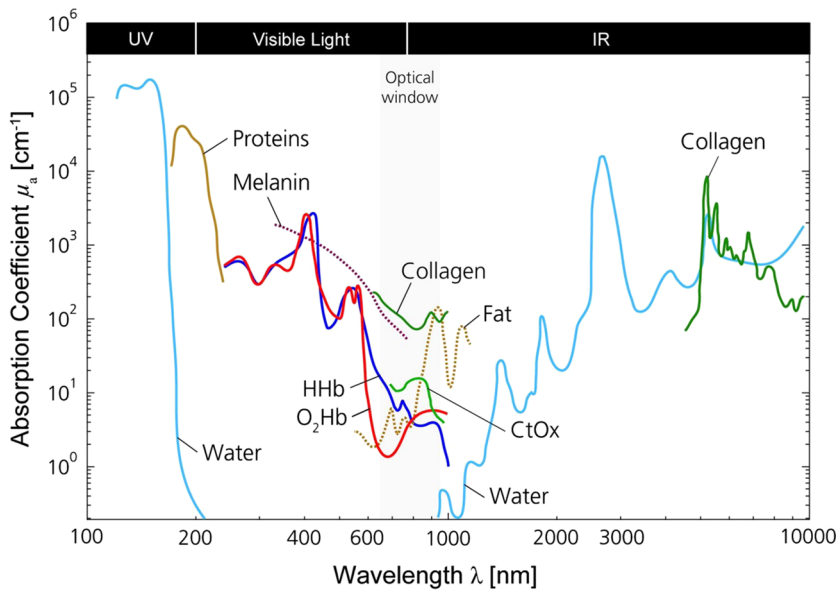


Figure 17. Absorption spectra for different chromophores present in human tissue. Shown are the spectra for millimolar concentration of oxy O_2Hb and deoxy-HHb hemoglobin, proteins, water, collagen, fat, and cytochrome oxidase (CtOx). Optical window through the tissue is in the region from 600 to 1000 nm. Reprinted with permission from ref 87. Copyright 2013 Elsevier.

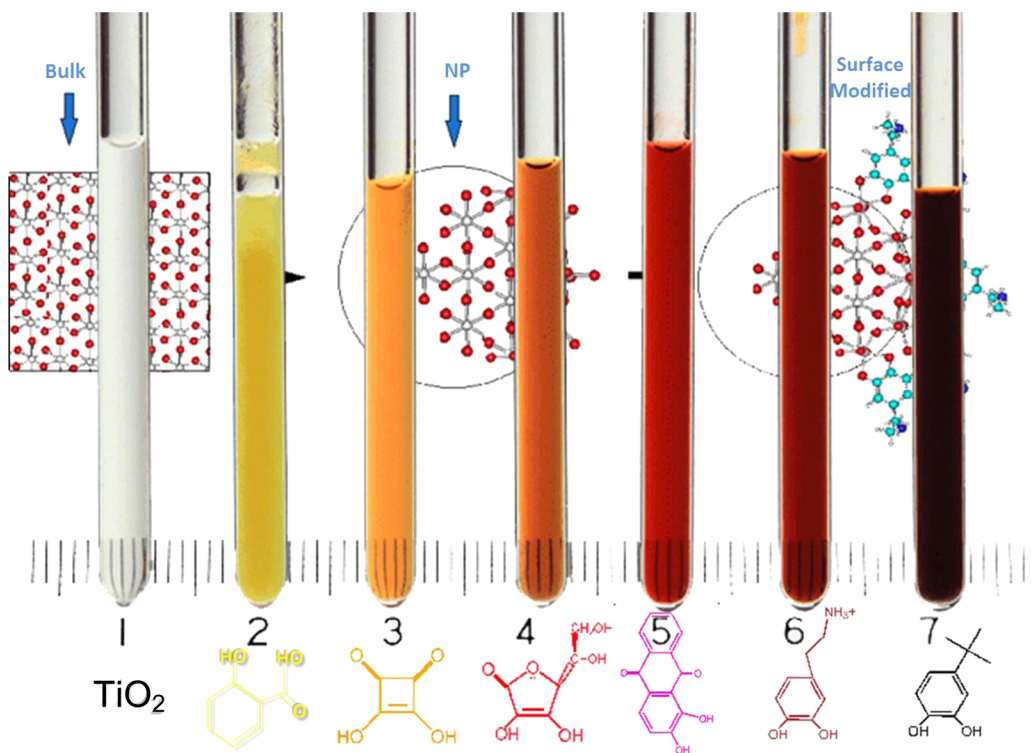


Figure 18. Forty-five Angstrom TiO_2 nanoparticles modified with different bidentate ligands: (1) bare TiO_2 , (2) salicylic acid, (3) squaric acid, (4) ascorbic acid, (5) alizarin, (6) dopamine, and (7) *tert*-butyl catechol. Molecule structures of the ligands used for surface modification are shown below the corresponding tube. The binding of enediol ligands is enhanced because of the stability gained from adsorption-induced restructuring of the NP surface. Reprinted with permission from ref 69. Copyright 2002 American Chemical Society.

conduction band of the TiO_2 particles, lowering their effective band gap.

The charge-transfer state of these collective orbitals enabled tuning of the effective band gap of surface-modified TiO_2 with the aromatic character of the ligand used for surface modification. Squaric acid-modified nanoparticles lower the effective band gap and the excitation threshold to 2.4 eV, ascorbic acid to 2.0 eV,

alizarin to 1.8 eV, dopamine to 1.4 eV, and *tert*-butyl catechol to 1.2 eV (Figure 18), tuning the absorption of hybrid nanoparticles throughout the whole visible-light region. The extinction coefficient of these particles was found to be directly proportional to the surface coverage. Importantly, in these composite systems localized orbitals of surface-attached ligands are electronically coupled with the delocalized conduction band of

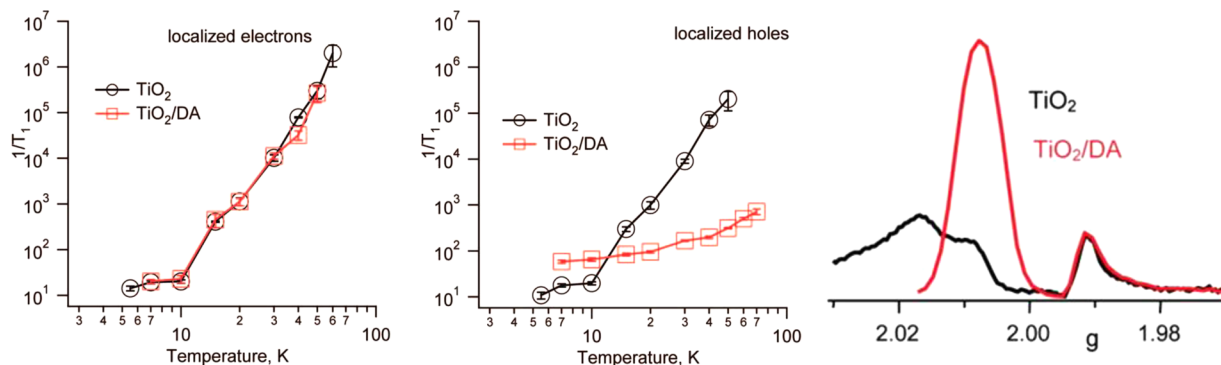


Figure 19. Spin–lattice relaxation dependence on the temperature for (a) electrons and (b) holes localized on dopamine in conjunction with (c) field swept echo spectra of TiO_2 and TiO_2/DA nanoparticles obtained by pulsed EPR. Reprinted with permission from ref 90. Copyright 2009 American Chemical Society.

the TiO_2 semiconductor, enabling electron hole pairs to be instantaneously separated into two phases upon absorption of light, increasing the separation distance between charge pairs: the holes localized on the donating organic modifier, and the electrons delocalized in the conduction band of TiO_2 .⁸⁹

While photogenerated electrons in dopamine-modified nanocrystals continue to show the same relaxation properties as electrons and holes in bare TiO_2 nanoparticles indicative of dynamic coupling to the anatase crystal field (see eq 12), the holes localized on dopamine show slow relaxation characteristic of carbon-centered organic radicals (Figure 19). Importantly, localized holes and electron spins in dopamine-modified nanoparticles behave as separate entities.⁹⁰ Relaxation of holes in dopamine (DA)-modified TiO_2 nanoparticles shows weak dependence on the temperature compared to photogenerated electrons, suggesting that relaxation from 4 to 20 K is dominated by resonant interactions with low-energy phonons, while at higher temperatures a weakly temperature-dependent Raman process with $1/T_1 \approx T^{1.5}$ was observed. The weak temperature dependence of relaxation is characteristic of relaxation of carbon-centered organic radicals.^{61,91} This further confirms instantaneous separation of electron hole pairs in these hybrid systems, resulting in effective charge separation as unpaired electrons on Ti atoms (trapped electrons) do not interact/couple with unpaired electrons of $\text{DA}^{+}\bullet$ radicals. This, in turn, suggests that reactions of photogenerated holes in dopamine-modified TiO_2 nanoparticles would not affect the reactivity of photogenerated electrons such as reduction of oxygen molecules to superoxide anions as well as other ROS. However, adsorption properties of TiO_2 nanoparticles could change upon surface modification with dopamine. The presence of dopamine at the surface of nanoparticles influences the affinity of oxygen molecules and superoxide radical toward nanoparticle surface, modifying overall efficiency of charge-transfer reactions. Therefore, the mechanism and yield of ROS formed in photocatalytic reactions in aerated aqueous solutions will change upon surface modification with dopamine due to the surface changes between bare and dopamine-modified TiO_2 , the difference in redox properties of localized holes, and the efficiency of charge separation.

Enediol ligands used for surface modification also provide points of attachment for covalent linking of biologically active molecules to the pendant groups of a surface-modifying ligand. Binding of biological molecules through covalent bonding enables robust composites that can be used for targeted delivery or *in vivo* applications.⁹² Due to their aromatic character, surface-modifying ligands were found to act as conductive leads that

allow covalent linking of the nanoparticles to biological molecules such as DNA,^{88,93–96} PNA,⁹⁵ peptides,^{97,98} antibodies,^{99,100} or magnetic resonance contrasting agents.¹⁰⁰

Modification of TiO_2 nanoparticles with enediol ligands results in enlarged spatial separation of photogenerated charges, holes localized on ligands, and electrons localized within the lattice of TiO_2 . This enhanced charge separation results in suppressed recombination of charges. This system also shows a signature of the efficient charge separation, the correlated radical pair, previously observed in natural photosynthetic systems and only in a few optimized triad donor–acceptor systems.^{42,89} While photogenerated electrons are only slightly affected by the presence of dopamine, localization of charges affects strongly the electronic properties and oxidation potential of photogenerated holes. Consequently, as the ROS are formed in multiple redox chemistries on the surface of particles, surface modification alters the mechanism of the radical species formed during illumination. Dimitrijevic et al.⁹⁰ demonstrated that dopamine radicals, $\text{DA}^{+}\bullet$, are not capable of oxidizing water molecules to OH^\bullet radicals on the surface of modified TiO_2 nanoparticles. The major ROS component produced upon illumination of TiO_2/DA was found to be superoxide anions formed in a reaction of photogenerated electrons with molecular oxygen, as demonstrated by a spin trap EPR experiments using TEMP superoxide reaction (Figure 20). Formation of singlet oxygen in this system was also detected and is probably the result of dismutation reaction of two $\text{O}_2^{-}\bullet/\text{HO}_2^\bullet$. The measured yield of ${}^1\text{O}_2$ was very low compared to bare TiO_2 . The low yield suggests that singlet oxygen is not formed in the reaction of the recombination of $\text{DA}^{+}\bullet$ with $\text{O}_2^{-}\bullet$, in contrast to bare TiO_2 where the major route for formation of ${}^1\text{O}_2$ is via reaction of photogenerated holes with superoxide anions, in contrast to bare TiO_2 , where the major route for formation of ${}^1\text{O}_2$ is via reaction of photogenerated holes with superoxide anions.

10.2. Dye Sensitization of TiO_2 Nanoparticles

Dyes such as chlorin e6¹⁰¹ and hypocrellin B¹⁰² were also used for visible-light-induced cell death. TiO_2 nanocrystalline particles were modified with a monolayer of chlorin e6 trisodium salt and incubated with murine thymic lymphoma (EL-4) cancer cells. Cells were irradiated with visible light (550–750 nm) used to excite chlorin e6. Irradiated nanoparticles induced significant damage to the EL-4 cells. A substantial fraction of cell death was contributed by dye conjugated to TiO_2 particle, compared to that of the chlorin e6 alone. This result suggests a cooperative interaction between surface-adsorbed dye and TiO_2 nanoparticles. Neither TiO_2 alone (1 mg/mL) under dark conditions nor under visible-light irradiation alone induced EL-4 cell death.

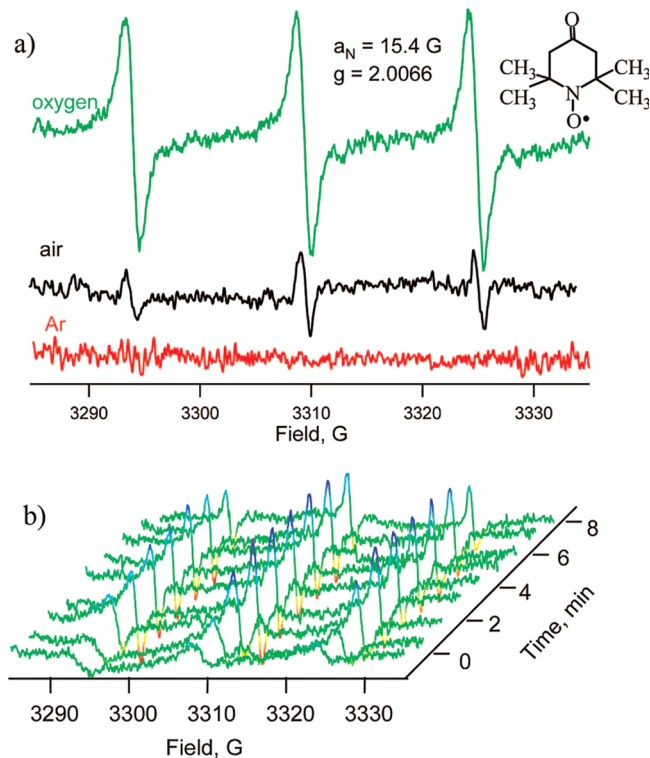


Figure 20. (a) Illumination of 0.1 M TiO_2/DA results in formation of radicals that react with 20 mM TEMP. (b) EPR spectra measured upon continuous UV-vis illumination in oxygenated solution at different times. Reprinted with permission from ref 90. Copyright 2009 American Chemical Society.

Weak bonding of the electrostatically adsorbed dye is the drawback of this system for biomedical applications as the complex is not likely to survive delivery of nanoparticles *in vivo* due to the interaction of reactive five-coordinated TiO_2 surface atoms with blood plasma proteins in the circulation. In addition, nonspecific interactions of nanoparticles with cells may lead to the death of not only cancerous cells but normal cells as well.

Phtalocyanine has also been used as a dye sensitizing agent.¹⁰³ Using the sol–gel method, zinc phthalocyanine (ZnPc) molecules were integrated into the porous network of titanium dioxide (TiO_2). $\text{ZnPc}-\text{TiO}_2$ was tested with three cell lines: epithelial cells, human hepatocellular liver carcinoma cells, and human fibroblasts (Figure 21). The composite $\text{ZnPc}-\text{TiO}_2$ was active against tumor and nontumor mammalian cells, while bare TiO_2 was not found to be phototoxic. Cells internalized $\text{ZnPc}-\text{TiO}_2$ at a lower level than ZnPc alone, probably due to the size of the composite and/or its hydrophilic character. The particle size of the composite, however, was not reported. Internalized $\text{ZnPc}-\text{TiO}_2$ and ZnPc were localized to mitochondria and cytoplasm. This approach of integrating the dye into the porous titanium dioxide network has the advantage that minimal losses of dye are expected upon interaction of $\text{ZnPc}-\text{TiO}_2$ with plasma proteins and lipids during nanoparticle delivery. Due to nonspecific interactions of dyes incorporated into porous TiO_2 nanoparticles these composites may be toxic to both non-transformed as well as transformed cells.

10.3. Sensitization by Anionic and Cationic Doping

Another approach to broaden the absorption range of TiO_2 to the visible region of the light spectrum involves doping of TiO_2 nanoparticles. For example, nitrogen-doped TiO_2 ($\text{N}-\text{TiO}_2$)

nanoparticles showed enhanced absorbance in the region up to 600 nm compared to bare TiO_2 .¹⁰⁴ The cytotoxicity and phototoxicity induced by visible light of TiO_2 and $\text{N}-\text{TiO}_2$ were examined for three types of human cancer cell lines: hepatocellular carcinoma cells, cervical carcinoma cells (HeLa), and nasopharyngeal carcinoma cells. There was not substantial cytotoxicity observed in the dark for nanoparticle concentrations up to 200 $\mu\text{g}/\text{mL}$. In contrast, visible-light-induced photolysis induced cytotoxicity was readily detected. As the concentration of nanoparticles incubated with the various cancer cell lines increased, the survival fraction of the cells decreased. $\text{N}-\text{TiO}_2$ was more effective than bare TiO_2 at causing cancer cells death. Laser scanning confocal microscopy detected colocalization of $\text{N}-\text{TiO}_2$ nanoparticles within Golgi apparatus of cancer cells. Some of the TiO_2 was also internalized in the nucleus as confirmed by colocalization experiments using confocal microscopy. Moreover, micronuclei, a type of deviant nuclear morphology, were visible after the cells were treated with $\text{N}-\text{TiO}_2$ nanoparticles that were irradiated by visible light. These findings provide evidence that the nucleus was directly damaged by photoexcitation of $\text{N}-\text{TiO}_2$ nanoparticles (Figure 22). ROS were found to play a central role in the photolysis of all three cell lines.

Another study in HeLa cells showed that $\text{N}-\text{TiO}_2$ altered intracellular Ca^{2+} , mitochondrial membrane potential (MMP), and nitrogen monoxide (NO) levels after treatment with PDT.¹⁰⁵ The $\text{N}-\text{TiO}_2$ particles caused more significant increases in Ca^{2+} and NO levels and decreases in MMP in HeLa cells compared to bare TiO_2 (Figure 23). Changes in cell morphology were also shown using confocal microscopy. $\text{N}-\text{TiO}_2$ -treated cells exhibited morphological distortions and breakage in the membrane an hour after illumination. Interestingly, the authors found that considerably more OH^\bullet radicals were photoproduced by TiO_2 than by $\text{N}-\text{TiO}_2$ under visible light. As cell death efficiency was significantly greater using visible illumination of doped TiO_2 , the study strongly suggests that hydroxyl radicals might contribute less to the damage of HeLa cells in photolysis using $\text{N}-\text{TiO}_2$ compared to other ROS ($\text{O}_2^\bullet-$ and H_2O_2) that have longer lifetime and longer diffusion length.⁹⁰

Illumination of Fe-doped and, in particular, Fe–N-codoped TiO_2 nanoparticles with visible light also significantly enhanced cell death.^{106–108} Photocatalytic inactivation of leukemia tumors by Fe–N-doped TiO_2 was assessed using the Cell Counting Kit-8 (CCK-8) assay. Doped TiO_2 nanoparticles significantly inhibited leukemic HL60 cell growth. The photocatalytic activity of codoped Fe–N– TiO_2 was greater than that of the combination of Fe– TiO_2 and $\text{N}-\text{TiO}_2$, suggesting that the photocatalytic efficiency could be effectively improved by the codoping of TiO_2 with paired Fe–N dopants. Additionally, when 200 $\mu\text{g}/\text{mL}$ of 2 wt % Fe–N– TiO_2 nanocomposites was incubated with the cells and illuminated for 30 min, an inactivation percentage of 78.5% was reached. Additionally, the authors detected a buildup of Ca^{2+} while illuminating the cells incubated with Fe–N– TiO_2 nanoparticles. The authors attributed Ca^{2+} increases with caspase activation leading to apoptosis. The authors suggested that Ca^{2+} accumulation in the cytoplasm activates a series of events leading to apoptosis.^{109,110} The percentage of apoptotic cells illuminated in the presence of Fe–N– TiO_2 nanoparticles was 7.3 times larger than in the control cells (Figure 24). They also suggested that photoinduced ROS increased intercellular Ca^{2+} levels. Photogenerated electrons in this system were found to localize at the Fe^{3+} centers, while photogenerated holes localize on nitrogen

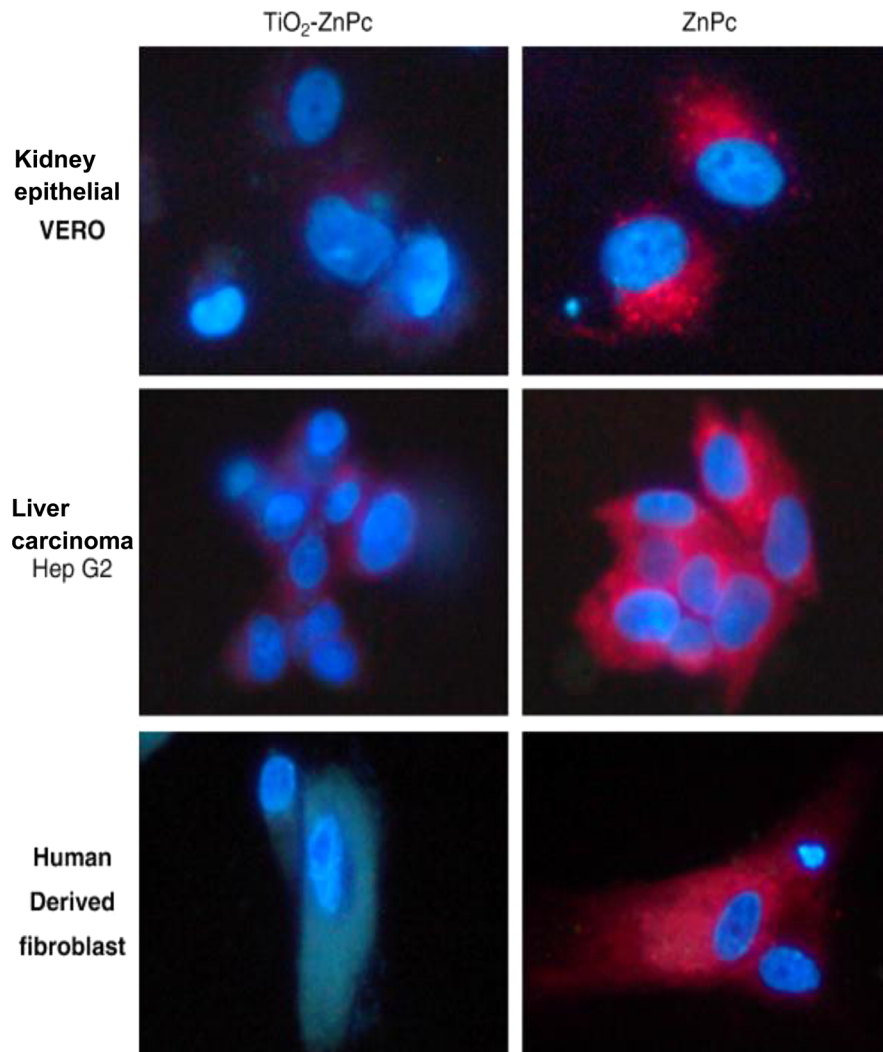


Figure 21. Cellular internalization of TiO₂-ZnPc and ZnPc in Vero, Hep G2 cells, and human-derived fibroblasts (HDFs). After 24 h of incubation with 15 μ M ZnPc or 100 μ g/mL of TiO₂-ZnPc, live cells were stained with Hoechst 3342 to identify the nucleus. Compounds were observed in the cytoplasm but not in the nucleus. The fluorescence signal of TiO₂-ZnPc was not observed in HDFs. Reprinted with permission from ref 103. Copyright 2009 American Chemical Society.

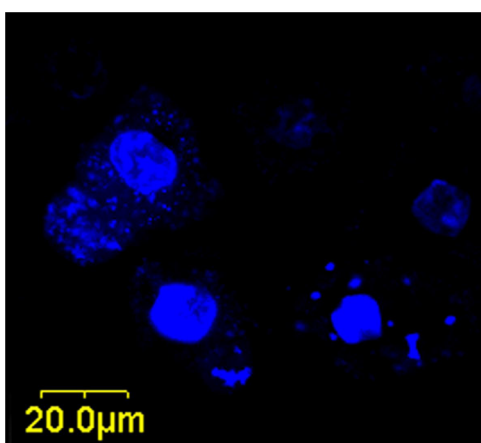


Figure 22. Micrograph of HeLa cells cultured with 50 μ g/mL N-TiO₂ for 10 h and illuminated using a Xe lamp with a 400 nm long-pass filter for 4 h to show the micronuclei. Reprinted with permission from ref 104. Copyright 2011 Li et al.; licensee Springer.

codopants. Both of these states have lower reduction and oxidation properties than CB and VB of bare TiO₂, respectively; hence, they have a significantly lower driving force to reduce the adsorbed oxygen and oxidize water. Nevertheless, the photocatalytic efficiency of cell death in this system was still higher than both bare TiO₂ and Fe-doped TiO₂. The authors attribute this behavior to the trapping of colocalized electron hole pairs that presumably inhibits charge pair recombination. What is of particular interest in this system is that initiation of cell death occurred by the absorption of the low-energy photons ($h\nu_4$, Figure 24) in the visible part of the light spectrum. Yet both photoinduced electrons and holes possessed sufficient energy to produce ROS necessary for cell death.

10.4. Surface Modification with Inorganic Complexes

A new class of assemblies that contains all inorganic components and are stable and nontoxic in the dark but stable and toxic under illumination provides a novel strategy for developing photosensitizers. This approach could overcome existing problems by extending the absorption of photocatalysts to the visible range of the light spectrum. Current approaches of dye sensitization involve compounds of limited stability and photostability,

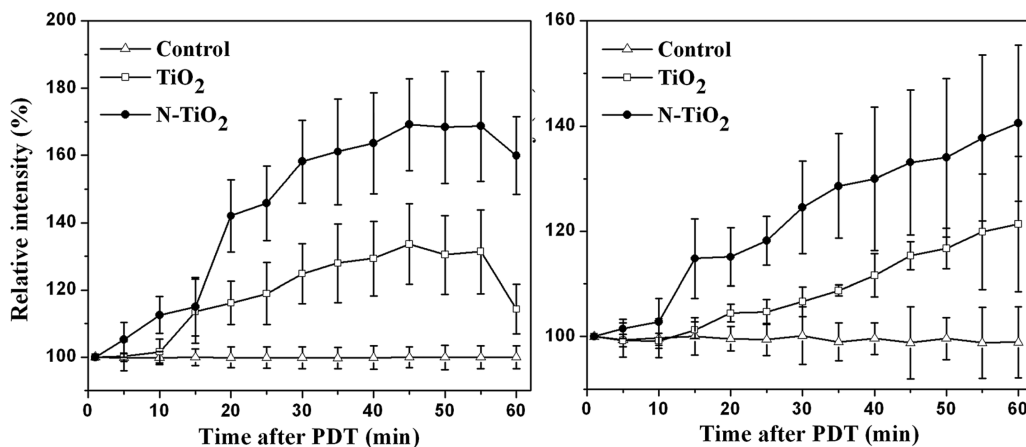


Figure 23. Changes of the intracellular Ca^{2+} levels (a) and NO levels (b) with time after illumination. TiO_2 (□) and N- TiO_2 (■) treated cells ($100 \mu\text{g}/\text{mL}$) were incubated in the dark for 2 h and illuminated by visible light for 5 min. Fluorescence of control cells (Δ) was set as 100%. Adapted from ref 105. Copyright 2013 Li et al.; Licensee Springer.

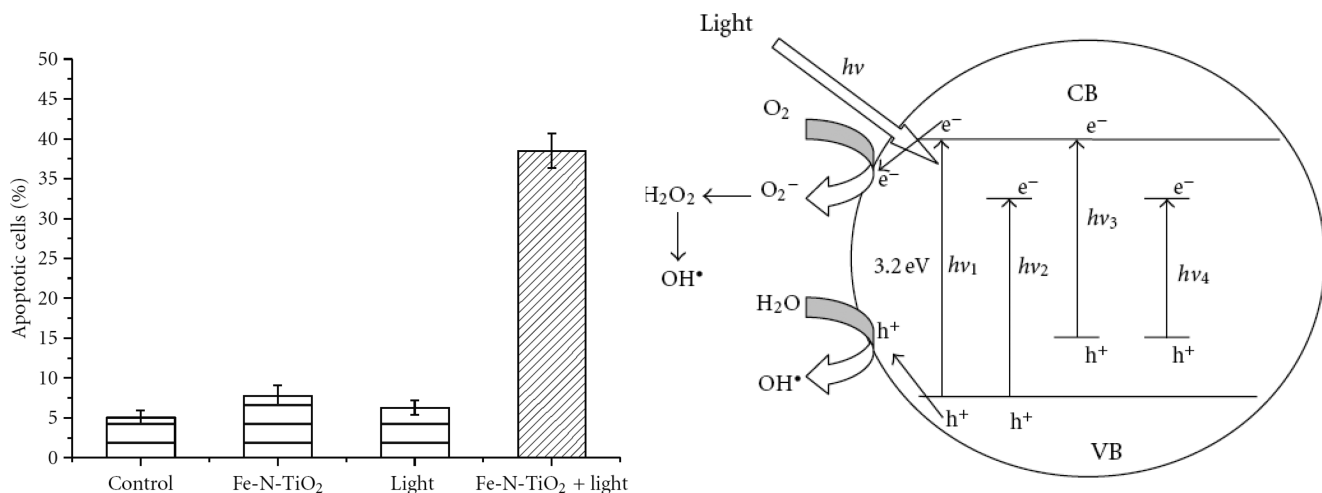


Figure 24. Light therapy in the presence of Fe-N-TiO₂ (30 min, light intensity of $5.0 \text{ mW}/\text{cm}^2$) resulting in a variance of percentage of apoptotic cells (left). Schematic presentation of the band structure of Fe-N-TiO₂ is shown on the right (TiO_2 , $h\nu_1$; Fe-TiO₂, $h\nu_2$; N-TiO₂, $h\nu_3$; Fe-N-TiO₂, $h\nu_4$). Adapted from ref 107. Copyright 2012 Kangqiang Huang et al.

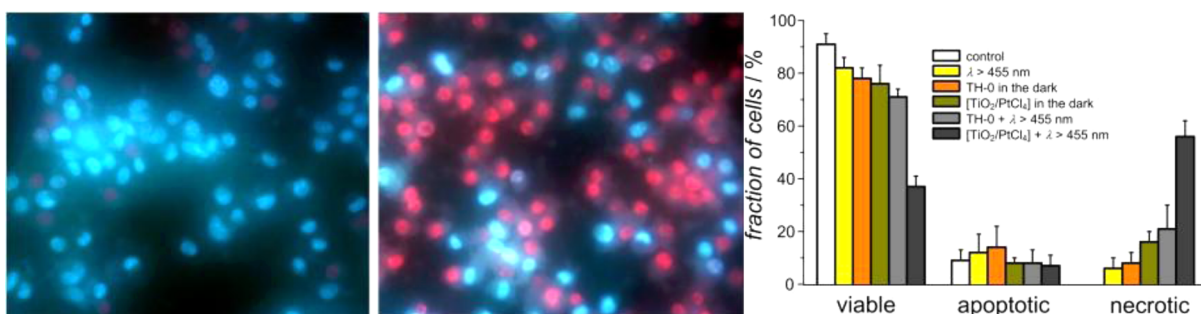


Figure 25. Melanoma cells from a mouse stained with Hoechst 33342 and propidium iodide: control (left) and cells irradiated with visible light ($\lambda > 455 \text{ nm}$, 30 min) in the presence of 4% $[\text{TiO}_2/\text{PtCl}_4]$ ($500 \mu\text{g}/\text{cm}^3$) (middle) in conjunction with the distribution among viable, apoptotic, and necrotic cells (right). Adapted from ref 111. Copyright 2008 Elsevier.

insufficient light absorption, or low yields of ROS generation. A recent study exploits the photoactivity of $[\text{TiO}_2]-\text{O}-\text{PtCl}_4(\text{H}_2\text{O})$, a photocatalyst known to be exceedingly reactive in visible-light photooxidation.¹¹¹ The phototoxicity of PtCl₄-modified titanium dioxide illuminated by visible light was investigated in mouse melanoma cells. The results demonstrate that $[\text{TiO}_2/\text{PtCl}_4]$ was more phototoxic to the melanoma cells as

compared to unmodified TiO₂ or the platinum(IV) species alone. Two fluorescent dyes Hoechst 33342 and propidium iodide were used to determine melanoma cells viability (Figure 25). In this assay the condensed chromatin of apoptotic cells is stained brighter by Hoechst 33342 than the chromatin of nonapoptotic cells, and only dead cells are stained by red-fluorescent propidium iodide dye.¹¹² Live cells have intact

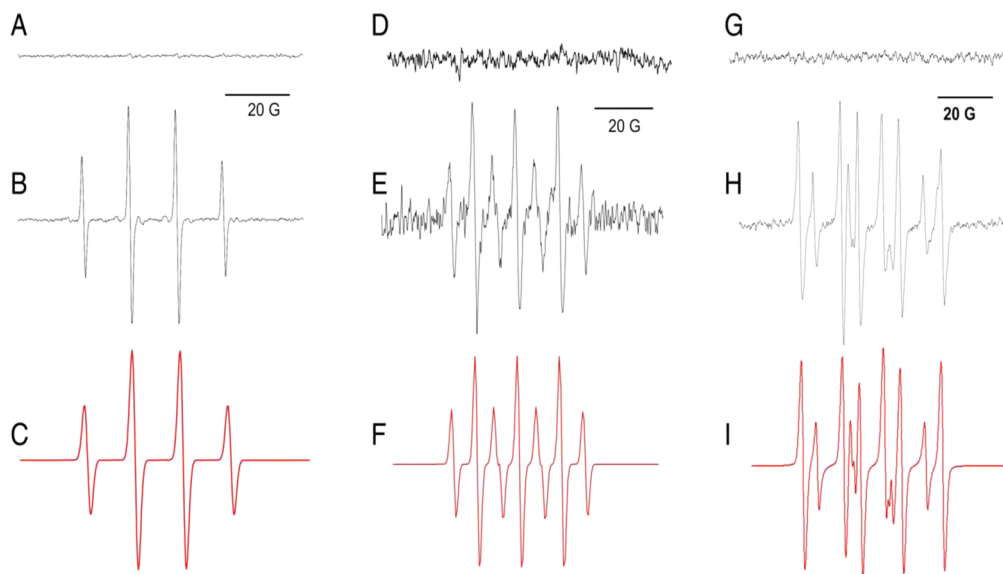


Figure 26. EPR spectra of UV–vis ($\lambda > 320$ nm) or visible light ($\lambda > 455$ nm) photoactivated TiO_2 or $[\text{TiO}_2/\text{PtCl}_4]$ in the presence of DMPO. TiO_2 in the dark (A); $\text{TiO}_2 + \text{UV-vis}$ (B); simulated spectrum of $\text{DMPO}-\cdot\text{OH}$ (C); $[\text{TiO}_2/\text{PtCl}_4]$ in the dark (D, G); $[\text{TiO}_2/\text{PtCl}_4] + \text{vis}$ (E); simulated spectrum of DMPOX (as a result of the DMPO oxidation by $\cdot\text{ClO}_2$ radical) (F); $[\text{TiO}_2/\text{PtCl}_4] + \text{UV-vis}$ (H); superposition of simulated spectra of $\text{DMPO}-\cdot\text{OOH}$ and $\text{DMPO}-\cdot\text{CH}_3$ (I). Reprinted with permission from ref 111. Copyright 2008 Elsevier.

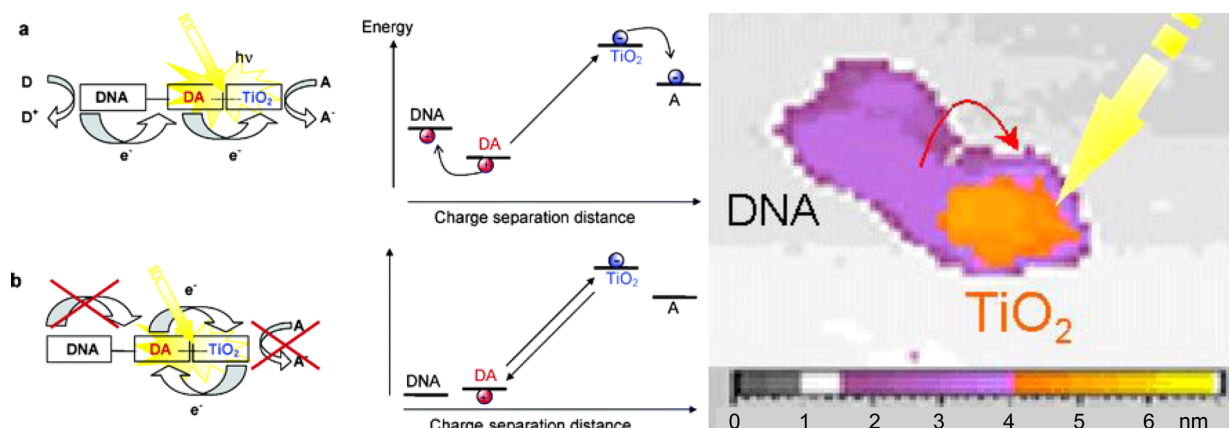


Figure 27. Electron transfer in hybrid bioinorganic triad systems is the basis for investigations of DNA redox reactions that are coupled to the initial photoinduced charge separation in TiO_2 /dopamine (left). AFM image of 5 nm TiO_2 nanoparticle linked with 16 base pair long oligonucleotide through dopamine anchor (right). Color-coded bar at the bottom of the image represents the sample height. Adapted from ref 93. Copyright 2004 American Chemical Society.

membranes that exclude a variety of dyes such as propidium iodide; however, the dye can easily penetrate the damaged, permeable membranes of nonviable cells, and it can be used to determine cells compromised by photocatalytic action. It was determined that the surviving fraction of the cells was reduced to 59% 4 h after irradiation of S-91 cells in the presence of $[\text{TiO}_2/\text{PtCl}_4]$ (500 mg/mL, $\lambda > 455$ nm, 30 min). Among the dead cells, 89% were determined to be necrotic cells showing propidium iodide stains and only 11% to be non-necrotic apoptotic cells. It was concluded that necrosis causes cellular death when the cells are irradiated in the presence of $[\text{TiO}_2/\text{PtCl}_4]$. Necrosis occurred within 4 h of treatment. EPR spin-trapping experiments using DMPO probe indicate photogeneration of various ROS including hydroxyl radicals and superoxide radical anions formed under light with wavelengths > 320 nm (Figure 26). However, chlorine-derived reactive species ($\cdot\text{ClO}_2$, $\cdot\text{ClO}$) were the main components in all experiments using visible light. The authors concluded that partial photodecomposition of the platinum(IV)

surface complex under visible light was the mechanism of formation of chlorine-derived radical species that were in all probability responsible for the necrotic cell death.

11. BINDING SPECIFICITY OF DNA HYBRID NANOCOMPOSITES

DNA stores genetic instructions for living organisms and is often thought of as a blueprint for a cell development and functioning. However, mutations in DNA can occur due to unrepaired damage, errors in the process of replication, or insertion or deletion of DNA fragments.^{113,114} The simplest types of mutations are single base pairs changes in DNA that results in replacement of normal amino acid with an incorrect amino acid in the encoded protein, which can cause changes in protein function. Some mutations introduce a premature stop codon that leads to an unstable or a malfunctional protein. Another example of a DNA change is the deletion or insertion of one or more base pairs that can shift the reading frame. From that point onward, all

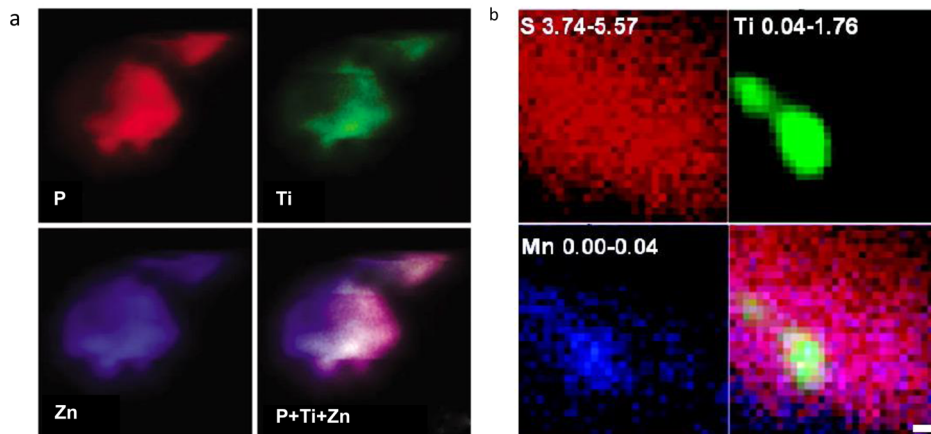


Figure 28. (a) Elemental mapping of a single nucleus containing 3.6×10^6 nanoparticles linked to oligonucleotide with genomic sequence. Colocalization of phosphorus (red), titanium (green), and zinc (blue) signals are presented as the overlap of these three colors. (b) Scan of the PC12 cell segment incubated with mitochondrial oligonucleotide/TiO₂ composites. Colocalization of sulfur (red), titanium (green), and manganese (blue) is presented as the overlap. Adapted from refs 88 and 93. Copyright 2003 and 2006 Rights Managed by Nature Publishing Group and American Chemical Society, respectively.

amino acids are incorrectly coded. Even more complex DNA changes can occur resulting in severely mutated proteins, while beyond current molecular bioengineering capabilities a future theoretical solution might be to use redox active nanoparticles to detect or repair such mutations that cause cell malfunctioning.

As shown in the previous sections, the reactivity of TiO₂ nanoparticles is contingent on the properties of the molecules that are conjugated to their surface. As mentioned previously, surface modification with enediol ligands results in visible absorption of TiO₂ particles, but it also reduces the reactivity of TiO₂ photogenerated holes to produce less reactive but longer lived radicals. Additionally, covalent binding of enediol ligands also provides a point of covalent attachment for biological molecules. The pendent groups of enediol ligands can be easily reacted with reactive residues of biological molecules, improving their reactivity with photogenerated holes. For example, if dopamine is used as a surface modifier, two ortho hydroxyl groups of dopamine chelate surface Ti atoms and positively charged amino groups that terminate TiO₂/DA surface can be used for covalent binding to carboxyl group-terminated biological molecules such as DNA oligonucleotides.⁹³

Absorption of light in TiO₂–dopamine–DNA oligonucleotide nanoconjugates results in charge separation across the nanoparticle–ligand interface. This initial charge separation is followed by further charge separation in which a hole, localized on a surface ligand, is transferred to DNA providing that conjugated DNA has a proper oxidation potential. The progression of events in the charge separation sequence of events in hybrid bioinorganic nanoconjugates was analogous to the reaction pathway in supramolecular triads, in which the efficiency of charge separation and redox functions were dependent on the thermodynamic properties of the triad constituents (Figure 27). Importantly, charge separation in DNA nanoconjugates was found to be dependent on the redox properties of the oligonucleotides covalently linked to the surface modifier. The redox properties of the DNA oligonucleotides that contain mismatches differ significantly from those of fully hybridized DNA. Hence, a new class of *in vitro* and *in vivo* hybridization sensors based on the efficiency of charge separation in TiO₂–DNA nanocomposites can be envisioned.

11.1. TiO₂/DNA Conjugates in the Cell Machinery

TiO₂/oligonucleotide nanocomposites were able to enter cells and preserve biorecognition of the cellular DNA in cell cultures, despite the short length of oligonucleotides.⁸⁸ In situ studies also confirmed that TiO₂ nanoparticles linked to 16-mer oligonucleotides were able to hybridize a long DNA (10 kilobase) fragment having a complementary DNA sequence. TiO₂/oligonucleotide nanoconjugates with the sequence complementary to the segments of genomic DNA were able to be introduced into PC12 mammalian cells using transfection and, moreover, reach the cell nucleus. The X-ray fluorescence elemental mapping scan of an isolated nucleus from a PC12 cell incubated with TiO₂/oligonucleotide is presented in Figure 28a. The scan shows that the titanium signal coincided with the phosphorus and zinc areas and that the Ti signal had a strong intensity in a small subregion of the nucleus. This nuclear subregion closely resembled the cell nucleolus in its size and shape. The nucleolus is the location where TiO₂–oligonucleotide nanoconjugate with genomic sequence would most likely be retained, as rRNA is concentrated in the nucleolus organizing regions.

When the sequence of oligonucleotide was changed to match that of mitochondrial DNA, specific for NADH dehydrogenase,⁹⁶ TiO₂/oligonucleotide nanocomposites were not identified in the nucleus region using X-ray elemental mapping. Instead, they were distributed within the whole cell and the Ti signal colocalized with manganese signal (Figure 28b), which was restricted to mitochondrial regions. Mn is bound to mitochondrial manganese superoxide dismutase protein, a nuclear encoded primary antioxidant enzyme located exclusively in the mitochondrial matrix that catalyzes the dismutation of superoxide (O_2^-). The intensity of Mn signal in X-ray elemental map images is proportional to Mn concentrations in the mitochondrial matrix.

TiO₂ nanoparticles can generate strong oxidizing radicals in the presence of light that are able to attack many neighboring molecules. Additional control of its redox properties is possible, however, when the TiO₂ surface is modified with enediol ligands as this alters the oxidizing power of photogenerated carriers (see section 10). Moreover, TiO₂ nanoparticles linked to DNA oligonucleotides gain site selectivity in a oligonucleotide-sequence-specific manner, directing the ROS to only the specific,

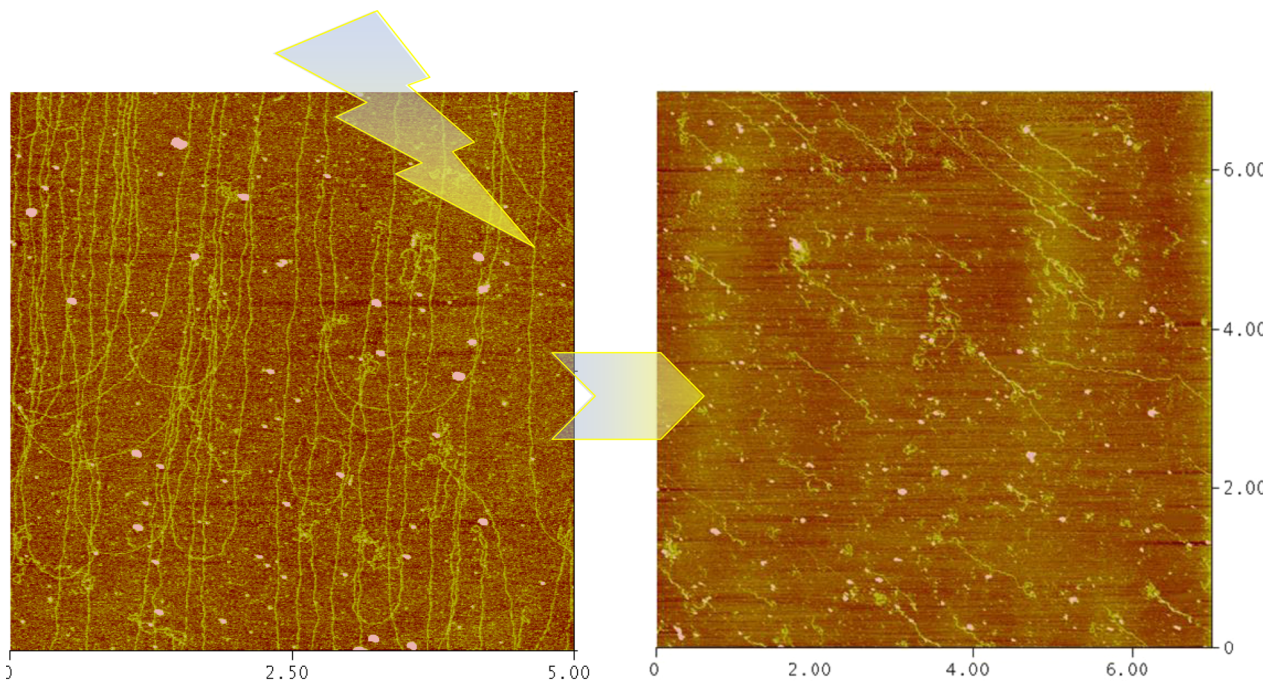


Figure 29. TiO_2 cleaves λ phage DNA upon illumination with white light ($>400 \text{ nm}$). Before illumination λ DNA is decorated with TiO_2 nanoparticles (left). After illumination λ DNA is cleaved into fragments of $\sim 1 \mu\text{m}$ length with some of the fragments ending with nanoparticles (right). The sequence of PNA used for attaching TiO_2 nanoparticles to DNA is found in λ DNA genome at eight positions for antiparallel binding. Adapted from ref 95. Copyright 2006 Society of Photo Optical Instrumentation Engineers.

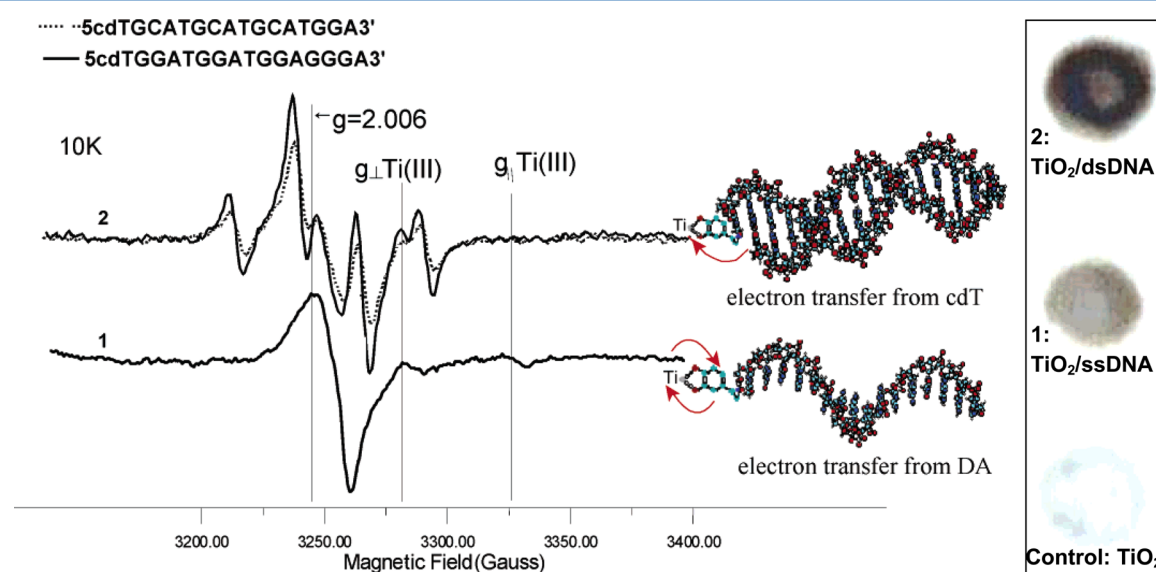


Figure 30. Low-temperature EPR spectra (left) and photoreduction of silver ions under ambient conditions (right) of TiO_2 nanoparticles coupled to single-stranded (1) and double-stranded oligonucleotides (2). Samples were illuminated with white light for 5 min. Brown color indicates a metallic silver deposition following accumulation of photogenerated electrons on TiO_2 nanoparticles as a result of extended charge separation. Adapted from ref 93. Copyright 2004 American Chemical Society.

complementary DNA base segment. When activated by light, photogenerated holes in a nanoconjugate are transferred only to the selected base pairs of the DNA sequence that are easily oxidized and which are located in the vicinity of the DNA antisense hybridized to nanoconjugates. As a consequence, light energy absorbed by TiO_2 is channeled to the bonds within the hybridized DNA, employing the oxidizing power of photo-generated holes to oxidize specific nucleic bases and leave the rest of the DNA intact. These nanocomposites now have the novel ability to act as light-inducible nucleic acid endonucleases.

Localization of the oxidation was shown by illumination of TiO_2 nanoparticles linked to double-stranded 30-mer and 50-mer oligonucleotides that lead to the light- and time-dependent release of free oligonucleotide. The length of the nucleotide cleaved upon illumination was consistent with the length of the antisense DNA linked to the nanoparticle. Furthermore, the amount of double-stranded oligonucleotide that was cleaved increased with the illumination time.⁸⁸ Since these nanocomposites can be targeted to the cell nucleus, one can envision

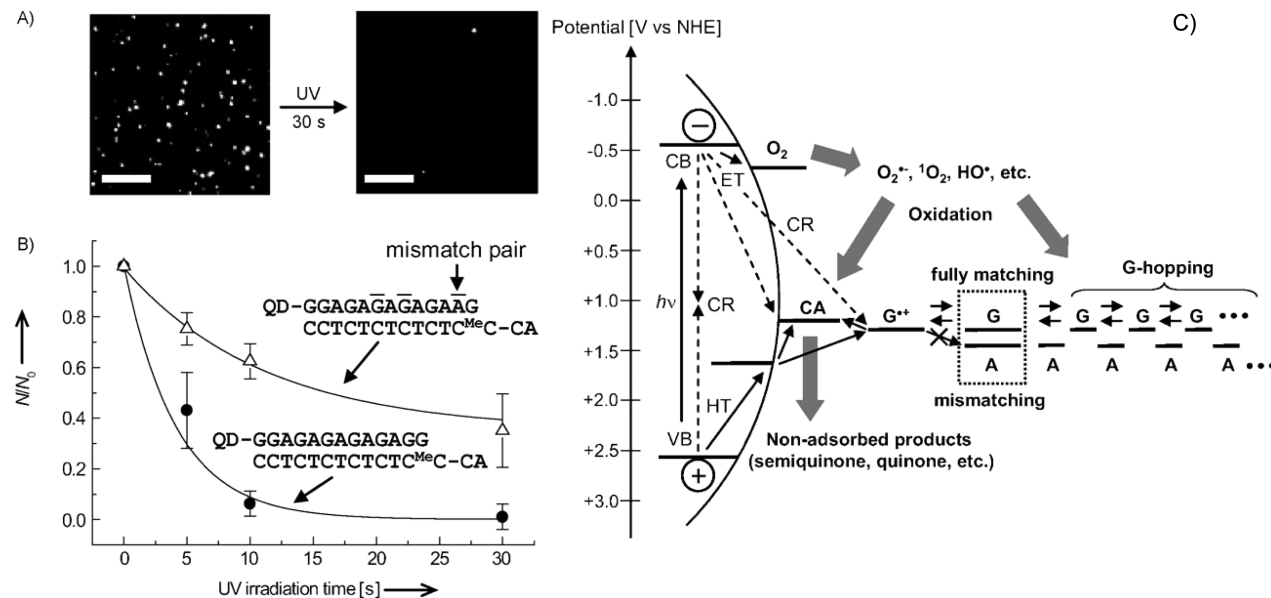


Figure 31. (A) Fluorescence of TiO₂/DNA linked to QDs obtained before (left) and after (right) the UV irradiation. Due to the cleavage of DNA upon UV illumination, QDs were detached causing a decrease in luminescence. (B) Luminescence of the fully matched and mismatched DNA duplexes dependent on UV irradiation. N_0 and N denote the number of luminescent spots before and after UV irradiation, respectively. (C) Proposed mechanisms of charge separation in the TiO₂/DNA nanoconjugates. Adapted from ref 120. Copyright 2008 Wiley-VCH Verlag GmbH & Co. KGaA, Weinheim.

that these composites might be used as endonucleases during gene surgery *in vitro* and *in vivo*.

Further improvement of this approach was achieved when peptide nucleic acid (PNA) rather than DNA oligonucleotides was linked to TiO₂ nanoparticles using dopamine as an anchor.⁹⁵ PNA is an oligonucleotide analog that has a peptide backbone instead of charged phosphate groups found in the backbone of DNA.^{115,116} Due to the absence of electrostatic repulsion of negative charges that modulate binding in DNA, PNA binding to the complementary strands is stronger than a DNA/DNA interaction. As a consequence, only 6 base pair long PNA bound to a DNA strand has a melting temperature above room temperature and can compete with the binding of double-stranded DNA. In this way, seven nucleotide long PNA, with a sequence complementary to the designed segments of λ phage DNA, was anchored to TiO₂ and used to decorate phage DNA with 5 nm TiO₂ nanoparticles (Figure 29a). Binding of PNA nanoconjugates was not exclusive to λ phage. PNA nanoconjugates were also shown to invade coiled plasmid DNA in a sequence-specific manner.¹¹⁷ Illumination of λ phage TiO₂ composites caused cleavage of λ DNA that resulted in DNA fragments with lengths that corresponded to the distance between the λ DNA runs complementary to the PNA sequence (Figure 29b).⁹⁵ After light-induced cleavage, TiO₂ nanoparticles remained bound to the ends of cleaved fragments, which likely included guanine doublets in DNA/PNA duplex.

11.2. TiO₂/DNA Conjugates and Biosensing

Absorption of light in TiO₂/oligonucleotide nanocomposites leads to extended charge separation in which photogenerated holes are transferred to double-stranded DNA with proper oxidation potential but not to single-stranded DNA⁹³ (Figure 30). Illumination of single-stranded DNA/TiO₂ composites (ssDNA/TiO₂) at helium temperatures results in a charge separation between dopamine and TiO₂ nanoparticle, as demonstrated using EPR spectroscopy. The EPR spectrum was identical to the one observed upon illumination of dopamine-

modified TiO₂, indicating that charge separation at 10 K terminates at the dopamine site and never reaches ssDNA oligonucleotide. In contrast, the EPR spectrum of double-stranded DNA conjugate (dsDNA/TiO₂) shows a signal characteristic of oxidized DNA. This spectrum was successfully simulated with the hole localized on the cdT nucleobase used for conjugation to dopamine. Upon annealing the sample to liquid nitrogen temperatures, the hole transfer extended further, enlarging the charge separation distance between the holes and the electrons trapped in the TiO₂ nanoparticles. The EPR spectrum at liquid nitrogen temperatures reveals localization of the holes on guanine bases of DNA. A follow-up study showed that hole transport in TiO₂/DNA conjugates is dependent on the position of guanine sites in DNA sequence, exponentially decaying with the distance from the nanoparticle surface.⁹⁴ Photocurrent measurements as well as metallic silver deposition confirm hole transfer consistent with the observed low-temperature measurements of charge separation in the TiO₂/DNA systems.

Importantly, this study also shows that DNA mismatches can be detected using charge separation in TiO₂ nanoparticles. During DNA sensing, DNA mismatches occur when template (probe) DNA is bound to target DNA with an altered base pair. Detection of single-nucleotide mismatches is important as many diseases including cancers and even drug resistance are associated with the appearance of single-nucleotide polymorphisms (SNPs).^{118,119} When the target DNA originates from a DNA with SNP, hybridization with the probe DNA (no SNP) results in a mismatch. One or two mismatches (GT) in the sequence of dsDNA reduces the hole transfer from TiO₂ linkers to DNA and reduces the consequent deposition of silver by photogenerated electrons for 50% or 80%, respectively. The result was explained by the decrease in the electron density in GT mismatches that prevents hole hopping within dsDNA. This study shows that TiO₂/DNA conjugates could be used for electronic biosensing with exceptional sensitivity, even detecting

the presence of the single-nucleotide mismatch. This exceptional sensitivity is attributed to the sensitivity of hole migration through DNA nucleobases.

Hole migration in TiO_2/DNA composites was also studied using wide field fluorescence microscopy.¹²⁰ In this study QD end-labeled DNA oligonucleotides were hybridized with a complementary strand having catechol as a terminal unit that enabled DNA immobilization on TiO_2 nanocrystalline films. Photocatalytic cleavage of the TiO_2/DNA nanoconjugates induced by UV irradiation was investigated using wide-field fluorescence microscopy. The investigators observed a decrease of the luminescence at the single-molecule level that was sequence dependent and significantly attenuated in DNA containing mismatches (Figure 31). These results strongly suggest that the migration of holes through DNA plays an important role in the photocatalytic cleavage of the conjugates. The authors have also shown that ROS, namely, OH^\bullet , $\text{O}_2^{\bullet-}$, and ${}^1\text{O}_2$, play a significant role in DNA cleavage.

12. BINDING SPECIFICITY OF PROTEIN HYBRID NANOCOMPOSITES

Binding of a protein or peptide to TiO_2 can enable specific localization and targeting of the hybrid TiO_2 –protein conjugate to a specific cell protein or organelle. Of special interest is the binding of monoclonal antibodies or markers to TiO_2 semiconducting nanoparticles. The reason is that once the conjugated TiO_2 -targeting-protein binds to the target on the cell surface or within the cell matrix, the semiconductor can initiate a series of redox reactions and alter cell functioning. In the same manner as an antisense oligonucleotide bound to TiO_2 is able to find target complementary DNA and after light-induced activation nick or cleave target DNA, peptide or proteins can be used for binding TiO_2 to complementary protein structures on intact cells or organelles with multivalent binding specificity and that subsequent light activation can be used to induce redox reactions to alter cell metabolism or induce cell death.

12.1. TiO_2 /Antibody Interaction with Cell Machinery

Antibodies have been used successfully as therapeutic agents in treating cancer by targeting specific cells. Antibodies (Ab) combined with photocatalytic nanoparticles, such as TiO_2 , can form future platforms for targeted therapy. In order to test the possibility of photocatalysis for use in targeted therapeutics, TiO_2 –Ab conjugates were synthesized and tested for the targeted therapy of psoriasis.⁹² T cells were targeted as they play a critical role in the pathogenesis of psoriasis.⁹²¹ T cells are part of the immune system, and their function is to detect and fight off foreign organisms, such as viruses or bacteria. In psoriasis, however, the T cells attack healthy skin cells.^{122,123} New strategies focusing on modifying T cells in this disease through inhibition of T-cell activation, direct elimination of activated T cells, or inhibition of cytokine secretion or activity are being developed for treatment of psoriasis.¹²¹ In the following study the strategy for treatment was to link TiO_2 nanoparticles to T-cell-specific antibodies and initiate light-induced redox chemistry.¹²⁴ The conjugates were allowed to bind T cells and then activated with either visible or UV light. The research followed a three-tiered approach. The potential therapeutic approach would be the nanoparticle conjugate that targets specific markers on the T cell, and then photoactivation would result in the death of T cells while not damaging healthy epidermal cells and Langerhans cells.

First, TiO_2 was conjugated to the targeting antibody using the approach developed for linking the amino group terminus PNA. Once it was shown that the antibody could be attached to TiO_2 (Figure 32) the functionality of each component was tested. For

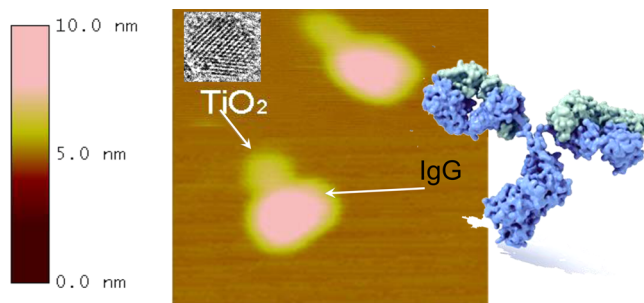


Figure 32. Atomic force microscopy image of TiO_2 –CD4 nanocomposites. TiO_2 –CD4 nanocomposites were dissolved in a HEPES buffer and incubated on freshly cleaved mica.

this purpose four monoclonal murine antibodies (Ab) were conjugated to TiO_2 . Three of these (anti-CD4, anti-CD8, and anti-CD3) are specific to T-cell epitopes. A fourth monoclonal antibody MOPS was also investigated as an isotype-matched negative control antibody to test the ability of nanoconjugate to retain the biological activity of the antibody.

Second, the Ab was tested for the ability to bind the target after conjugation to TiO_2 nanoparticles. Each cell type was incubated with either purified antibodies (anti-CD3, anti-CD4, anti-CD8, or MOPS) or TiO_2 –Ab conjugates (Figure 33). The results show that the anti-CD4 antibody and TiO_2 –anti-CD4 conjugates bound the cell lines that express CD4 and CD3, but they did not bind the cell lines that were negative for CD4. Similarly, both anti-CD8 and TiO_2 –anti-CD8 conjugates bound the CD8+ lines but not the CD8– cell lines. Although all three cell lines are reported to express CD3, the FACS results show definite binding of both anti-CD3 and TiO_2 –anti-CD3 only for the cells expressing CD8 and CD3. It should be noted that the negative control antibody MOPS and the negative control conjugate TiO_2 –MOPS did not bind any cells.

These results have clearly demonstrated the ability to target TiO_2 to the cell using molecular recognition properties of Ab. The third important question that remains to be answered is whether TiO_2 targeted to the cell of interest is still able to induce cell death after photoactivation. To investigate this outcome, each cell type was incubated with targeting TiO_2 –Ab conjugate and after photoactivation cell death was investigated using Trypan blue exclusion. The hypothesis was that TiO_2 –Ab nanocomposites after photoexcitation would produce targeted cell death. This targeted cell death may occur due to either protein damage at the binding via oxidation with photogenerated holes or initiation of programmed cell death by introduction of superoxide radical or singlet oxygen species produced via reaction with photogenerated electrons.⁹⁰

The results show surprising speed and specificity of cell death with TiO_2 –Ab conjugates. For the CD4+ cell line targeted with TiO_2 –anti-CD4, following the 1 min photoactivation, 25% of the cells showed cell death within 2 h and an additional 30% died 24 h after illumination (see Figure 34). Importantly, neither the control Ab, MOPs conjugated to TiO_2 , nor nonspecific Ab-conjugates like TiO_2 –CD8 incubated with CD4 cells caused significant cell death. The ability to specifically kill targeted cells was not limited to TiO_2 –anti-CD4 on CD4 cell line because

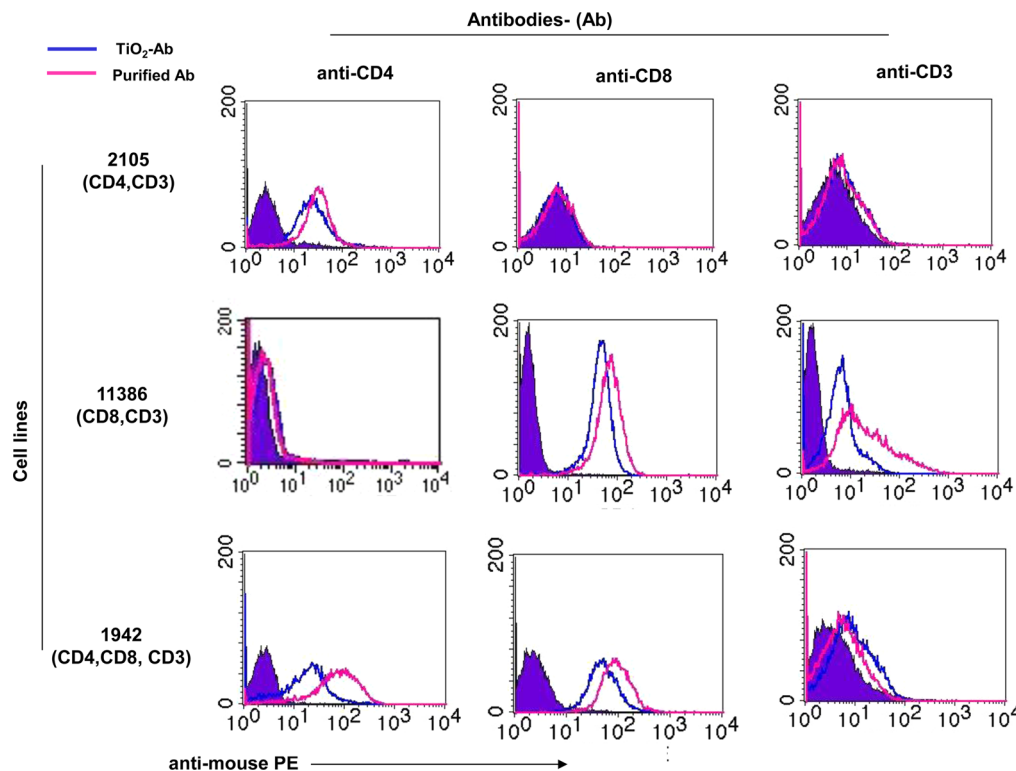


Figure 33. Antibodies retain targeting ability while linked to TiO_2 . CD4, CD8, and CD3 are epitopes that mark and are expressed on the surface of T cells. Three different cell lines 1942 (CD4, CD8, and CD3), 2105 (CD4 and CD3), and 11386 (CD8 and CD3) were used to test the ability of either purified antibody or TiO_2 -linked antibody to target them. Cells were labeled with 5 $\mu\text{g}/\text{mL}$ anti-CD4, anti-CD8, or anti-CD3 antibodies and then detected by fluorescently labeled antimouse Ab. Antibodies conjugated to TiO_2 were used at the same concentration of purified Ab and detected by the same secondary fluorescently labeled antibody. Each cell line was also stained with secondary ab alone as the unlabeled group in solid blue. Flow cytometric analysis was used to examine the data, and results are displayed in histogram form with fluorescence on the x axis. Cell lines are indicated on the left and the antibody treatment across the top. Purified antibodies are indicated by purple lines, and the TiO_2 -conjugated Ab are blue lines.

TiO_2 -anti-CD4 was also able to target and cause cell death in CD4+ cell lines (positive for CD4, CD8, and CD3) but not those lacking CD4 epitope (CD4-, such as CD8, CD3 cell line). Conjugating TiO_2 with other antibodies also generated functionally active targeting. TiO_2 -anti-CD8 or TiO_2 -anti-CD3 was also able to target CD-8 or CD-3 expressing cells to specifically induce cell death. Furthermore, we demonstrated that the surviving T cells do not up-regulate pro-inflammatory cytokines (IL-2, IFN- γ , and TNF- α) in response to TiO_2 -Ab treatment. These results indicate that cell death using TiO_2 composites was not associated with cellular inflammation.

This work demonstrated the power of constructing nanoparticle conjugates which combine unique inorganic and biological components. TiO_2 nanoparticles can be modified to capture a significant part of the light spectrum and generate reactive chemical species. The ROS in turn can destroy the inflammatory cells associated with psoriasis. The study also shows that nanoconjugates can be successfully constructed using several different monoclonal antibodies. Further, different linking chemistries were used for conjugation with retention of electron-transfer capability. These demonstrate the broad applicability of this technology and the possibility of optimizing the linkage for maximal performance, for example, by reducing the steric hindrance of the binding site or promoting charge transfer through the organic portion of the nanoconjugate. In each of the FACS experiments showing positive binding to cells there was slightly lower binding of nanoconjugates compared to unconjugated antibody. This is likely due to some degree of steric hindrance induced by the TiO_2 component to either the binding

to the cellular epitope and/or the binding of the secondary detection antibody. Overall, however, binding of TiO_2 -Ab and Ab alone was comparable, demonstrating that conjugation to the nanoparticles generally left the binding ability of the mAbs intact.

The effect of nanoconjugates on living cells was notable for its effectiveness, controlled activation, and specificity. In a clinical setting, this kind of control is of great value due to the potential of limiting side effects while increasing targeted killing effectiveness that derives their redox potential. However, the biological mechanism by which this electron transfer results in cell death is incompletely understood. Death was detectable soon after treatment and persisted up to 24 h after illumination with substantial total cell death. While the objective of this study was creation of an effective treatment for psoriasis, this strategy can be modified and applied to other disease states. In fact, we view a primary advantage of this technology is its flexibility. Various conjugates can be created using this strategy that can be tailored for different specificities and classes of targeting molecules. Also, as there are often multiple cell types that contribute to a disease state, multiple targets can be combined. While steric hindrance might limit creation of multivalent molecular entities, nanoconjugate “cocktails” included in a single treatment could be used to target multiple disease-associated epitopes.

Rozhkova et al.⁹⁹ targeted highly malignant glioblastoma multiform (GBM) cells using TiO_2 and monoclonal antibodies approach. The interleukin-13 (IL13), a key signaling molecule in cancerous growth and inflammation, binds interleukin-13R2 receptor domain (IL13 α 2R), resulting in internalization of the ligand–receptor complex inside the tumor cell.^{125–130} It has

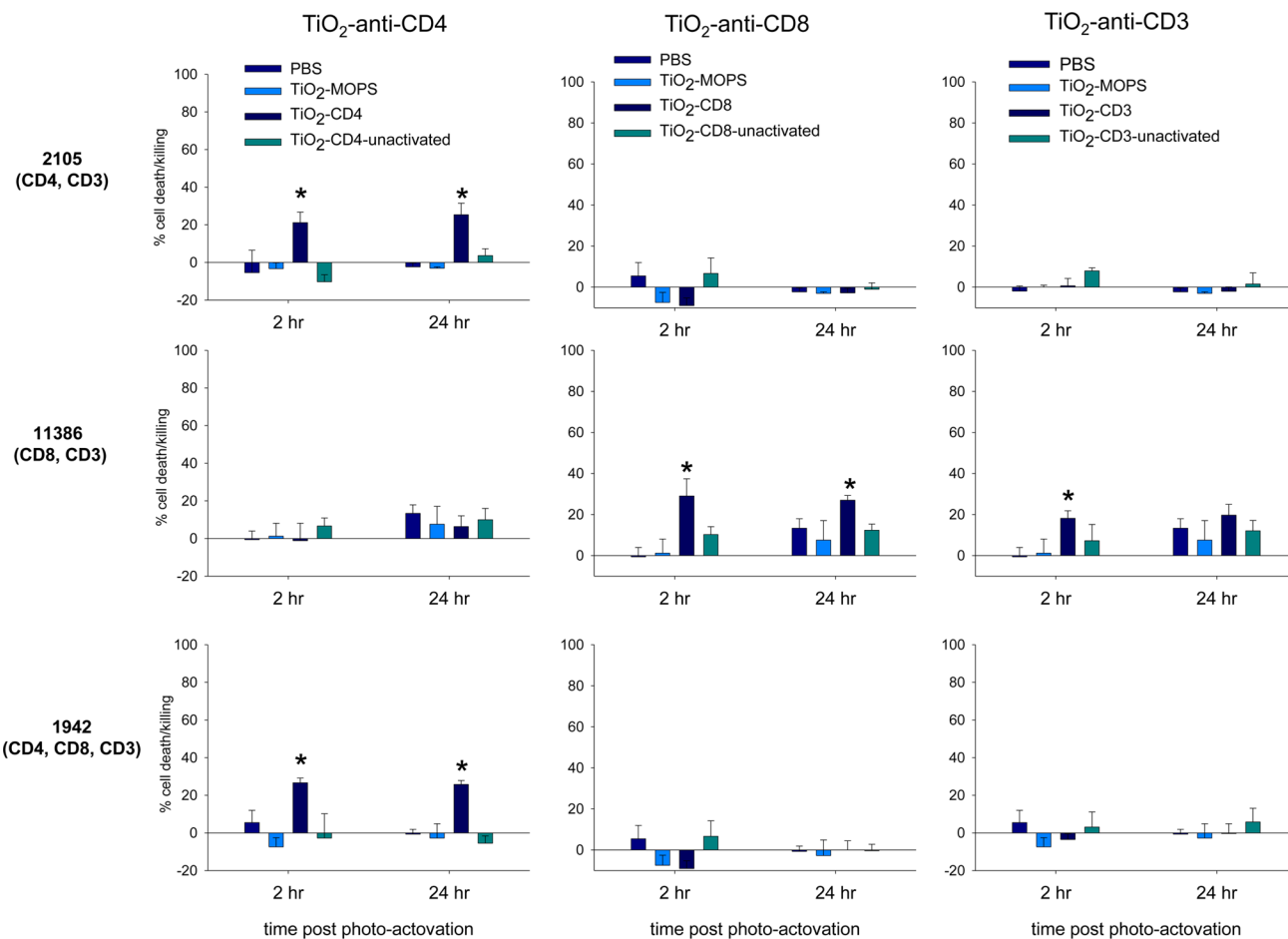


Figure 34. Functionalized TiO₂ can target and lyse T cells specifically. TiO₂ conjugated to anti-CD4, anti-CD8, anti-CD3, or control Ab (MOPs) were incubated with 3 different T cell lines as indicated and photoactivated for 1 min. After either 2 or 24 h an aliquot of cells was enumerated and examined for cell death by Typan blue exclusion. A control plate with similar treatments of each line was included that was not photoactivated (labeled as unactivated TiO₂–Ab). Results are displayed in terms of percent of cell death on the y axis at each time point. Cell lines are labeled on the left, and the TiO₂ conjugates are labeled across the top. Percent death at 24 h was calculated based on an average of PBS-treated cells as the baseline. (Asterisk designates significant $p < 0.05$ with respect to PBS-treated cells and TiO₂–MOPs-treated cells.)

been reported that this receptor is exclusively overexpressed on the cell surface of certain tumor types, including GBM.^{128,131} Therefore, IL13 α 2R appears to be an ideal target for antiglioblastoma therapy. This receptor was previously targeted with cytotoxic elements such as toxins,¹²⁵ viruses,¹³² immuno-nanoshells,¹³³ and more recently redox nanoparticles such as TiO₂.

In this study anti-IL13 was linked to TiO₂ through a carboxyl group-terminated catechol moiety (DOPAC) that enabled covalent linking of nanoparticles to the antibody as well as visible light excitation of the composite. Anti-IL13 conjugated to TiO₂ directed the nanoconjugate to the GBM cell. Elemental mapping using X-ray fluorescence (Figure 35a) shows that TiO₂ nanoparticles were not internalized in GBM A172 cells that highly express IL13 α 2R receptor but localized on the cell surface. The distribution of TiO₂ coincides with the distribution of phosphorus present in the cell membrane (composed of phospholipid bilayer) and throughout the cell but does not coincide with the distribution of Zn that is mostly associated with nucleoplasm proteins. When even very small concentrations of anti-IL13 bionanoconjugates were used to treat GBM cells, local concentrations of the titanium were detected that were comparable to concentrations of biogenic elements such as Zn.

Illumination of the glioblastoma cells incubated with the TiO₂/anti-IL13 (6 to 600 ng/mL) using polychromatic visible light (5 min) resulted in significant light-induced cytotoxicity in both U87 with moderate expression of IL13R2R receptor and A172 cells with high expression of IL13R2R receptor. Furthermore, 48 h following exposure to light, toxicity was still apparent (Figure 35b). Note that in these receptor-mediated experiments the concentration of TiO₂ was 50–5000 times lower than the concentration used with bare TiO₂. Illumination times in these experiments were also 6–10 times shorter than the treatment times used with bare TiO₂. The TiO₂–Ab conjugate exhibited concentration-dependent phototoxicity toward A172 cells. Within 6 h of light exposure A172 cells killing was 80%, whereas killing of lower receptor expressing U87 cells plateaued around 50% and did not change significantly with increasing nanoconjugate concentration for the same amount of time. Light treatment of the astrocyte cell line under the same experimental conditions did not induce any phototoxicity.

This study also determined for the first time the mechanism of cell death *in situ* as cell death was inhibited by 10 unit/mL superoxide dismutase (SOD; superoxide natural scavenger) or 2 mM sodium azide (superoxide, singlet oxygen, and OH[•] trap) (Figure 35c). This result indicates that under illumination with light in the visible range the photoinduced cytotoxicity of TiO₂

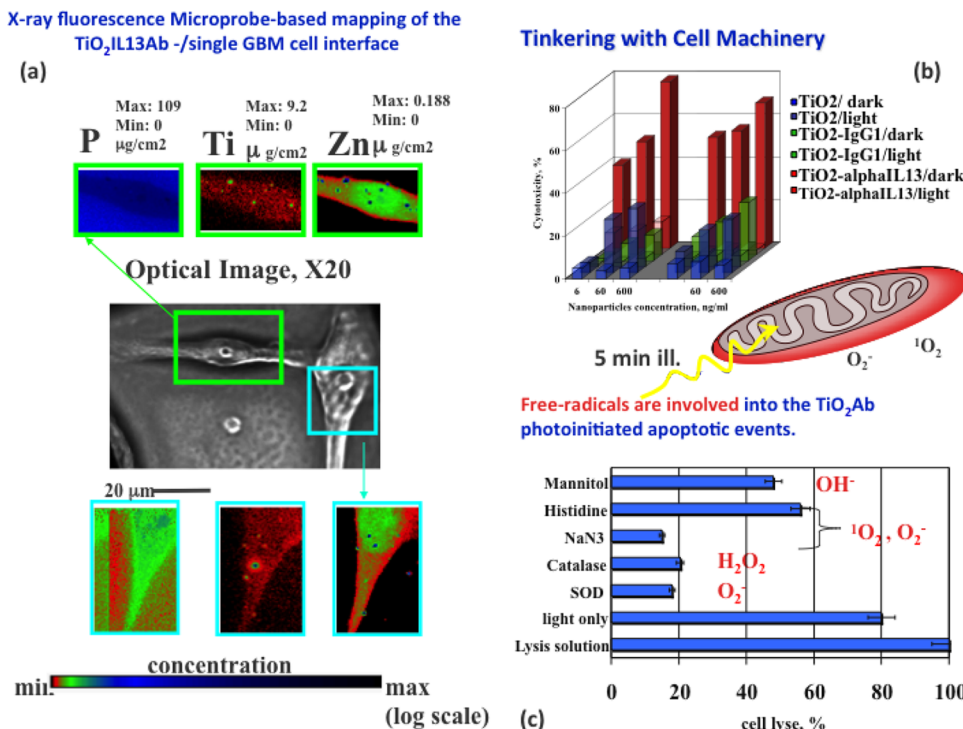


Figure 35. (a) TiO_2 -antibody/receptor interaction and mapping of the location and distribution of IL13R in a single A172 brain cancer cell using X-ray fluorescence microscopy. (b) Light-induced cytotoxicity in the presence of bare TiO_2 , TiO_2 modified with nonspecific antibody (TiO_2/IgG), and TiO_2 modified with anti-IL13 α 2R ($\text{TiO}_2/\text{alphaIL13}$) in the dark and after 5 min of illumination using visible light. (c) Quenching of light-induced cytotoxicity by $\text{TiO}_2/\text{alphaIL13}$ in the presence of different ROS radical scavengers. Adapted from ref 99. Copyright 2009 American Chemical Society.

tethered to mAb through a DOPAC linker is mediated by superoxide radical anions and to a lesser extent with singlet oxygen. It has been shown that superoxide triggers cancer cells to undergo apoptosis,¹³⁴ while photosensitized damage of plasma membranes of live cells is induced by singlet oxygen.¹³⁵ The fact that phototoxicity of TiO_2 tethered to mAb is mainly mediated by superoxide radicals suggests that apoptosis is the main mechanism of cell death. This conclusion is further supported by localization of annexin V on the surface of the membrane of the A172 GB cells after treatment with TiO_2 -mAb and following light exposure (Figure 36). Apoptotic changes caused by interaction of superoxide radicals with cell mitochondria are characterized by the loss of integral phospholipid mitochondrial membrane asymmetry and inversion of the normally cytosol-facing lipid phosphatidylserine to the outer side of the membrane with apoptosis. This inversion is one of the earliest events in apoptosis and detected by binding of annexin V to the inverted outer side of the membrane. Labeling of annexin V with fluorescent labels was detected using laser-confocal microscopy imaging. The signature of annexin binding was not observed in control experiments.

Xu et al.¹³⁶ also investigated light-induced cancer cell death using antibody-coated TiO_2 nanoparticles. By electroporating TiO_2 nanoparticles impregnated with the monoclonal antibody, the authors improved the photolysis selectivity and effectiveness of photoexcitation of TiO_2 delivered to cancer cells. The monoclonal antibodies appeared to improve the photokilling discrimination of TiO_2 nanoparticles toward the cancer cells, while electroporation accelerated delivery of the TiO_2 nanoparticles to cancer cells. In this study light-induced treatment was applied to the colon adenocarcinoma cell line (LoVo), and anticarcino embryonic antigen (CEA) antibody was used to target TiO_2 nanoparticles. TiO_2 nanoparticles were incubated

with CEA antibody for 5 days at 4 °C resulting in strongly physisorbed antibody which could not be separated from TiO_2 nanoparticles by centrifugation (10 000 r/min for 30 min). Electroporation was used to enhance the delivery speed of the CEA-modified TiO_2 nanoparticles to cancer cells. With this approach 100% of human LoVo colon cancer cells were killed within 90 min, while only 39% of the noncancerous cells were killed under irradiation of ultraviolet (UV) light (365 nm).

In another TiO_2 application for cancer treatment the investigators targeted cancer stem cells, another even more challenging problem. The importance of stem cells in the biology of metastasis is increasingly recognized.¹³⁷ Targeting metastatic stem cells with new strategies that would kill such cells would be a significant breakthrough. Elvira et al.¹³⁸ developed monoclonal antibodies (Nilo1) in their laboratory that recognize a cell surface antigen specific to neural stem cells.¹³⁹ They coupled TiO_2 to Nilo1 mAb using physisorption followed by centrifugation, as developed by Xu et al.¹³⁶ Conjugated particles were incubated with cancerous stem cells to assess whether the antibody could increase the retention of the nanoparticles on designated targets and if the conjugates could be used to selectively kill the target cells upon TiO_2 photoactivation (Figure 37).

Although light-induced cell death was incomplete, the study verified that Nilo1- TiO_2 complex can induce cell death in vitro. Importantly, the conjugate was particularly efficient when low concentrations of Nilo1- TiO_2 complex were used, whereas bare TiO_2 did not have significant killing power. TUNEL assays that detect DNA fragmentation also suggest that the major mechanism of light-induced cytotoxicity is program cell death, an apoptotic mechanisms. Rozhkova¹⁴⁰ has also shown the apoptotic mechanism of light-induced cell death by monoclonal IL13R antibody- TiO_2 composites using confocal microscopy. In this study it has been shown that highly crystalline TiO_2

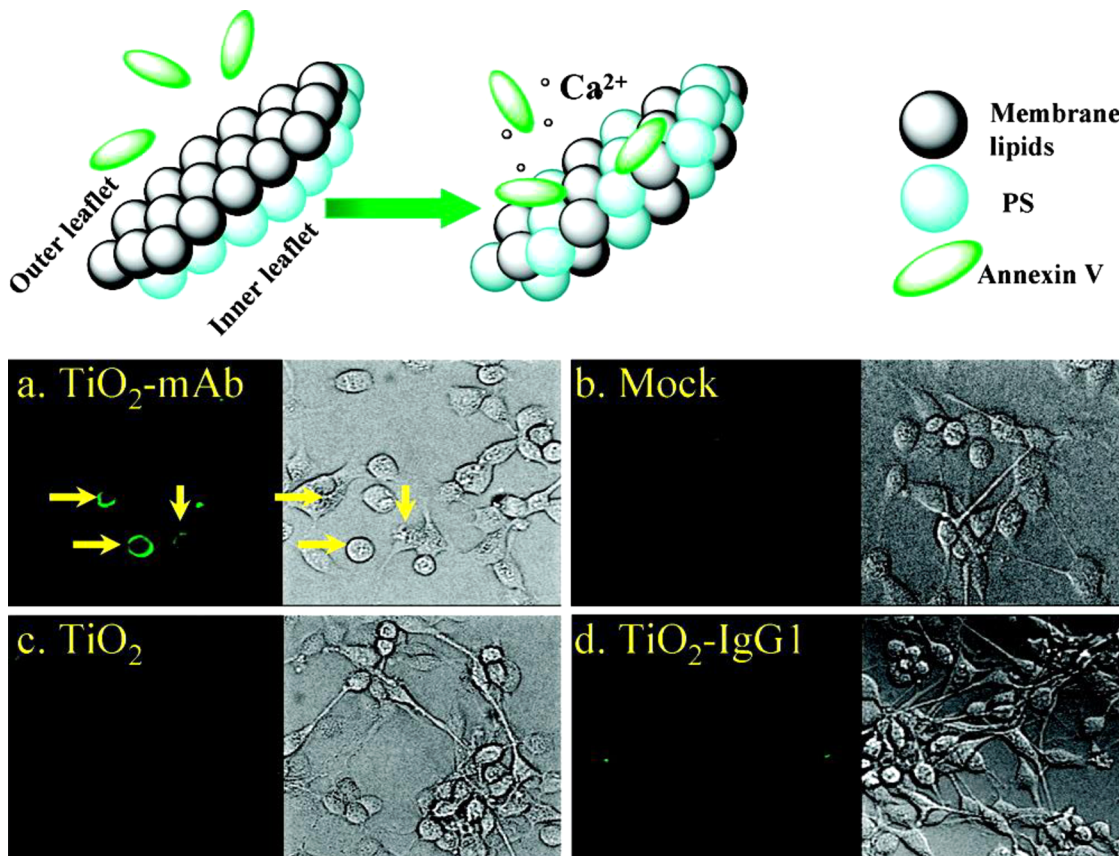


Figure 36. Images of the localization of Annexin V on the outer membrane of the A172 GBM cells after their treatment with TiO_2 -mAb. After illumination the cells were incubated for 6 h and treated with antihuman FITC-labeled Annexin V (a). No Annexin V: FITC luminescence was detected in control experiments without nanoparticles (b) or in cells having bare TiO_2 particles (c); cells with isotype-matched immunoglobulin also did not show binding of Annexin V (d). Adapted from ref 99. Copyright 2009 American Chemical Society.

nano particles (5 nm) conjugated to the antibody enabled specific delivery of nanoparticles to glioblastoma cells specifically. Illumination of incubated cells with a white light for only 5 min (60 mW/cm^2) resulted in notable cell morphology changes. Figure 38 shows laser scanning confocal microscopy images of the cells that were treated with the nanocomposite and are labeled with Mitotracker red to stain the mitochondria. The top image shows cells 90 min after incubation with TiO_2 -alphaIL13 composite where cells are spread on the support without any signs of stress. However, 30 min following light exposure the cells start showing typical morphological changes associated with apoptosis¹⁴¹ such as budding of the cell membrane and cell shrinking. The importance of an apoptotic mechanism as the pathway mediating cell death in TiO_2 -conjugated nanoparticles lies in the fact that the apoptotic cells are rapidly cleared by phagocytosis without eliciting an inflammatory response in the host.

12.2. TiO_2 /Protein Conjugates and Biosensing

Binding of a protein or peptide to TiO_2 can also be exploited to develop simple and sensitive electrochemical biosensors relevant for drug discovery, diagnostics, environmental applications, as well as food safety. TiO_2 is a semiconductor that upon reduction becomes highly conductive and therefore capable of electrochemically responding to the presence of redox species in its environment. Moreover, TiO_2 can be synthesized in a variety of sizes and shapes as well as in the mesoporous form that enables creation of electrodes with high surface area, which, in turn, can significantly increase the signal-to-noise ratio in electrochemical

detection. Several studies have shown that TiO_2 mesoporous electrodes can qualitatively and quantitatively analyze several biomolecules including metabolically relevant redox proteins or tumor markers.

Wang et al.¹⁴² developed a new photoelectrochemical method able to detect NADH at a relatively low potentials using dopamine-modified TiO_2 nanocrystalline films excited by broad visible light (up to 580 nm). Because of the significance of NADH in cellular metabolism and respiration, its quantitative determination is important in studies of biological systems. Many of the detection methods, however, result in irreversible oxidation of the proteins. Recent studies mainly focus on identifying proper electron-transfer mediators that mitigate irreversible oxidation problem.^{143,144} In this approach the indium–tin oxide (ITO) electrode was first covered by colloidal TiO_2 and then modified with dopamine in order to create a charge-transfer complex with TiO_2 via coordinating dopamine with undercoordinated titanium atoms on the electrode surface. These electrodes exhibit an anodic photocurrent under visible light. Importantly, NADH was found to greatly enhance the photocurrent mediated by the electron transfer between NADH and photogenerated holes localized on dopamine. The lowest limit of NADH detection was $1.4 \times 10^{-7} \text{ M}$, and the detection range was linear up to $1.2 \times 10^{-4} \text{ M}$. The TiO_2 electrode modified with dopamine has advantages compared to other NADH detection approaches including fast response and easy fabrication of electrodes for photoelectrochemical determination of NADH. This strategy largely minimizes destructive effects of

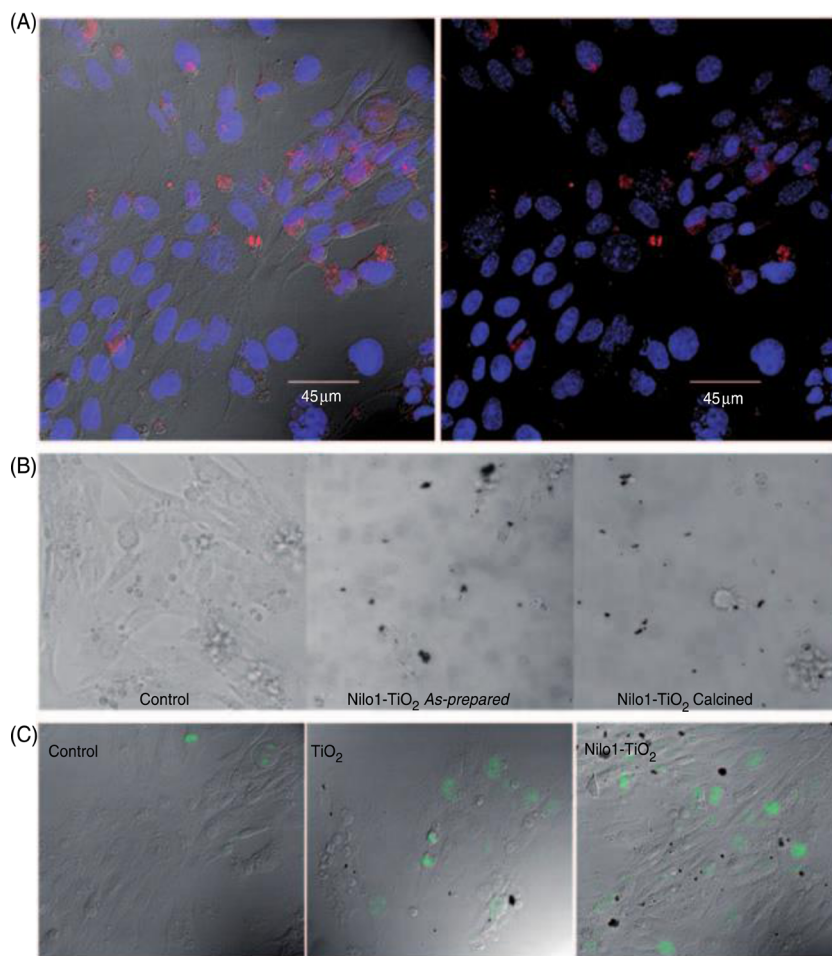


Figure 37. (A) CT-2A astrocytoma cells incubated with Nilo1 labeled by a secondary antibody (red) and Dapi nuclei stained (blue) imaged using confocal microscopy. (B) Bright field of CT-2A cells (left) incubated with as-prepared (middle) or calcined (right) Nilo1–TiO₂ particles after UV irradiation. (C) TUNEL analysis of CT-2A cells in the absence (left) or presence of TiO₂ (central) or Nilo1–TiO₂ particles (right) 6 days after UV irradiation. Adapted from ref 138. Copyright 2010 G. Elvira et al.; SAGE Publications Ltd.

UV light and highly energetic photogenerated holes formed in TiO₂ under UV illumination toward biomolecules and open numerous opportunities for the use of TiO₂ in photoelectrochemical biosensing.

Lin et al.¹⁴⁵ reported a practical method for assembly of an immunosensor based on electrochemical polymerization of polypyrrole propylic acid (PPA) and antirabbit IgG antibody films patterned on TiO₂ nanowires. Observable variations in *I*–*V* signals were detected with interaction of the film and changing concentrations of target rabbit IgG secondary antibody within a linear range of 11.2–112 μg/mL (Figure 39). These results suggested that secondary antibodies were interacting specifically with the immunosensor. The mechanism of detection was explained with the enhanced electron transfer of conducting polymer, due to a change in the electrostatic environment after immobilization of the secondary antibody under the applied bias. The effects of the Schottky barrier were still significant with additional undesirable effects, such as additional bias of about 4 V needed to increase the current flow inside the conductivity channel of the sensing device.

Yamaguchi et al.¹⁴⁶ used covalent linking of 3-aminopropyl trimetoxysilane APTMS and glutaraldehyde coupling linkers to immobilize CD4 peptides to TiO₂ films. Immobilization was studied using AFM and SEM approaches. This coupling allowed for detection and inactivation of HIV-1 viruses (Figure 40). The

figure shows that untreated TiO₂ formed films with the surfaces that were smooth under AFM experimental conditions. During intermediate steps of TiO₂ surface modification with the cross-linkers (first with an amino group followed by an aldehyde group) the surface remained smooth. However, in the third step, when the surface was conjugated CD4 peptides, roughening of the surface was observed. The roughening turned into the bigger islands when HIV-1 virions with a diameter of ~100 nm were incubated on CD4 peptide-modified surface, with the density of islands matching the calculated surface density of virions. Concomitantly, (Figure 40e) the roughness of the surface was barely detectable upon the same treatment without incubation with HIV virions (Figure 40f). These results suggest that modification of TiO₂ with CD4 peptides enables specific conjugation of HIV-1 to the surface of TiO₂. Moreover, the authors have additionally shown that bound virions can be additionally inactivated by UV illumination. Six different serum samples containing HIV-1 virus were deactivated in a single UV illumination treatment using CD4 peptide-conjugated TiO₂. The study also indicated that the CD4 peptide-modified TiO₂ surfaces account for dramatic effectiveness of UV light inactivation of HIV-1 in different primary viral strains, including nonpassaged serum viruses.

In another approach focused on sensing of the alpha-fetoprotein (AFP) an immunosensor for reagentless ampero-

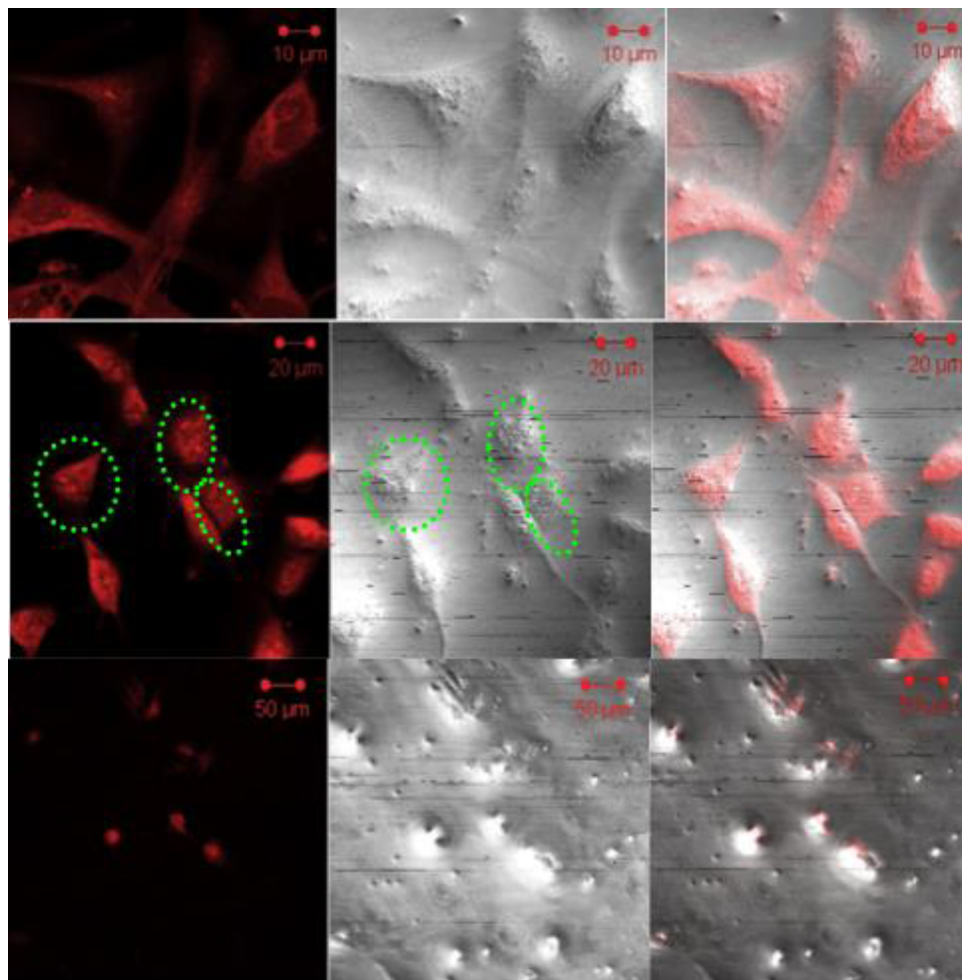


Figure 38. ROS affect cells in their morphology and membrane permeability and cause cell death. Only 5 min of white light illumination with an intensity of 60 mW/cm^2 results in notable cell morphology changes. Images of cells interfaced with the nanobiocomposite: control cells (top), 30 min (middle) and 90 min (bottom) following light exposure using the laser confocal microscope. Green dashed areas denote budding of the cells, an indication of apoptosis. Adapted from ref 140. Copyright 2011 WILEY-VCH Verlag GmbH & Co. KGaA, Weinheim.

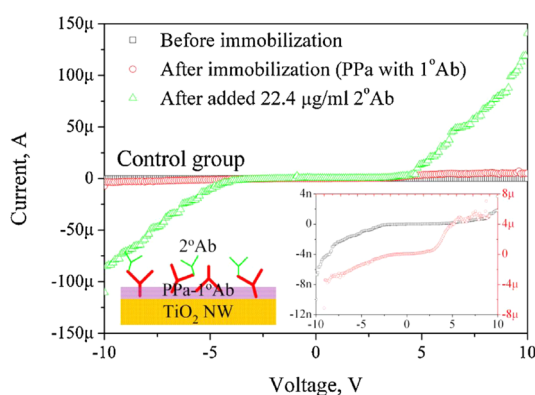


Figure 39. $I-V$ signal response curves of a TiO_2 NWs-based immunosensor. A device without primary antibody (1°Ab) on its surface gives a negligible current change after secondary antibody (2°Ab) addition. In contrast, when 2°Ab is introduced to already immobilized 1°Ab , a current 10 times higher is obtained. A higher current confirms that the immunosensor has the ability to discriminate between immobilized 1°Ab and target 2°Ab . Adapted from ref 145. Copyright 2013 Elsevier.

metric detection was developed by immobilizing TiO_2 colloids on a platinum electrode modified with Prussian blue.¹⁴⁷ AFP is

most widely used as a tumor marker for hepatocellular carcinoma.¹⁴⁸ AFP is also used to detect abnormal development of the fetal brain or spinal cord during pregnancy.^{149,150} TiO_2 with a positively charged interface enabled the adsorption of gold nanoparticles to be used for immobilization of anti-alpha-fetoprotein antibodies (anti-AFP). Cyclic voltammograms showed a response specific to AFP. AFP was detected in two concentration ranges, one from 3.0 to 30.0 ng/mL and other more concentrated from 30.0 to 300.0 ng/mL with a detection limit of 1.0 ng/mL. The immunosensor displayed a high selectivity, suitable reproducibility, and lasting stability. The sensitivity of the sensor was improved when TiO_2 nanoparticles were coprecipitated with CdS nanoparticles leading to visible absorption of light. The immunosensor displayed a linear response to AFP in the range from 50 pg/mL to 50 ng/mL with a relatively low detection limit of 40 pg/mL.¹⁵¹ A similar approach was used for development of anticarcinoembryonic antigen (CEA) modified immunoselective electrode in which graphene oxide was used instead of Prussian blue.¹⁵² CEA is a biomarker that is present at ultralow levels in the early stages of colon cancer,^{153,154} and it is very important to explore new methods for signal amplification to increase the sensitivity of detection. The CEA immunosensor displayed a linear response to CEA in two ranges from 0.1 to 10.0 ng/mL and from 10.0 to 120.0 ng/mL

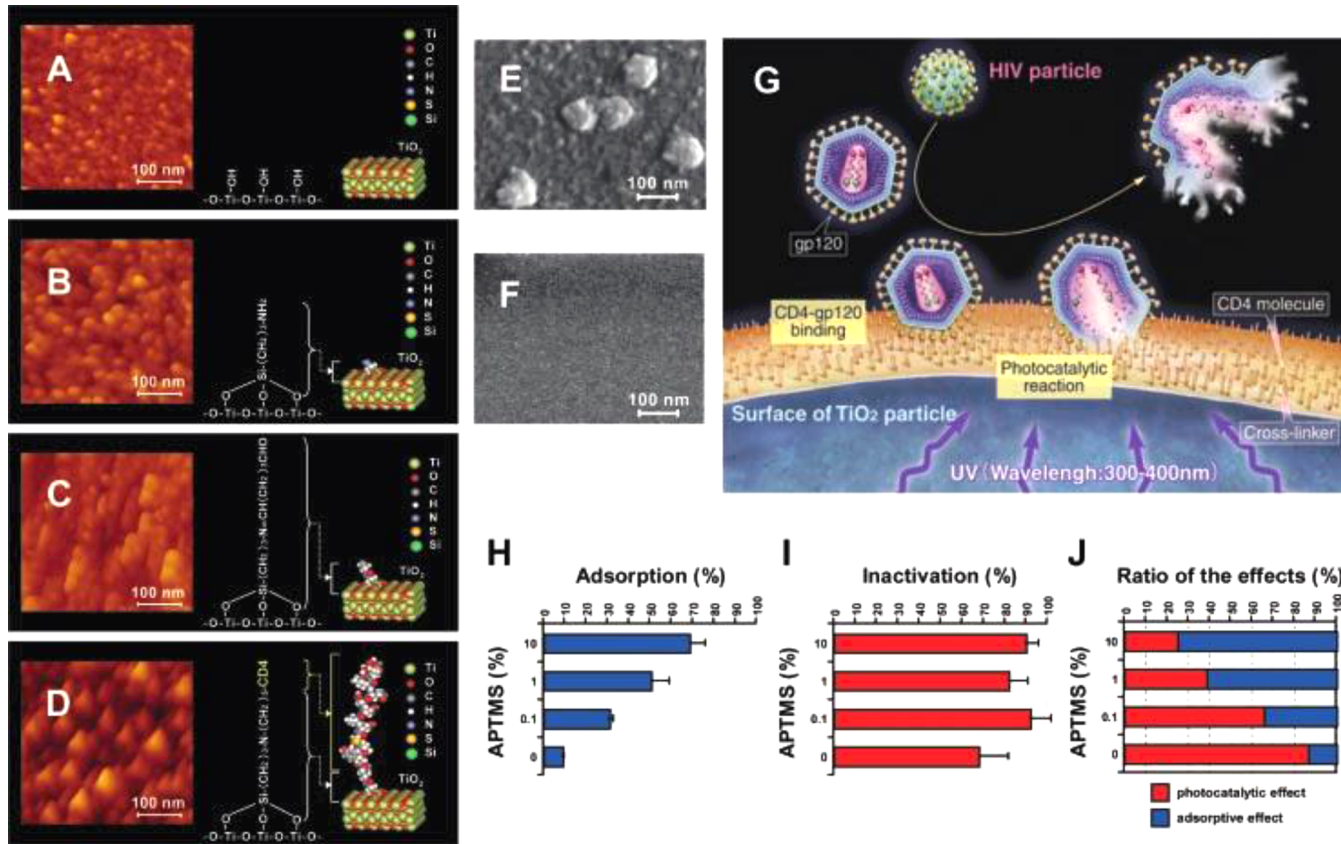


Figure 40. AFM images of the surface of TiO₂ upon conjugation with CD4. (A) Untreated surface. (B) First cross-linker with an amino group conjugation. (C) Second cross-linker with an aldehyde group conjugation. (D) CD4-conjugated TiO₂. (E) Immobilization of HIV viron with a diameter ~100 nm on the CD4-TiO₂. (F) Untreated surface. (G) Schematic presentation of viral UV inactivation on the CD4-TiO₂. (H) Effectiveness of adsorption of HIV viron on CD4-TiO₂. (I) Effectiveness of inactivation (both adsorption and photocatalytic action) of CD4-TiO₂. Results are shown as percent adsorption or inactivation derived from comparisons with untreated controls. (J) Relative contributions of photocatalysis and adsorption to the total inactivation effects. Adapted from ref 146. Copyright 2008 Wiley-Liss, Inc.

with a relatively low detection limit of 0.01 ng/mL. RGD-Y peptide was also used for immobilization of intact cells (MC3T3-E1 cell line) to the surface of TiO₂. Immobilization of RGD-Y-terminated peptide was developed based on the tyrosinase-catalyzed oxidative reaction that may be used as a sensor for intact cell analysis.¹⁵⁵ Wang et al.¹⁵⁶ developed an impedance-based immunosensor that was capable of sensing bacteria, namely, *Listeria monocytogenes*, using its selective binding to anti-Listeria antibody. These new approaches for sensing intact cells are expected to open entirely new areas that would increase our understanding of biotransformations during metabolic events giving insight into intracellular redox cofactor analysis and enzyme kinetics that determine cellular metabolic functioning.

13. DRUG DELIVERY

Unlike traditional therapies, which exhibit peaks and troughs of drug concentration, time-release drug delivery systems are designed to maintain steady-state drug therapeutic levels during the extended treatment periods. A controlled time-release drug delivery vehicle is able to control the time and rate of drug delivery. A site-selective drug delivery vehicle is able to localize delivery to a targeted area of the body. Both controlled time release and site selectivity are desirable characteristics. In addition, an ideal drug carrier should possess a high surface area in order to foster significant drug adsorption but also an appropriate pore size to accommodate the size of the drug. A sufficiently large pore volume is needed to incorporate the

required amount of a drug into the pore matrix. A relatively homogeneous pore network is also needed in order to control the uniform drug release kinetics. A desirable feature would be the ability for surface functionalization to provide additional control over drug loading and release.

These requirements make mesoporous materials excellent contenders for controlled drug-delivery systems. In particular, TiO₂ structures, with unique undercoordinated surface sites that enable facile and controlled surface functionalization, are an ideal material for the design of drug carriers. The capability to systematically engineer the shape and size of TiO₂ nanoparticles brings additional control of their electronic and chemical properties resulting in new opportunities for more efficient site-selective chemistry. In addition, nanoparticles with light activating chemistry, so well controlled in TiO₂ systems, can make an excellent vehicle for a light-induced drug delivery. This stimuli-responsive approach is of particular interest for delivery of toxic drugs that require very low tolerance for premature release.

Several approaches have been developed for restricting delivering of toxic agents other than ROS to the diseased tissue using TiO₂ platforms while minimizing side effects. The first approach is to use amphiphilic hollow structures such as nanotubes that accumulate hydrophilic drug within the interior hydrophilic structure.¹⁵⁷ In order to avoid undesired nonspecific adsorption of abundant proteins (e.g., bovine serum albumin)¹⁵⁸ to the drug delivery vehicle and concomitantly prevent fast drug

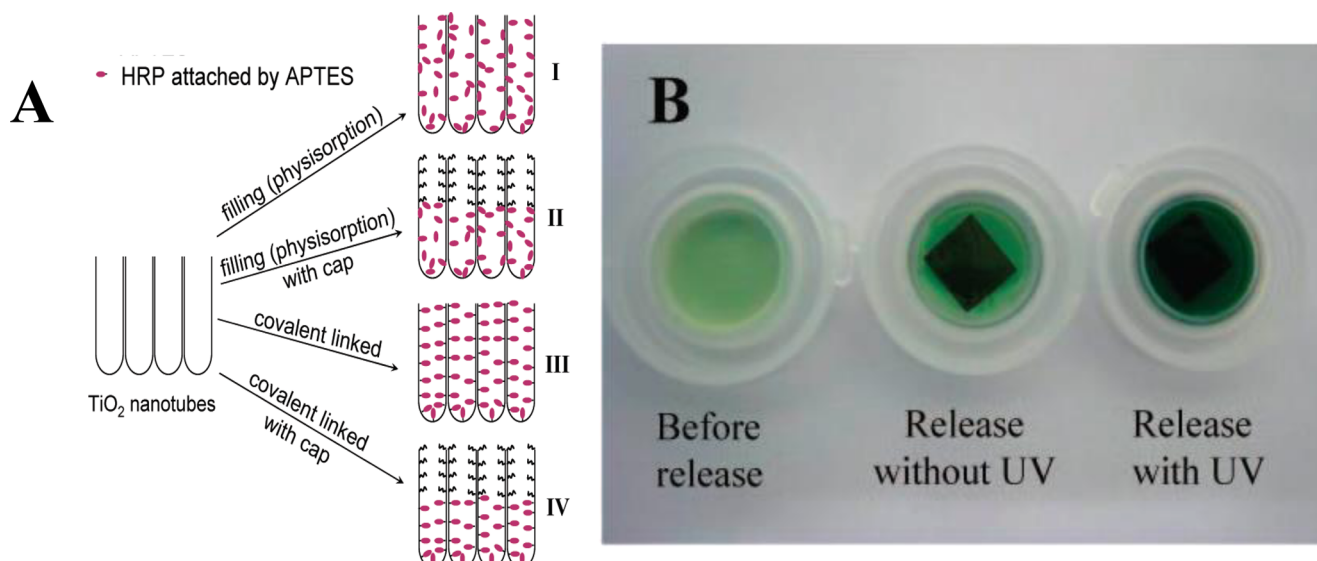


Figure 41. (A) Horseradish peroxide (HRP) assisted drug loading: (I) No TiO_2 surface modification (control), (II) hydrophobic modification of the upper nanotube layer with OPDA (hydrophobic cap), (III) covalent linking of HRP over the entire nanotube, (IV) both OPDA hydrophobic cap and covalent linking of HRP in the bottom of the nanotube. (B) Images of nanotubes immersed in solution in the presence of a HRP indicator and H_2O_2 before (left) and after HRP release without (middle) and with UV illumination for 40 min (right). Adapted from ref 157. Copyright 2009 American Chemical Society.

release, the top of the mesoscopic structure was surface modified with hydrophobic ligands (Figure 41). In the case when horseradish peroxide, a model for hydrophilic drugs, was physisorbed in the TiO_2 nanotubes without covalent linking (I in Figure 41A), release of the model drug was fairly fast with a rate constant of $k = 1.32 \times 10^{-2} \text{ s}^{-1}$. On the other hand, when a hydrophobic stopper was applied to the nanotubes, release was controlled by the intensity of UV illumination; the greater the UV intensity, the more rapid the release rate (in fact, the kinetic constants $k_{\text{high}} = 8.21 \times 10^{-4} \text{ s}^{-1}$ and $k_{\text{low}} = 3.74 \times 10^{-4} \text{ s}^{-1}$ directly correlated with the light intensity). UV light produced radical species that attacked hydrophobic chains as well as ligands that covalently link the drug to the mesoporous support, releasing it to the surrounding environment. Release of the drug without UV radiation was very slow (Figure 41B). A similar study was also performed with nanotubes that were modified with magnetic nanoparticles, improving tissue targeting of drug release structures.¹⁵⁹

Another approach used TiO_2 primarily as a drug carrier and involved relatively weak attachment (physisorption) of oxygen-rich drug daunorubicin on anisotropic whisker structures of TiO_2 .¹⁶⁰ This study took advantage of strong fluorescence of the drug and using confocal microscopy showed that integration of the drug with TiO_2 particles (P25) as well as whiskers lead to a different mechanism of drug uptake. Upon incubation with the cells, the TiO_2 –daunorubicin composite delivered strong fluorescence to the cells that was more pronounced in the case of TiO_2 whiskers than P25 nanoparticles. Fluorescence was observed exclusively in the cell regions, with drug-modified nanoparticles showing localization in the cytoplasm and drug composites with whiskers showing strong luminescence in the nucleus as well. These results suggest that whisker composites upon entering the cell separate from the drug molecules, which are then able to enter the nucleus. The strength of the composite is expected to be greater in the case of nanoparticles due to the presence of five-coordinated sites that complete their coordination by binding to oxygen-rich ligands, hindering release of the

drug. UV illumination promotes mortality of cells beyond the one induced by the drug alone, and the survival fraction of cells was found to be dependent on the duration of UV irradiation. More recent studies involve delivery of doxorubicin, one of the most extensively used chemotherapy agents.¹⁶¹ In one of these studies¹⁶² the authors observed pH-dependent release of the drug containing noncovalently bound drug to EDTA-modified TiO_2 nanoparticles (7–9 nm), and doxorubicin was found inside the cell nucleus, similar to the results obtained using daunorubicin, a 1-methoxy analog of doxorubicin. In another study¹⁶¹ the authors showed that the nanoparticle composites (6–8 nm $\text{Fe}_2\text{O}_3@\text{TiO}_2$ core–shell structure) found their way to the cell cytoplasm and to a lesser extent to the nucleus. They also found that drug–nanoparticle composites eliminated resistance to anthracyclines and offered enhanced doxorubicin delivery to the cancer cells that overexpress phosphoglycoprotein (pgp) (Figure 42). The study also found that drug–nanocomposites increased the uptake of transferrin-tagged therapeutic agents.

Site-selective delivery of the drugs was explored using hollow TiO_2 nanoparticle structures that were surface modified with monoclonal antibodies.¹⁶³ Hollow TiO_2 nanoparticles were functionalized with antihuman epidermal growth factor receptor 2 antibody Herceptin and applied to human breast cancer cell line SK-BR-3. The composites were efficiently internalized into the cell owing to the enhanced binding of the antibody to the EGFR expressed on their membrane (Figure 43). The hollow particles were also loaded with the camptothecin anticancer drug, and in 24 h they released an entire load of the drug-producing efficient anticancer activity. As cellular uptake of antibody-labeled nanoparticles was not efficient in nontransformed cells, the particles produced little cytotoxicity in healthy cells.

14. IMAGING GUIDED THERAPY

As the targeting therapies are focusing to a single cell level resolution, including isolated stem cells, reducing off-target effects by directing therapeutic agents to localized targets is becoming particularly important. New miniaturized sensors and

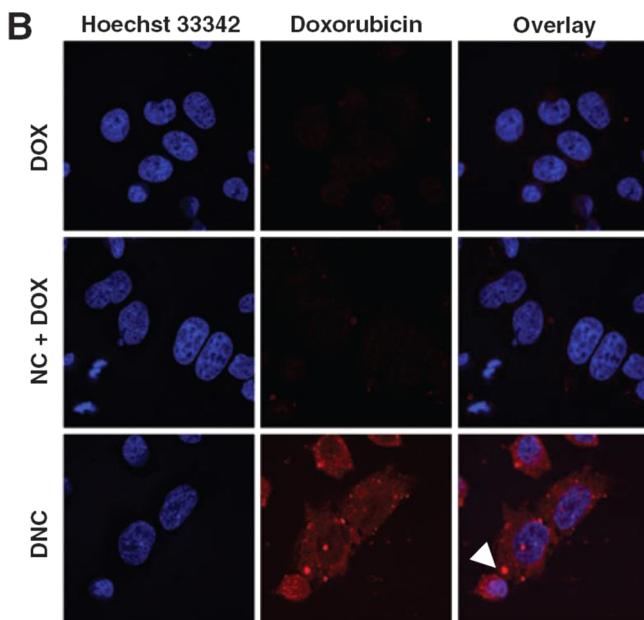


Figure 42. A2780/AD cells that overexpress pgp, treated with doxorubicin alone, cotreated with nanocomposites, and incubated with doxorubicin-coated nanoparticles. Drug resistance to doxorubicin is typically mediated by overexpression of pgp, a membrane transporter that actively pumps doxorubicin out of the cell. As a consequence, A2780/AD cells showed almost no doxorubicin accumulation when treated with doxorubicin alone or doxorubicin added with nanoparticles separately. On the contrary, cells treated with nanoparticles coated with doxorubicin showed doxorubicin signal in both the nucleus and the cytoplasm, preventing the resistance caused by overexpression of pgp. Adapted from ref 161. Copyright 2012 American Association for Cancer Research.

actuators are needed to achieve permanent destruction of diseased tissues or suppression of pathological processes. Many of the new advances in medical therapeutic principles involve energy-based approaches with direct energy deposition within the cellular machinery, although the underlying molecular mechanisms are not yet fully understood. Drug delivery systems activated by heat, magnetic fields, ultrasound, or light are being investigated. Several factors are important for the molecularly targeted therapies among which prevention of premature release is one of the most important ones. This can be achieved by associating a drug to carriers that facilitate accumulation of the drug at the target site before energy that activates the carrier is deposited. In this approach monitoring of the drug carrier localization before energy deposition as well as during energy deposition is needed. This is an important concept but at the same time a challenging problem as additional imaging agents (e.g., contrasts) have to be incorporated in the drug delivery vehicles to ensure reliable tracking of the delivery.

Optical imaging and, in particular, SERS (surface-enhanced Raman spectroscopy), MRI (magnetic resonance imaging), EPR, PET (positron emission tomography), and ultrasound are techniques of choice for monitoring drug delivery and the effects of the energy deposition in the targeted tissue. While optical imaging and SERS have by far the greatest resolution that can visualize structures on the subcellular scale, MRI, PET, and ultrasound have the advantage of being widely used as diagnostic tools. Although exceptionally suited for photocatalytic applications, TiO_2 itself is not intrinsically suited for imaging purposes as it has very faint fluorescence for optical imaging, it has a Raman

band in the very low energy region ($\sim 100\text{--}300 \text{ cm}^{-1}$), it is not magnetic, and it does not have a substantially large atomic number to have significant contrast in X-ray measurements. However, as described earlier, TiO_2 is the most efficient of all nanoparticulate systems in performing redox reactions, which is a most important prerequisite for practical application in biomedical therapies. Therefore, adapting TiO_2 nanostructures to gain properties for cell imaging with each of the above-mentioned monitoring techniques offers a potential prospect for future powerful applications of nanoparticle-based photodynamic therapies.

Modification of TiO_2 nanoparticles with optical fluorescent dyes was achieved using enediol dye Alizarin Red S (ARS).¹⁶⁴ Due to the bidentate coupling to TiO_2 nanoparticles to alizarin dye a charge-transfer complex is formed that has optical properties different from those of free alizarin. Absorption of the conjugate is shifted to the visible region of the optical spectrum with an enhanced extinction coefficient compared to that of free alizarin. Therefore, illumination of the complex with visible light ($\lambda_{\text{exc}} = 543 \text{ nm}$) resulted in the *red* fluorescence of the complex ($\lambda_{\text{em}} = 560\text{--}615 \text{ nm}$), while excitation of free alizarin with the same excitation light does not lead to free alizarin fluorescence in the same optical window (Figure 44). This method allows for direct imaging of the TiO_2 nanoparticles using fluorescence microscopy. These particles are otherwise invisible without alizarin modification. Additionally, the authors showed that labeling of TiO_2 nanoparticles can be performed even after incubation with the cells, enabling visualization of already targeted nanoparticles (Figure 44B). Simultaneous imaging using confocal microscopy and X-ray fluorescence on the same cell sample confirmed colocalization of the alizarin fluorescence and TiO_2 nanoparticles. These measurements also showed that as few as 7.9×10^4 alizarin molecules immobilized on TiO_2 nanoparticles (44% surface coverage) were sufficient to efficiently visualize TiO_2 using confocal microscopy.

In another study mesoporous TiO_2 nanoparticles were labeled with phosphate-containing flavin molecule (Riboflavin 5P').¹⁶⁵ It was known from previous research of the dye-sensitized solar cells that phosphonic acid derivatives adsorb strongly to TiO_2 surface but do not promote electron transfer from the dye to TiO_2 .¹⁶⁶ Therefore, binding of dyes through a phosphonic groups holds promise for efficient conjugation to TiO_2 surface that does not promote quenching of the dye fluorescence. The flavin– TiO_2 particles were incubated with BT-20 breast cancer cells in the presence of a cell membrane impermeable anticancer drug (Doxorubicin). Four hours after incubation it was found that flavin– TiO_2 composites were localized in the cytoplasm, as determined using fluorescence confocal microscopy. The study indicated that flavin dye remained linked to mesoporous TiO_2 without significant leaching.

The excellent suitability of TiO_2 nanoparticles for Raman imaging in biological environment was recently shown for nanoparticles functionalized with enediol ligands. It was found that bidentate modification exhibits enhanced Raman scattering compared to the Raman scattering of the free modifier alone. The enhancement was a consequence of the creation of a charge-transfer complex. As electromagnetic enhancement in TiO_2 is very small (a factor of 3 due to the dielectric cavity effects) the authors attributed the chemical mechanism of Raman enhancement as a dominant effect in surface-modified semiconductor nanoparticles. Remarkably, these functionalized semiconductor nanoparticles achieve 10^3 Raman enhancements in the individual nanoparticles in solution (unlike metallic nanoparticles in which

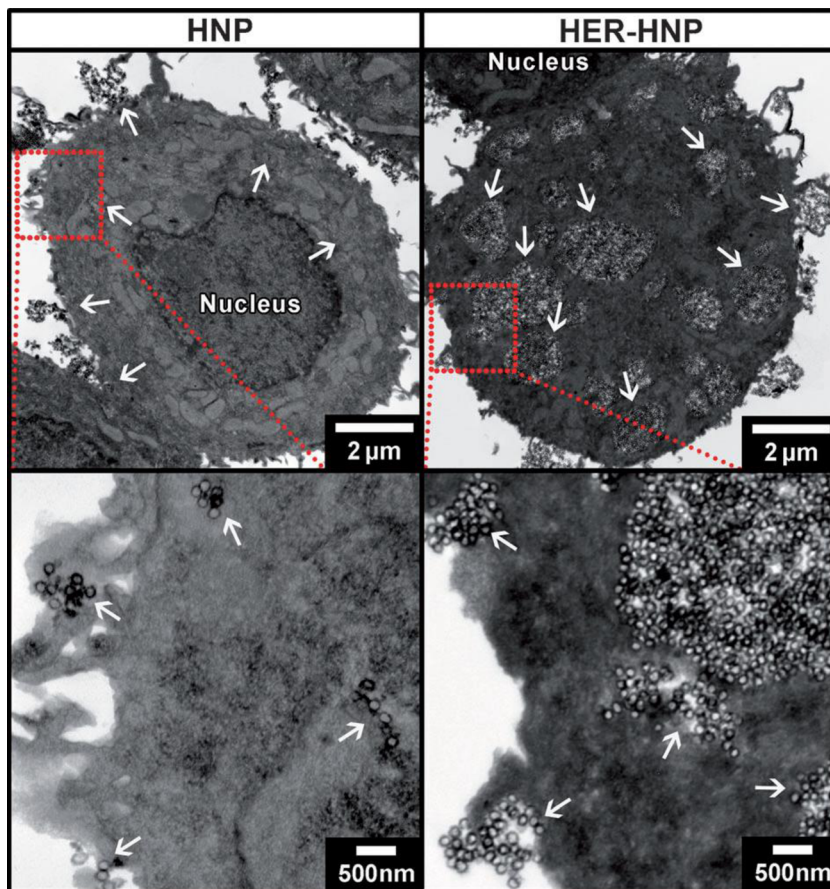


Figure 43. TEM imaging of cellular uptake of TiO_2 hollow nanoparticles and Herceptin-modified nanoparticles by SKBR-3 cells over 24 h. Hollow nanoparticles were used as a carrier of camptothecin drug. Reprinted with permission from ref 163. Copyright 2012 Wiley-VCH Verlag 4902 GmbH & Co. KGaA, Weinheim.

nanoparticle aggregates carry out largest enhancements). Sizable detection of the Raman scattering of individual nanoparticles opens the possibilities of using ligand-modified nanoparticles as Raman scattering dyes. Moreover, different ligands enhance at different frequencies of the infrared spectrum, suggesting the possibility of multiplexing with different ligand modifications.^{167–170}

Enediol ligands bound to TiO_2 were also used as a vehicle to connect paramagnetic probes for magnetic imaging. Gadolinium(III)-containing compounds are the most commonly used contrasting agents in MRI, in particular, for imaging of internal body structures such as in MR angiography or tumor detection. MRI of tissue anatomy and function is based on the imaging of two hydrogen atoms in water that produce the contrast. In addition to differences in the local water content, the essential contrast in the MR image is primarily the outcome of regional dissimilarities in intrinsic relaxation times of two hydrogen atoms in water due to their interaction with different neighboring molecules.¹⁷¹ Gd(III) chelates interact with the protons in nearby tissues and shorten their T_1 relaxation time and at the same time enhance the rate of stimulated emission occurring by relaxation of the nuclear spin from high-energy states (nuclear spin antialigned with the main field) to low-energy states (nuclear spin aligned), enabling dynamic enhancement of the imaging of protons in a nearby tissue. In contrast, MRI nanoparticle probes such as iron oxide and platinum–iron nanoparticles alter T_2 relaxation to yield T_2 -weighted MR images that create negative contrast. Negative contrast is often a subject

of misinterpretation due to background artifacts.^{172–174} Gd imaging, on the other hand, enhances the contrast by increasing both T_1 and T_2 signals, enabling positive identification of structural changes and enhanced fine structure of the internal tissue.^{175,176}

Gd–DO3A is a contrasting agent typically used for imaging of the pathologies associated with the central nervous system and extracranial/extraspinal tissues that results in blood–brain barrier breakage and perfusion deficiency (commercial name ProHance). In order to couple MRI imaging with photodynamic therapy, Gd–DO3A dopamine conjugate was synthesized by linking a succinimidyl ester derivative of DO3A chelate with dopamine in the presence of GdCl_3 .¹⁰⁰ The conjugate was integrated with TiO_2 nanoparticles as well as mitochondrial DNA (also labeled with dopamine), resulting in a construct that showed detectable enhancement of T_1 -weighted signal that appeared to colocalize with DNA in targeted mitochondria. In the later refinement of this approach the authors conjugated the chelate and dopamine to polyglutamic acid via intermediate succinimide ester and linked it to already DNA-modified TiO_2 nanoparticles. This complex seemed to have much better stability than the one obtained by simultaneous conjugation of all complex constituents. The complex also contained a high Gd to TiO_2 molar ratio (630:1), leading to localization of magnetic contrast that results in a high signal-to-noise ratio. Indeed, it was observed that the concentration of Gd in nanoconjugate-treated cells was 1000-fold greater than that in cells treated with Gd chelate alone.¹⁷⁷ Additionally, the authors found unprecedented

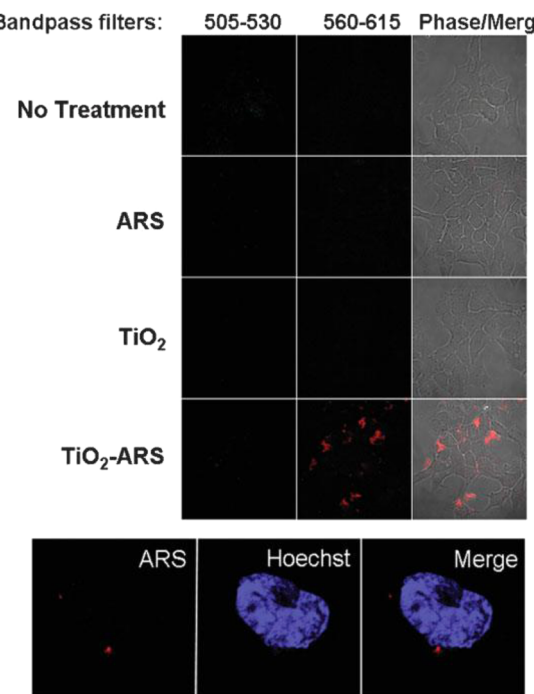


Figure 44. Detection of ARS-modified TiO_2 nanoparticles in PC-3 M cells. (Top) Cells treated with PBS, ARS, TiO_2 nanoparticles, or TiO_2 -ARS. A strong fluorescent signal was obtained only in cells incubated with TiO_2 -ARS using a 560–615 nm band-pass filter (excitation = 543 nm). (Bottom) TiO_2 nanoparticles in fixed cells. Cells incubated with TiO_2 nanoparticles, washed, fixed, and stained with Hoechst 33342 to stain the nucleus (blue). After that cells were treated with ARS (red) in PBS to stain the internalized nanoparticles. Black fields indicate no fluorescence. Reprinted with permission from ref 164. Copyright 2009 Wiley-VCH Verlag GmbH & Co. KGaA, Weinheim.

prolonged retention of Gd contrasting agent in the treated cells 48 h after treatment, holding promise for a wealth of new approaches in dynamic contrast-enhanced MRI. X-ray colocalization of Ti and Gd with biogenic elements shows that Ti and Gd follow localization of P and Zn associated with the cell nucleus (Figure 45), suggesting intracellular nanoconjugate accumulation. This target-dependent retention of Gd, due to the selectivity of DNA attached to the nanoparticles (genomic DNA

was used in this study), suggests that the imaging can be specific for different cell types or subcellular localities, further increasing the resolution and specificity of Gd-containing contrasting agents in MRI imaging.

Recently, Chandran et al.¹⁷⁸ reported an alternative approach based on Gd doping of amorphous TiO_2 nanoparticles that was also found to affect the T_1 relaxation time of surrounding protons by shortening their lifetime, producing a positive contrast enhancing effect. The authors found that this property is obtained only in amorphous porous TiO_2 structures that enable unhindered exchange of protons between nanoparticle and surrounding water. Annealed anatase and rutile samples loose this ability due to the crystallization of the sample. Very low doping levels (~ 2 mol %) showed stronger concentration-dependent T_1 -weighted signals than commercial Gd-chelate agents at the same concentration. Cytotoxicity studies show that Gd-doped samples mirror the behavior of TiO_2 itself and do not show significant dark toxicity in blood or primary endothelial cells up to a concentration of 200 $\mu\text{g}/\text{mL}$. Even under exposure to light both doped and undoped amorphous samples did not produce observable evidence of stress caused by intracellular ROS production (although it is not clear what light source for illumination of the samples was used in this work). These results also suggest that amorphous TiO_2 is not suitable for photocatalytic applications. Amorphous TiO_2 , however, presents a viable candidate for molecular imaging in accordance with its biocompatibility.

TiO_2 nanocomposites were also labeled with radiolabeled oligonucleotides, opening a new approach for functionalized PET imaging.⁹² We have shown that TiO_2 -DNA can be hybridized using ^{32}P radioactively labeled oligonucleotides that could be used for extremely sensitive radioactive imaging of nanoparticles. Additionally, one can envision that instead of beta-emitter ^{32}P positron-emitting isotopes with short half-lives such as ^{11}C (20 min), ^{13}N (10 min), ^{15}O (2 min), ^{64}Cu (17.2 h), or ^{18}F (110 min) can be used for obtaining high-resolution PET imaging. Additionally, cleavage of the double-stranded DNA from the TiO_2 nanoparticles was observed after different times of exposure to ^{32}P radioactivity covalently linked to TiO_2 nanoparticles. Note that exposure of oligonucleotides hybridized with complementary ^{32}P -labeled strand, which was not

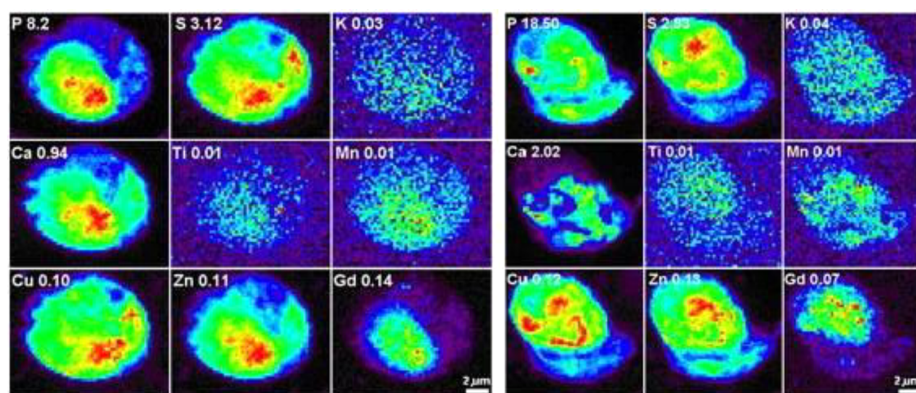


Figure 45. X-ray fluorescence mapping of MCF-7/WS8 cells transfected with TiO_2 -DNA oligonucleotide-Gd contrasting agent. Elemental maps were obtained by imaging spatial distribution of P, S, K, Ca, Ti, Mn, Cu, Zn, and Gd in cells treated with nanoconjugates for 24 h. Elemental maps pictured in a rainbow color scale from the highest concentration (red) to the lowest signal (black) are used to show the range of concentrations in the sample. Highest concentrations are given adjacent to the element symbol and expressed in $\mu\text{g}/\text{cm}^2$. Reprinted with permission from ref 177. Copyright 2008 Elsevier.

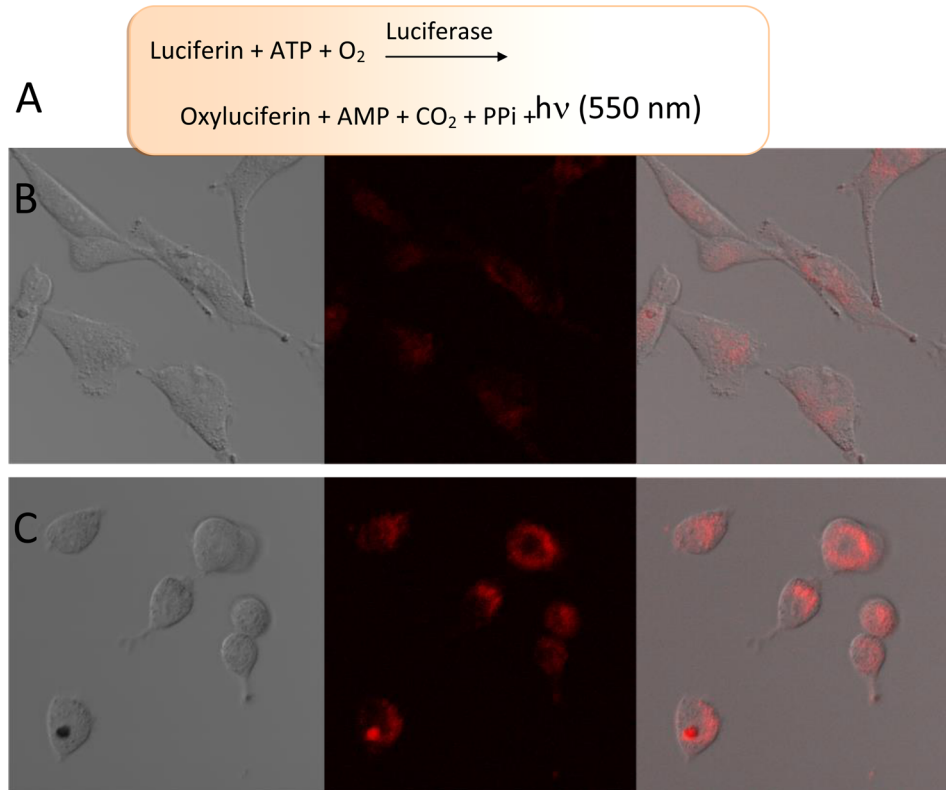


Figure 46. (A) Scheme depicting the mechanism of luciferase bioluminescence used for activation of TiO_2 nanoparticles. (B) Untreated A172 cells stained with Mitosox dye that emits red fluorescence when it interacts with superoxide. (C) A172 cells following 2 h of treatment with the TiO_2 –luciferase nanoparticles in the presence of luciferin.

covalently linked to TiO_2 nanoparticles, did not show any cleavage under the same experimental conditions.

15. CONCLUDING REMARKS AND FUTURE DIRECTIONS

There is great interest in applying nanotechnology solutions in biomedicine. Nanotechnology offers materials designed at the nanometer level that provide properties that are largely unavailable in bulk materials of the same composition and have the ability to be integrated with biological molecules of similar sizes. In particular, the high surface-to-bulk ratio of metal oxide nanomaterials offers the unique possibility of linking multiple biological molecules (probes) to the surface of each nanoparticle using precise engineering of their surface. These biomolecules, in turn, affect the chemistry of nanoparticles and mediate their activity. TiO_2 nanoparticles with their extraordinary stability, exceptional photoreactivity, and biocompatibility have a special place in biomedical solutions of the future. This field, which began in the 1990s, is growing exponentially and has now expanded into an area of great importance and impact.

In this review, we have shown that TiO_2 is able to control and initiate chemical reactions within the cell environment. Nanoparticles modified with “conductive leads” and integrated with antibodies established effective light-induced crosstalk across the interface between biomolecules and metal oxide nanoparticles. Furthermore, functionally integrated TiO_2 –antibody complexes retain the photocatalytic properties of nanoparticles and recognition properties of monoclonal antibodies. Antibodies provide a highly selective specificity to the metal oxide nanoparticles, increasing their retention on targeted cells expressing cognate antigens on the membrane surface. In this

way, composites are activated only in close proximity to biological targets of interest, such as cancerous cells, while not injuring nearby healthy cells. This specificity and targeting affinity, in turn, can be used for multimodal imaging of targeted cells or for drug delivery. The therapeutic potential of TiO_2 lies in the ability of these particles in response to light to produce reactive oxygen species (singlet oxygen and superoxide radicals). These radical species can alter respiratory pathways in mitochondria and cause the release of electron-transfer proteins that trigger programmed cell death (apoptosis). These new nanoscale photodynamic therapeutic agents can attack cancer cells while leaving healthy cells unharmed. These functionalized nanoparticles provide a promising new platform for detection and treatment of human diseases.

The ability of TiO_2 nanoparticles to initiate electron-transfer reactions within DNA molecules holds additional promise for the biomedical revolution occurring in the stem cell arena. The promise of creating new life from stem cells was greatly advanced in 2006 when Yamanaka et al.¹⁷⁹ discovered that when the genes that coded a set of four proteins were introduced into mouse skin cells the cells became reprogrammed into ones that closely resembled embryonic stem cells. Electron transfer in DNA that results in cleaving of DNA fragments initiated by light also holds promise of reprogramming gene coding either by deleting or by inserting gene codons. Taking into account that these nanocomposites can be introduced into the cell nucleus, one can hypothesize that these composites can be used as endonuclease during gene surgery in vitro and in vivo. Moreover, one can speculate that TiO_2 nanoparticles with their strong reactivity upon exposure to light might participate in the methylation/demethylation of the DNA, participating thereby in epigenetic

gene regulation in development of a disease or by altering DNA expression as cells differentiate.

The existing challenge associated with *in vivo* use of TiO₂ nanoparticles in advanced medical therapies lies in finding a way to deliver light to TiO₂ deep in the tissue. Although the use of UV light for sensitization of bare TiO₂ particles seems to be feasible in the treatment of skin diseases (psoriasis, melanoma, etc.), exposure of healthy cells to increased amounts of UV light continues to present a stumbling block. Therefore, finding ways to sensitize TiO₂ nanoparticles in the visible region or activating them by other energies (e.g., magnetic fields, NIR light, X-rays) that penetrate deep through the tissue remain major challenges for application of TiO₂-driven therapies.

In this regard, recently TiO₂ was shown to behave as a sonocatalyst. Specifically, the presence of TiO₂ particles enhances hydroxyl (OH[•]) radical production by ultrasound irradiation even in dark conditions.^{180,181} Ultrasound is already employed for some cancer therapies, either by generating high-intensity focused heating or by a drug release activated by low-intensity ultrasound irradiation. It was shown that a 1 MHz ultrasound will penetrate about 4 inches below the skin and can be used for activating TiO₂ nanoparticles deep below the skin surface. Also, activation of TiO₂ nanoparticles covalently linked to radioactive probes⁹² can be used for efficient treatment of cancers in deep tissue. Very small radiation doses of electron/positron-emitting radioisotopes can be selectively delivered to already distributed TiO₂ nanoparticles, targeted to cancer cells via DNA or monoclonal antibodies. After isotope binding, reactive (oxygen) radical species, produced by interaction of radiation with TiO₂, can participate in the activation of cell death. Raman activation of TiO₂ nanoparticles also holds promise to be used for photodynamic diagnosis or therapy.^{182,183} Creating light *in situ* using bioluminescence is another exciting approach that can be used to activate TiO₂ particles when they are already attached to cancerous cells (Figure 46).¹⁸⁴ Then, upon delivery of activating molecules, just like Feynman's prediction states, "...the surgeon [TiO₂] takes a little knife [ROS] and slices it out".¹

AUTHOR INFORMATION

Corresponding Author

*Phone 630-252-5334. E-mail: rajh@anl.gov.

Notes

The authors declare no competing financial interest.

Biographies



Tijana Rajh is a Senior Scientist and a group leader in the Center for Nanoscale Materials at Argonne National Lab. She has extensive experience in the synthesis and study of colloidal semiconductor

nanocrystals and their integration into hierarchical assembly. She conducted some of the earliest research on quantum dots, a scientific area that has grown enormously and is of great current interest and impact. Her early studies involved electron-transfer reactions and photoelectrochemistry of colloidal semiconductors and quantum dots as well as solar energy conversion into chemical fuels. She developed methods for seamless electronic integration of chelating ligands and colloidal semiconductors creating hybrid properties between nanoparticles and organic/biological molecules. Her current research activities focus on exploring nanoparticles in light-induced chemistries, energy storage, and integration of nanoparticles with biomolecules.



Nada Dimitrijevic is a scientist in the Chemical Sciences and Engineering Division at Argonne National Laboratory. She has extensive experience in light-induced charge separation, heterogeneous photocatalysis, and synthesis and characterization of nanoparticles. She conducted some of the earliest research on nano-TiO₂ and quantum dots as photocatalysts for solar energy conversion. Her current research activities focus on exploring nanoparticles for photocatalytic conversion of CO₂ into fuels and in exploring charge separation across nanoparticle–biomolecule interfaces.



Marc Bissonnette, M.D., is an Associate Professor of Medicine in the Section of Gastroenterology at the University of Chicago. He is a gastroenterologist whose research focuses on colonic tumorigenesis and chemoprevention. His research interests include interactions between diet and host that modulate growth factor signals in the colon. He is also investigating the roles of stroma and epigenetic regulation, including microRNAs in tumorigenesis. In addition, he is studying chemopreventive agents including vitamin D and fish oils that suppress Western diet-related tumor-promoting signals.



Tamara Koritarov is a graduate student at Boston University and a Research Aid at the Center for Nanoscale Materials at Argonne National Laboratory. Her current research interest is to develop a photodynamic therapy with TiO_2 to be used as a treatment for cancer.



Vani Konda, M.D., is an Assistant Professor at the Center for Endoscopic Research and Therapeutics and the Section of Gastroenterology in the Department of Medicine at University of Chicago Medicine. She is a gastroenterologist who specializes in the diagnosis and treatment of Barrett's esophagus and manages esophageal diseases, colon cancer screening and surveillance, and novel imaging modalities in the gastrointestinal tract. Her research interests focus on utilization of optical imaging modalities for detection, characterization, monitoring, and treatment of gastrointestinal diseases in preclinical and clinical studies.

ACKNOWLEDGMENTS

Use of the Center for Nanoscale Materials was supported by the U.S. Department of Energy, Office of Science, Office of Basic Energy Sciences, under contract no. DE-AC02-06CH11357. The authors thank Rosemary Wilton from the Biosciences Division at Argonne National Laboratory for useful discussions.

REFERENCES

- (1) Feynman, R. *Eng. Sci.* **1960**, *4*, 23.
- (2) Albert R. Hibbs, rocket scientist at Jet Propulsion Laboratory, the voice of Voyager and other unmanned spacecraft who helped work his way through graduate school at the roulette wheel and dreamed of going to the moon. *Los Angeles Times*, 2003.
- (3) Bard, A. J. *Integrated Chemical Systems. A Chemical Approach to Nanotechnology*; John Wiley & Sons: New York, 1994.
- (4) Rajh, T. *Nat. Mater.* **2006**, *5*, 347.
- (5) Hashimoto, K.; Irie, H.; Fujishima, A. *Jpn. J. Appl. Phys., Part 1* **2005**, *44*, 8269.
- (6) Martin, J. Y.; Schwartz, Z.; Hummert, T. W.; Schraub, D. M.; Simpson, J.; Lankford, J.; Dean, D. D.; Cochran, D. L.; Boyan, B. D. *J. Biomed. Mater. Res.* **1995**, *29*, 389.
- (7) Ellingsen, J. E. *Biomaterials* **1991**, *12*, 593.
- (8) Cai, R.; Hashimoto, K.; Itoh, K.; Kubota, Y.; Fujishima, A. *Bull. Chem. Soc. Jpn.* **1991**, *64*, 1268.
- (9) Yang, H. G.; Sun, C. H.; Qiao, S. Z.; Zou, J.; Liu, G.; Smith, S. C.; Cheng, H. M.; Lu, G. Q. *Nature* **2008**, *453*, 638.
- (10) Barnard, A. S.; Curtiss, L. A. *Nano Lett.* **2005**, *5*, 1261.
- (11) Satoh, N.; Nakashima, T.; Yamamoto, K. *Sci. Rep.* **2013**, *3*, 1959.
- (12) Wu, Z. Y.; Ouvrard, G.; Gressier, P.; Natoli, C. R. *Phys. Rev. B: Condens. Matter* **1997**, *55*, 10382.
- (13) Wang, H.; Lewis, J. P. *J. Phys.: Condens. Matter* **2006**, *18*, 421.
- (14) Boudreaux, D. S.; Williams, F.; Nozik, A. J. *J. Appl. Phys.* **1980**, *51*, 2158.
- (15) Pascual, J.; Camassel, J.; Mathieu, H. *Phys. Rev. B* **1978**, *18*, 5606.
- (16) Kormann, C.; Bahnemann, D. W.; Hoffmann, M. R. *J. Phys. Chem.* **1988**, *92*, 5196.
- (17) Agekyan, V. T.; Berezhnaya, A. A.; Lutsenko, V. V.; Stepanov, Y. A. *Fiz. Tverd. Tela* **1980**, *22*, 12.
- (18) Kasinski, J. J.; Gomezjahn, L. A.; Faran, K. J.; Gracewski, S. M.; Miller, R. J. D. *J. Chem. Phys.* **1989**, *90*, 1253.
- (19) Tang, H.; Prasad, K.; Sanjines, R.; Schmid, P. E.; Levy, F. *J. Appl. Phys.* **1994**, *75*, 2042.
- (20) Serpone, N.; Lawless, D.; Khairutdinov, R. *J. Phys. Chem.* **1995**, *99*, 16646.
- (21) Hurum, D. C.; Agrios, A. G.; Gray, K. A.; Rajh, T.; Thurnauer, M. C. *J. Phys. Chem. B* **2003**, *107*, 4545.
- (22) Chen, L. X.; Liu, T.; Thurnauer, M. C.; Csencsits, R.; Rajh, T. *J. Phys. Chem. B* **2002**, *106*, 8539.
- (23) Chen, L. X.; Rajh, T.; Jager, W.; Nedeljkovic, J.; Thurnauer, M. C. *J. Synchrotron Radiat.* **1999**, *6*, 445.
- (24) Rajh, T.; Nedeljkovic, J. M.; Chen, L. X.; Poluektov, O.; Thurnauer, M. C. *J. Phys. Chem. B* **1999**, *103*, 3515.
- (25) Chen, L. X.; Rajh, T.; Wang, Z. Y.; Thurnauer, M. C. *J. Phys. Chem. B* **1997**, *101*, 10688.
- (26) de la Garza, L.; Saponjic, Z. V.; Dimitrijevic, N. M.; Thurnauer, M. C.; Rajh, T. *J. Phys. Chem. B* **2006**, *110*, 680.
- (27) Dimitrijevic, N. M.; De la Garza, L.; Rajh, T. *Int. J. Mod. Phys. B* **2009**, *23*, 473.
- (28) Rabatic, B. M.; Dimitrijevic, N. M.; Cook, R. E.; Saponjic, Z. V.; Rajh, T. *Adv. Mater.* **2006**, *18*, 1033.
- (29) Setvin, M.; Aschauer, U.; Scheiber, P.; Li, Y.-F.; Hou, W.; Schmid, M.; Selloni, A.; Diebold, U. *Science* **2013**, *341*, 988.
- (30) Fujishima, A.; Honda, K. *Nature* **1972**, *238*, 37.
- (31) Nozik, A. J. *Faraday Discuss.* **1980**, *70*, 7.
- (32) Gutierrez, C.; Salvador, P. *J. Electroanal. Chem.* **1982**, *138*, 457.
- (33) Schweitzer, C.; Schmidt, R. *Chem. Rev.* **2003**, *103*, 1685.
- (34) Redmond, R. W.; Kochevar, I. E. *Photochem. Photobiol.* **2006**, *82*, 1178.
- (35) Tachikawa, T.; Majima, T. *Langmuir* **2009**, *25*, 7791.
- (36) Thurnauer, M. C.; Katz, J. J.; Norris, J. R. *Proc. Natl. Acad. Sci. U.S.A.* **1975**, *72*, 3270.
- (37) Yanez, J.; Sevilla, C. L.; Becker, D.; Sevilla, M. D. *J. Phys. Chem.* **1987**, *91*, 487.
- (38) Kochi, J. K. In *Free Radicals*; Kochi, J. K., Ed.; John Wiley & Sons: New York, 1973; Vol. II, p 677.
- (39) Murphy, D. M. In *Metal Oxide Catalysis*; Jackson, S. D., Hargreaves, J. S. J., Eds.; Wiley-VCH: Weinheim, 2009; p 1.
- (40) Howe, R. F.; Gratzel, M. *J. Phys. Chem.* **1985**, *89*, 4495.
- (41) Howe, R. F.; Gratzel, M. *J. Phys. Chem.* **1987**, *91*, 3906.
- (42) Thurnauer, M. C.; Dimitrijevic, N. M.; Poluektov, O.; Rajh, T. *Spectrum* **2004**, *17*, 10.
- (43) Dyrek, K.; Che, M. *Chem. Rev.* **1997**, *97*, 305.
- (44) Chiesa, M.; Giannello, E.; Che, M. *Chem. Rev.* **2010**, *110*, 1320.
- (45) Hurum, D. C.; Agrios, A. G.; Crist, S. E.; Gray, K. A.; Rajh, T.; Thurnauer, M. C. *J. Electron Spectrosc. Relat. Phenom.* **2006**, *150*, 155.

- (46) Moore, G. F.; Hambourger, M.; Gervaldo, M.; Poluektov, O. G.; Rajh, T.; Gust, D.; Moore, T. A.; Moore, A. L. *J. Am. Chem. Soc.* **2008**, *130*, 10466.
- (47) Dimitrijevic, N. M.; Vijayan, B. K.; Poluektov, O. G.; Rajh, T.; Gray, K. A.; He, H.; Zapol, P. *J. Am. Chem. Soc.* **2011**, *133*, 3964.
- (48) Li, G.; Dimitrijevic, N. M.; Chen, L.; Nichols, J. M.; Rajh, T.; Gray, K. A. *J. Am. Chem. Soc.* **2008**, *130*, 5402.
- (49) Rajh, T.; Ostafin, A. E.; Micic, O. I.; Tiede, D. M.; Thurnauer, M. C. *J. Phys. Chem.* **1996**, *100*, 4538.
- (50) Dimitrijevic, N. M.; Saponjic, Z. V.; Rabatic, B. M.; Poluektov, O. G.; Rajh, T. *J. Phys. Chem. C* **2007**, *111*, 14597.
- (51) Saponjic, Z. V.; Dimitrijevic, N. M.; Tiede, D. M.; Goshe, A. J.; Zuo, X. B.; Chen, L. X.; Barnard, A. S.; Zapol, P.; Curtiss, L.; Rajh, T. *Adv. Mater.* **2005**, *17*, 965.
- (52) Zhu, H. Y.; Lan, Y.; Gao, X. P.; Ringer, S. P.; Zheng, Z. F.; Song, D. Y.; Zhao, J. C. *J. Am. Chem. Soc.* **2005**, *127*, 6730.
- (53) Menzel, R.; Peiro, A. M.; Durrant, J. R.; Shaffer, M. S. P. *Chem. Mater.* **2006**, *18*, 6059.
- (54) Bavykin, D. V.; Friedrich, J. M.; Walsh, F. C. *Adv. Mater.* **2006**, *18*, 2807.
- (55) Gordon, T. R.; Cargnello, M.; Paik, T.; Mangolini, F.; Weber, R. T.; Fornasiero, P.; Murray, C. B. *J. Am. Chem. Soc.* **2012**, *134*, 6751.
- (56) Meriaudeau, P.; Che, M.; Jorgensen, C. K. *Chem. Phys. Lett.* **1970**, *5*, 131.
- (57) Micic, O. I.; Zhang, Y. N.; Cromack, K. R.; Trifunac, A. D.; Thurnauer, M. C. *J. Phys. Chem.* **1993**, *97*, 13284.
- (58) Micic, O. I.; Zhang, Y. N.; Cromack, K. R.; Trifunac, A. D.; Thurnauer, M. C. *J. Phys. Chem.* **1993**, *97*, 7277.
- (59) Standley, K. J.; Vaughan, R. A. *Electron Spin Relaxation Phenomena in Solids*; Adam Hilger Ltd.: London, 1960.
- (60) Stoneham, A. M. *Solid State Commun.* **1965**, *3*, 71.
- (61) Gallay, R.; Vanderklink, J. J.; Moser, J. *Phys. Rev. B: Condens. Matter* **1986**, *34*, 3060.
- (62) Dimitrijevic, N. M.; Poluektov, O. G.; Saponjic, Z. V.; Rajh, T. *J. Phys. Chem. B* **2006**, *110*, 25392.
- (63) Setyawati, M. I.; Tay, C. Y.; Chia, S. L.; Goh, S. L.; Fang, W.; Neo, M. J.; Chong, H. C.; Tan, S. M.; Loo, S. C. J.; Ng, K. W.; Xie, J. P.; Ong, C. N.; Tan, N. S.; Leong, D. T. *Nat. Commun.* **2013**, *4*, 1673.
- (64) Hashizume, H.; Baluk, P.; Morikawa, S.; McLean, J. W.; Thurston, G.; Robarge, S.; Jain, R. K.; McDonald, D. M. *Am. J. Pathol.* **2000**, *156*, 1363.
- (65) Huang, R.-L.; Teo, Z.; Chong, H. C.; Zhu, P.; Tan, M. J.; Tan, C. K.; Lam, C. R. I.; Sng, M. K.; Leong, D. T. W.; Tan, S. M.; Kersten, S.; Ding, J. L.; Li, H. Y.; Tan, N. S. *Blood* **2011**, *118*, 3990.
- (66) Gurr, J. R.; Wang, A. S. S.; Chen, C. H.; Jan, K. Y. *Toxicology* **2005**, *213*, 66.
- (67) Trouiller, B.; Reliene, R.; Westbrook, A.; Solaimani, P.; Schiestl, R. H. *Cancer Res.* **2009**, *69*, 8784.
- (68) Yin, J.-J.; Liu, J.; Ehrenshaft, M.; Roberts, J. E.; Fu, P. P.; Mason, R. P.; Zhao, B. *Toxicol. Appl. Pharmacol.* **2012**, *263*, 81.
- (69) Rajh, T.; Chen, L. X.; Lukas, K.; Liu, T.; Thurnauer, M. C.; Tiede, D. M. *J. Phys. Chem. B* **2002**, *106*, 10543.
- (70) Hoffmann, M. R.; Martin, S. T.; Choi, W. Y.; Bahnemann, D. W. *Chem. Rev.* **1995**, *95*, 69.
- (71) Mills, A.; LeHunte, S. *J. Photochem. Photobiol. A* **1997**, *108*, 1.
- (72) Schwarz, P. F.; Turro, N. J.; Bossmann, S. H.; Braun, A. M.; Wahab, A.; Durr, H. *J. Phys. Chem. B* **1997**, *101*, 7127.
- (73) Nosaka, Y.; Natsui, H.; Sasagawa, M.; Nosaka, A. Y. *J. Phys. Chem. B* **2006**, *110*, 12993.
- (74) Daimon, T.; Nosaka, Y. *J. Phys. Chem. C* **2007**, *111*, 4420.
- (75) Tachikawa, T.; Majima, T. *J. Fluoresc.* **2007**, *17*, 727.
- (76) Christ, T.; Kulzer, F.; Bordat, P.; Basche, T. *Angew. Chem., Int. Ed.* **2001**, *40*, 4192.
- (77) Kahn, A. U. *Int. J. Quantum Chem.* **1991**, *39*, 251.
- (78) Janczyk, A.; Krakowska, E.; Stochel, G.; Macyk, W. *J. Am. Chem. Soc.* **2006**, *128*, 15574.
- (79) Nakamura, R.; Nakato, Y. *J. Am. Chem. Soc.* **2004**, *126*, 1290.
- (80) Panus, P. C.; Radi, R.; Chumley, P. H.; Lillard, R. H.; Freeman, B. A. *Free Radical Biol. Med.* **1993**, *14*, 217.
- (81) Sawunyama, P.; Fujishima, A.; Hashimoto, K. *Langmuir* **1999**, *15*, 3551.
- (82) Doane, T. L.; Burda, C. *Chem. Soc. Rev.* **2012**, *41*, 2885.
- (83) Dunford, R.; Salinaro, A.; Cai, L. Z.; Serpone, N.; Horikoshi, S.; Hidaka, H.; Knowland, J. *FEBS Lett.* **1997**, *418*, 87.
- (84) Wamer, W. G.; Yin, J. J.; Wei, R. R. *Free Radical Biol. Med.* **1997**, *23*, 851.
- (85) Hirakawa, K.; Hirano, T. *Chem. Lett.* **2006**, *35*, 832.
- (86) Nenadovic, M. T.; Rajh, T.; Micic, O. I.; Nozik, A. J. *J. Phys. Chem.* **1984**, *88*, 5827.
- (87) Scholkmann, F.; Kleiser, S.; Metz, A. J.; Zimmermann, R.; Mata Pavia, J.; Wolf, U.; Wolf, M. *NeuroImage* **2013**, *85*, 6–27.
- (88) Paunesku, T.; Rajh, T.; Wiederrecht, G.; Maser, J.; Vogt, S.; Stojicevic, N.; Protic, M.; Lai, B.; Oryhon, J.; Thurnauer, M.; Woloschak, G. *Nat. Mater.* **2003**, *2*, 343.
- (89) Rajh, T.; Poluektov, O.; Dubinski, A. A.; Wiederrecht, G.; Thurnauer, M. C.; Trifunac, A. D. *Chem. Phys. Lett.* **2001**, *344*, 31.
- (90) Dimitrijevic, N. M.; Rozhkova, E.; Rajh, T. *J. Am. Chem. Soc.* **2009**, *131*, 2893.
- (91) Hirsh, D. J.; Beck, W. F.; Innes, J. B.; Brudvig, G. W. *Biochem.* **1992**, *31*, 532.
- (92) Rajh, T.; Dimitrijevic, N. M.; Elhofy, A.; Rozhkova, E. In *Handbook of Nanophysics*; Sattler, K. D., Ed.; CRC: Boca Raton, FL2010; Vol. Functional Nanomaterials.
- (93) Rajh, T.; Saponjic, Z.; Liu, J. Q.; Dimitrijevic, N. M.; Scherer, N. F.; Vega-Arroyo, M.; Zapol, P.; Curtiss, L. A.; Thurnauer, M. C. *Nano Lett.* **2004**, *4*, 1017.
- (94) Liu, J.; de la Garza, L.; Zhang, L.; Dimitrijevic, N. M.; Zuo, X.; Tiede, D. M.; Rajh, T. *Chem. Phys.* **2007**, *339*, 154.
- (95) Liu, J.; Saponjic, Z.; Dimitrijevic, N. M.; Luo, S.; Preuss, D.; Rajh, T. In *Colloidal Quantum Dots for Biomedical Applications*; Osinski, M., Yamamoto, K., Jovin, T. M., Eds.; Proc. SPIE: San Jose, CA, 2006; Vol. 6096.
- (96) Paunesku, T.; Vogt, S.; Lai, B.; Maser, J.; Stojicevic, N.; Thurn, K. T.; Osipo, C.; Liu, H.; Legnini, D.; Wang, Z.; Lee, C.; Woloschak, G. E. *Nano Lett.* **2007**, *7*, 596.
- (97) Statz, A. R.; Barron, A. E.; Messersmith, P. B. *Soft Matter* **2008**, *4*, 131.
- (98) Dalsin, J. L.; Lin, L. J.; Tosatti, S.; Voros, J.; Textor, M.; Messersmith, P. B. *Langmuir* **2005**, *21*, 640.
- (99) Rozhkova, E. A.; Ulasov, I.; Lai, B.; Dimitrijevic, N. M.; Lesniak, M. S.; Rajh, T. *Nano Lett.* **2009**, *9*, 3337.
- (100) Endres, P. J.; Paunesku, T.; Vogt, S.; Meade, T. J.; Woloschak, G. E. *J. Am. Chem. Soc.* **2007**, *129*, 15760.
- (101) Tokuoka, Y.; Yamada, M.; Kawashima, N.; Miyasaka, T. *Chem. Lett.* **2006**, *35*, 496.
- (102) Paramaguru, G.; Solomon, R. V.; Venuvanalingam, P.; Renganathan, R. *J. Fluoresc.* **2011**, *21*, 1887.
- (103) Lopez, T.; Ortiz, E.; Alvarez, M.; Navarrete, J.; Odriozola, J. A.; Martinez-Ortega, F.; Paez-Mozo, E. A.; Escobar, P.; Espinoza, K. A.; Rivero, I. A. *Nanomed. Nanotechnol.* **2010**, *6*, 777.
- (104) Zheng, L.; Lan, M.; Pei-Nan, W.; Ji-Yao, C. *Nanoscale Res. Lett.* **2011**, *6*, 356 (7 pp.).
- (105) Li, Z.; Pan, X.; Wang, T.; Wang, P.-N.; Chen, J.-Y.; Mi, L. *Nanoscale Res. Lett.* **2013**, 8157.
- (106) Huang, K.; Chen, L.; Liao, M.; Xiong, J. *Int. J. Photoenergy* **2012**, *367072*.
- (107) Huang, K.; Chen, L.; Xiong, J.; Liao, M. *Int. J. Photoenergy* **2012**, *631435*.
- (108) George, S.; Pokhrel, S.; Ji, Z. X.; Henderson, B. L.; Xia, T.; Li, L. J.; Zink, J. I.; Nel, A. E.; Madler, L. *J. Am. Chem. Soc.* **2011**, *133*, 11270.
- (109) Dolmans, D.; Kadambi, A.; Hill, J. S.; Waters, C. A.; Robinson, B. C.; Walker, J. P.; Fukumura, D.; Jain, R. K. *Cancer Res.* **2002**, *62*, 2151.
- (110) Hui, H. X.; Dotta, F.; Di Mario, U.; Perfetti, R. *J. Cell. Physiol.* **2004**, *200*, 177.
- (111) Janczyk, A.; Wolnicka-Gtubisz, A.; Urbanska, K.; Kisch, H.; Stochel, G.; Macyk, W. *Free Radical Biol. Med.* **2008**, *44*, 1120.
- (112) Life Technologies, <http://tools.lifetechnologies.com/content/sfs/manuals/mp13244.pdf>, 2009.

- (113) Sawyer, S. A.; Parsch, J.; Zhang, Z.; Hartl, D. L. *Proc. Natl. Acad. Sci. U.S.A.* **2007**, *104*, 6504.
- (114) Encyclopaedia Britannica Online, Encyclopædia Britannica Inc.: <http://www.britannica.com/EBchecked/topic/399695/mutation>, 2014.
- (115) Egholm, M.; Buchardt, O.; Christensen, L.; Behrens, C.; Freier, S. M.; Driver, D. A.; Berg, R. H.; Kim, S. K.; Norden, B.; Nielsen, P. E. *Nature* **1993**, *365*, 566.
- (116) Wittung, P.; Nielsen, P. E.; Buchardt, O.; Egholm, M.; Norden, B. *Nature* **1994**, *368*, 561.
- (117) Brown, E. M. B.; Paunesku, T.; Wu, A.; Thurn, K. T.; Haley, B.; Clark, J.; Priester, T.; Woloschak, G. E. *Anal. Biochem.* **2008**, *383*, 226.
- (118) Todd, J. A.; Bell, J. I.; McDevitt, H. O. *Nature* **1987**, *329*, 599.
- (119) Giacomini, K. M.; Huang, S. M.; Tweedie, D. J.; Benet, L. Z.; Brouwer, K. L. R.; Chu, X. Y.; Dahlin, A.; Evers, R.; Fischer, V.; Hillgren, K. M.; Hoffmaster, K. A.; Ishikawa, T.; Keppeler, D.; Kim, R. B.; Lee, C. A.; Niemi, M.; Polli, J. W.; Sugiyama, Y.; Swaan, P. W.; Ware, J. A.; Wright, S. H.; Yee, S. W.; Zamek-Gliszczynski, M. J.; Zhang, L.; International, T. *Nat. Rev. Drug Discovery* **2010**, *9*, 215.
- (120) Tachikawa, T.; Asanoi, Y.; Kawai, K.; Tojo, S.; Sugimoto, A.; Fujitsuka, M.; Majima, T. *Chem.—Eur. J.* **2008**, *14*, 1492.
- (121) Prinz, J. C. *J. Eur. Acad. Dermatol. Venereol.* **2003**, *17*, 257.
- (122) Gottlieb, S. L.; Gilleadeau, P.; Johnson, R.; Estes, L.; Woodworth, T. G.; Gottlieb, A. B.; Krueger, J. G. *Nat. Med.* **1995**, *1*, 442.
- (123) Schlaak, J. F.; Buslau, M.; Jochum, W.; Hermann, E.; Girndt, M.; Gallati, H.; Zumbuschenfelde, K. H. M.; Fleischer, B. *J. Invest. Dermatol.* **1994**, *102*, 145.
- (124) Dimitrijevic, N. M.; Saponjic, Z. V.; Rabatic, B. M.; Rajh, T. *J. Am. Chem. Soc.* **2005**, *127*, 1344.
- (125) Debinski, W.; Gibo, D. M.; Hulet, S. W.; Connor, J. R.; Gillespie, G. Y. *Clin. Cancer Res.* **1999**, *5*, 985.
- (126) Mintz, A.; Gibo, D. M.; Slagle-Webb, B.; Christensen, N. D.; Debinski, W. *Neoplasia* **2002**, *4*, 388.
- (127) Debinski, W.; Gibo, D. M. *Mol. Med.* **2000**, *6*, 440.
- (128) Kawakami, K.; Kawakami, M.; Snoy, P. J.; Husain, S. R.; Puri, R. K. *J. Exp. Med.* **2001**, *194*, 1743.
- (129) Kawakami, K.; Taguchi, J.; Murata, T.; Puri, R. K. *Blood* **2001**, *97*, 2673.
- (130) Kawakami, K.; Takeshita, F.; Puri, R. K. *J. Biol. Chem.* **2001**, *276*, 25114.
- (131) Wykosky, J.; Gibo, D. M.; Stanton, C.; Debinski, W. *Clin. Cancer Res.* **2008**, *14*, 199.
- (132) Zhou, G.; Yet, G. J.; Debinski, W.; Roizman, B. *Proc. Natl. Acad. Sci. U.S.A.* **2002**, *99*, 15124.
- (133) Bernardi, R. J.; Lowery, A. R.; Thompson, P. A.; Blaney, S. M.; West, J. L. *J. Neuro Oncol.* **2008**, *86*, 165.
- (134) Strathmann, J.; Klimo, K.; Sauer, S. W.; Okun, J. G.; Prehn, J. H. M.; Gerhaeuser, C. *FASEB J.* **2010**, *24*, 2938.
- (135) Zarębski, M.; Kordon, M.; Dobrucki, J. W. *Photochem. Photobiol.* **2014**, n/a.
- (136) Xu, J.; Sun, Y.; Huang, J.; Chen, C.; Liu, G.; Jiang, Y.; Zhao, Y.; Jiang, Z. *Bioelectrochemistry* **2007**, *71*, 217.
- (137) Nagrath, S.; Sequist, L. V.; Maheswaran, S.; Bell, D. W.; Irimia, D.; Ulkus, L.; Smith, M. R.; Kwak, E. L.; Digumarthy, S.; Muzikansky, A.; Ryan, P.; Balis, U. J.; Tompkins, R. G.; Haber, D. A.; Toner, M. *Nature* **2007**, *450*, 1235.
- (138) Elvira, G.; Moreno, B.; del Valle, I.; Garcia-Sanz, J. A.; Canillas, M.; Chinarro, E.; Jurado, J. R.; Silva, A. *J. Biomater. Appl.* **2012**, *26*, 1069.
- (139) Del Valle, I.; Elvira, G.; Garcia-Benzاقون, L.; Armesilla-Diaz, A.; Kremer, L.; Garcia-Sanz, J. A.; Martinez, S.; Silva, A. *Neuroscience* **2010**, *169*, 1473.
- (140) Rozhkova, E. A. *Adv. Mater.* **2011**, *23*, H136.
- (141) Kerr, J. F. R.; Winterford, C. M.; Harmon, B. V. *Cancer* **1994**, *73*, 2013.
- (142) Wang, G.-L.; Xu, J.-J.; Chen, H.-Y. *Biosens. Bioelectron.* **2009**, *24*, 2494.
- (143) Vasilescu, A.; Andreescu, S.; Bala, C.; Litescu, S. C.; Noguer, T.; Marty, J. L. *Biosens. Bioelectron.* **2003**, *18*, 781.
- (144) Kumar, S. A.; Chen, S.-M. *Anal. Chim. Acta* **2007**, *592*, 36.
- (145) Lin, C.-C.; Chu, Y.-M.; Chang, H.-C. *Sens. Actuators, B* **2013**, *187*, 533.
- (146) Yamaguchi, K.; Sugiyama, T.; Kato, S.; Kondo, Y.; Ageyama, N.; Kanekiyo, M.; Iwata, M.; Koyanagi, Y.; Yamamoto, N.; Honda, M. *J. Med. Virol.* **2008**, *80*, 1322.
- (147) Yuan, Y.; Ynan, R.; Chai, Y.; Zhuo, Y.; Shi, Y.; He, X.; Miao, X. *Electroanalysis* **2007**, *19*, 1402.
- (148) Kato, K.; Asai, S.; Taga, H.; Tominaga, Y.; Ishikawa, K.; Arakawa, Y. *Hepatol. Res.* **1997**, *8*, 95.
- (149) Bader, D.; Riskin, A.; Vafsi, O.; Tamir, A.; Peskin, B.; Israel, N.; Merksamer, R.; Dar, H.; David, M. *Clin. Chim. Acta* **2004**, *349*, 15.
- (150) Stefanova, I.; Horejsi, V.; Kristofova, H.; Angelisova, P.; Zizkovsky, V.; Hilgert, I. *J. Immunol. Methods* **1988**, *111*, 67.
- (151) Wang, G.-L.; Xu, J.-J.; Chen, H.-Y.; Fu, S.-Z. *Biosens. Bioelectron.* **2009**, *25*, 791.
- (152) Huang, K.-J.; Wu, Z.-W.; Wu, Y.-Y.; Liu, Y.-M. *Can. J. Chem.* **2012**, *90*, 608.
- (153) Wu, J.; Fu, Z.; Yan, F.; Ju, H. *TrAC, Trends Anal. Chem.* **2007**, *26*, 679.
- (154) Zhang, B.; Zhang, X.; Yan, H.-H.; Xu, S.-J.; Tang, D.-H.; Fu, W.-L. *Biosens. Bioelectron.* **2007**, *23*, 19.
- (155) Park, K. M.; Park, K. D. *J. Mater. Chem.* **2011**, *21*, 15906.
- (156) Wang, R.; Ruan, C.; Kanayeva, D.; Lassiter, K.; Li, Y. *Nano Lett.* **2008**, *8*, 2625.
- (157) Song, Y. Y.; Schmidt-Stein, F.; Bauer, S.; Schmuki, P. *J. Am. Chem. Soc.* **2009**, *131*, 4230.
- (158) Aumelas, A.; Serrero, A.; Durand, A.; Dellacherie, E.; Leonard, M. *Colloids Surf., B* **2007**, *59*, 74.
- (159) Shrestha, N. K.; Macak, J. M.; Schmidt-Stein, F.; Hahn, R.; Mierke, C. T.; Fabry, B.; Schmuki, P. *Angew. Chem., Int. Ed.* **2009**, *48*, 969.
- (160) Li, Q.; Wang, X.; Lu, X.; Tian, H.; Jiang, H.; Lv, G.; Guo, D.; Wu, C.; Chen, B. *Biomaterials* **2009**, *30*, 4708.
- (161) Arora, H. C.; Jensen, M. P.; Yuan, Y.; Wu, A.; Vogt, S.; Paunesku, T.; Woloschak, G. E. *Cancer Res.* **2012**, *72*, 769.
- (162) Qin, Y.; Sun, L.; Li, X.; Cao, Q.; Wang, H.; Tang, X.; Ye, L. *J. Mater. Chem.* **2011**, *21*, 18003.
- (163) Kim, C.; Kim, S.; Oh, W.-K.; Choi, M.; Jang, J. *Chem.—Eur. J.* **2012**, *18*, 4902.
- (164) Thurn, K. T.; Paunesku, T.; Wu, A.; Brown, E. M. B.; Lai, B.; Vogt, S.; Maser, J.; Aslam, M.; Dravid, V.; Bergan, R.; Woloschak, G. E. *Small* **2009**, *5*, 1318.
- (165) Wu, K. C. W.; Yamauchi, Y.; Hong, C.-Y.; Yang, Y.-H.; Liang, Y.-H.; Funatsu, T.; Tsunoda, M. *Chem. Commun.* **2011**, *47*, 5232.
- (166) Ruhle, S.; Greenshtein, M.; Chen, S. G.; Merson, A.; Pizem, H.; Sukenik, C. S.; Cahen, D.; Zaban, A. *J. Phys. Chem. B* **2005**, *109*, 18907.
- (167) Finkelstein-Shapiro, D.; Tarakeshwar, P.; Rajh, T.; Mujica, V. *J. Phys. Chem. B* **2010**, *114*, 14642.
- (168) Lee, N.; Hummer, D. R.; Sverjensky, D. A.; Rajh, T.; Hazen, R. M.; Steele, A.; Cody, G. D. *Langmuir* **2012**, *28*, 17322.
- (169) Tarakeshwar, P.; Finkelstein-Shapiro, D.; Hurst, S. J.; Rajh, T.; Mujica, V. *J. Phys. Chem. C* **2011**, *115*, 8994.
- (170) Tarakeshwar, P.; Finkelstein-Shapiro, D.; Rajh, T.; Mujica, V. *Int. J. Quantum Chem.* **2011**, *111*, 1659.
- (171) Strijkers, G. J.; Mulder, W. J. M.; van Tilborg, G. A. F.; Nicolay, K. *Anti-Cancer Agents Med. Chem.* **2007**, *7*, 291.
- (172) Bulte, J. W. M.; Kraitchman, D. L. *NMR Biomed.* **2004**, *17*, 484.
- (173) Weinmann, H. J.; Brasch, R. C.; Press, W. R.; Wesbey, G. E. *Am. J. Roentgenol.* **1984**, *142*, 619.
- (174) Flacke, S.; Fischer, S.; Scott, M. J.; Fuhrhop, R. J.; Allen, J. S.; McLean, M.; Winter, P.; Sicard, G. A.; Gaffney, P. J.; Wickline, S. A.; Lanza, G. M. *Circulation* **2001**, *104*, 1280.
- (175) Voisin, P.; Ribot, E. J.; Miraux, S.; Bouzier-Sore, A.-K.; Lahitte, J.-F.; Bouchaud, V.; Mornet, S.; Thiaudiere, E.; Franconi, J.-M.; Raison, L.; Labrugere, C.; Delville, M.-H. *Bioconjugate Chem.* **2007**, *18*, 1053.
- (176) Guccione, S.; Li, K. C. P.; Bednarski, M. D. *Methods in Enzymology: Imaging in Biological Research, Part B*; Elsevier Academic Press: London, 2004; Vol. 386, p 219.

- (177) Paunesku, T.; Ke, T.; Dharmakumar, R.; Mascheri, N.; Wu, A.; Lai, B.; Vogt, S.; Maser, J.; Thurn, K.; Szolc-Kowalska, B.; Larson, A.; Bergan, R. C.; Omary, R.; Li, D.; Lu, Z.-R.; Woloschak, G. E. *Nanomed. Nanotechnol.* **2008**, *4*, 201.
- (178) Chandran, P.; Sasidharan, A.; Ashokan, A.; Menon, D.; Nair, S.; Koyakutty, M. *Nanoscale* **2011**, *3*, 4150.
- (179) Takahashi, K.; Yamanaka, S. *Cell* **2006**, *126*, 663.
- (180) Ninomiya, K.; Ogino, C.; Oshima, S.; Sonobe, S.; Kuroda, S.; Shimizu, N. *Ultrason. Sonochem.* **2012**, *19*, 607.
- (181) Yamaguchi, S.; Kobayashi, H.; Narita, T.; Kanehira, K.; Sonezaki, S.; Kudo, N.; Kubota, Y.; Terasaka, S.; Houkin, K. *Ultrason. Sonochem.* **2011**, *18*, 1197.
- (182) Hurst, S. J.; Fry, H. C.; Gosztola, D. J.; Rajh, T. *J. Phys. Chem. C* **2011**, *115*, 620.
- (183) Musumeci, A.; Gosztola, D.; Schiller, T.; Dimitrijevic, N. M.; Mujica, V.; Martin, D.; Rajh, T. *J. Am. Chem. Soc.* **2009**, *131*, 6040.
- (184) Rajh, T.; Koritarov, T.; Blaszik, B.; Massich, M.; Konda, V. Manuscript in preparation.